

THÈSE DE DOCTORAT

Soutenue à AMU — Aix-Marseille Université
le ... décembre 2024 par

Raffael DÜLL

SIMULATING EDGE PLASMA TURBULENCE FOR ITER:
Improving the numerical resolution of a very anisotropic, poorly
conditioned diffusion problem

Discipline

Sciences pour l'Ingénieur

Spécialité

Fusion magnétique

École doctorale

ED 353 SCIENCES POUR L'INGÉNIER:
MECANIQUE, PHYSIQUE, MICRO ET NA-
NOELECTRONIQUE

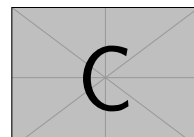
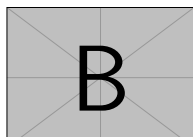
Laboratoire/Partenaires de recherche

Laboratoire de Mécanique, Modélisation &
Procédés Propres (M2P2), AMU
Institut de Recherche sur la Fusion par
Confinement Magnétique (IRFM), CEA
Cadarache

Consignes de présentation détaillées
des pages liminaires en annexe B

Composition du jury

Prénom NOM	Rapporteur·e
Titre et affiliation	
Prénom NOM	Rapporteur·e
Titre et affiliation	
Prénom NOM	Examinateur·rice
Titre et affiliation	
Prénom NOM	Président·e du jury
Titre et affiliation	
Prénom NOM	Directeur·rice de thèse
Titre et affiliation	
Prénom NOM	Membre invité·e
Titre et affiliation	



Affidavit

Je soussigné-e, [Prénom Nom], déclare par la présente que le travail présenté dans ce manuscrit est mon propre travail, réalisé sous la direction scientifique de [Prénom Nom], dans le respect des principes d'honnêteté, d'intégrité et de responsabilité inhérents à la mission de recherche. Les travaux de recherche et la rédaction de ce manuscrit ont été réalisés dans le respect à la fois de la charte nationale de déontologie des métiers de la recherche et de la charte AMU relative à la lutte contre le plagiat.

Ce travail n'a pas été précédemment soumis en France ou à l'étranger dans une version identique ou similaire à un organisme examinateur.

Fait à [ville] le [date]



Cette œuvre est mise à disposition selon les termes de la [Licence Creative Commons Attribution - Pas d'Utilisation Commerciale - Pas de Modification 4.0 International](#).

Liste de publications et participation aux conférences

Liste des publications et/ou brevets réalisées dans le cadre du projet de thèse:

- 1.
- 2.
- 3.

Participation aux conférences et écoles d'été au cours de la période de thèse:

1. PlasmaSurf Summer School, Lisbon Portugal
2. EPS, July 2023, Bordeaux France
3. PET-19, September 2023, Hefei China
4. PSI-26, May 2024, Marseille France
5. ECCOMAS, June 2024, Lisbon Portugal

Résumé et mots clés

Lorem ipsum dolor sit amet, consectetuer adipiscing elit. Ut purus elit, vestibulum ut, placerat ac, adipiscing vitae, felis. Curabitur dictum gravida mauris. Nam arcu libero, nonummy eget, consectetuer id, vulputate a, magna. Donec vehicula augue eu neque. Pellentesque habitant morbi tristique senectus et netus et malesuada fames ac turpis egestas. Mauris ut leo. Cras viverra metus rhoncus sem. Nulla et lectus vestibulum urna fringilla ultrices. Phasellus eu tellus sit amet tortor gravida placerat. Integer sapien est, iaculis in, pretium quis, viverra ac, nunc. Praesent eget sem vel leo ultrices bibendum. Aenean faucibus. Morbi dolor nulla, malesuada eu, pulvinar at, mollis ac, nulla. Curabitur auctor semper nulla. Donec varius orci eget risus. Duis nibh mi, congue eu, accumsan eleifend, sagittis quis, diam. Duis eget orci sit amet orci dignissim rutrum.

Mots clés: géométrie algorithmique, complexe planaire et rectangulaire, géodésique, courbure globale non-positive

Abstract and keywords

Lorem ipsum dolor sit amet, consectetuer adipiscing elit. Ut purus elit, vestibulum ut, placerat ac, adipiscing vitae, felis. Curabitur dictum gravida mauris. Nam arcu libero, nonummy eget, consectetuer id, vulputate a, magna. Donec vehicula augue eu neque. Pellentesque habitant morbi tristique senectus et netus et malesuada fames ac turpis egestas. Mauris ut leo. Cras viverra metus rhoncus sem. Nulla et lectus vestibulum urna fringilla ultrices. Phasellus eu tellus sit amet tortor gravida placerat. Integer sapien est, iaculis in, pretium quis, viverra ac, nunc. Praesent eget sem vel leo ultrices bibendum. Aenean faucibus. Morbi dolor nulla, malesuada eu, pulvinar at, mollis ac, nulla. Curabitur auctor semper nulla. Donec varius orci eget risus. Duis nibh mi, congue eu, accumsan eleifend, sagittis quis, diam. Duis eget orci sit amet orci dignissim rutrum.

Keywords: computational geometry, planar and rectangular complex, geodesic, global nonpositive curvature

Remerciements

Le modèle de thèse AMU n'existerait pas sans la contribution des doctorants. Nous souhaitons remercier tout particulièrement [Mickaël Bojados](#), [Flora Cordoleani](#) et [Florian Caullery](#) pour leur aide précieuse et la qualité de leurs fichiers sources LaTeX. La mise à jour effectuée en 2018 doit beaucoup à l'excellent travail de [Dorian Depriester](#).

Lorem ipsum dolor sit amet, consectetur adipiscing elit. Ut purus elit, vestibulum ut, placerat ac, adipiscing vitae, felis. Curabitur dictum gravida mauris. Nam arcu libero, nonummy eget, consectetur id, vulputate a, magna. Donec vehicula augue eu neque. Pellentesque habitant morbi tristique senectus et netus et malesuada fames ac turpis egestas. Mauris ut leo. Cras viverra metus rhoncus sem. Nulla et lectus vestibulum urna fringilla ultrices. Phasellus eu tellus sit amet tortor gravida placerat. Integer sapien est, iaculis in, pretium quis, viverra ac, nunc. Praesent eget sem vel leo ultrices bibendum. Aenean faucibus. Morbi dolor nulla, malesuada eu, pulvinar at, mollis ac, nulla. Curabitur auctor semper nulla. Donec varius orci eget risus. Duis nibh mi, congue eu, accumsan eleifend, sagittis quis, diam. Duis eget orci sit amet orci dignissim rutrum.

Nam dui ligula, fringilla a, euismod sodales, sollicitudin vel, wisi. Morbi auctor lorem non justo. Nam lacus libero, pretium at, lobortis vitae, ultricies et, tellus. Donec aliquet, tortor sed accumsan bibendum, erat ligula aliquet magna, vitae ornare odio metus a mi. Morbi ac orci et nisl hendrerit mollis. Suspendisse ut massa. Cras nec ante. Pellentesque a nulla. Cum sociis natoque penatibus et magnis dis parturient montes, nascetur ridiculus mus. Aliquam tincidunt urna. Nulla ullamcorper vestibulum turpis. Pellentesque cursus luctus mauris.

Contents

Affidavit	2
Liste de publications et participation aux conférences	3
Résumé et mots clés	4
Abstract and keywords	5
Remerciements	6
Contents	7
List of Figures	11
List of Tables	15
1. Introduction	16
I. Fundamental Concepts of Fluid Models for Magnetized Plasmas	19
2. Tokamak Concept	20
2.1. Particles in a magnetized plasma	20
2.1.1. Magnetic confinement	20
2.1.2. Tokamak configuration	21
2.1.3. Grad-Shafranov equilibrium	22
2.1.4. Realisation of magnetic configurations	24
2.2. Interaction between particles	27
2.2.1. Debye shielding	27
2.2.2. Particle collisions	27
2.2.3. Macroscopic effects of plasma collisions	30
2.3. Scrape-Off-Layer	31
2.3.1. Fundamental sheath physics	31
2.3.2. Confinement characteristics	31
2.3.3. Problematic of heat exhaust	32

3. Description of Plasmas	33
3.1. Direct description of Plasma Particles	33
3.1.1. Particle Tracking	33
3.1.2. Kinetic Models	34
3.2. Three Fluid Moments of the Kinetic Equation	34
3.2.1. Mass Balance ($k = 0$)	35
3.2.2. Momentum Balance ($k = 1$)	36
3.2.3. Energy Balance ($k = 2$)	36
3.3. MHD description of plasmas	37
3.3.1. Extended MHD Model	37
3.3.2. Reduced MHD model	38
3.3.3. Reduced Ohm's law	39
3.4. Fluid closures	39
4. Drift-reduced models for plasma turbulence	40
4.1. Drift wave turbulence	41
4.1.1. Plasma drifts	41
4.1.2. Drift-ordering approximation	42
4.1.3. Linear plasma instabilities	45
4.2. Electromagnetic effects in edge plasma	48
4.2.1. Magnetic induction	49
4.2.2. Electron inertia	50
4.2.3. Electromagnetic flutter	50
4.3. Comparison to reduced MHD models	51
4.4. Drift-Alfvén waves	51
4.4.1. Dispersion relation	51
4.4.2. Perturbative solution	53
4.4.3. Electromagnetic mode excitation	54
II. An Electromagnetic Model for SOLEDGE3X	57
5. Electromagnetic effects in the SOLEDGE3X framework	58
5.1. Dimensionless fields	58
5.2. Transport equations	60
5.2.1. Mass balance	61
5.2.2. Momentum balance	61
5.2.3. Energy balance	62
5.2.4. Charge balance	62
5.3. Electromagnetic Model in SOLEDGE3X	64
5.3.1. Electron Inertia	65
5.3.2. Electromagnetic Induction	66
5.3.3. Electromagnetic Flutter	67
5.3.4. Formulation of the electromagnetic vorticity system	69

5.4. Boundary conditions	70
6. Numerical Implementation	71
6.1. Geometrical consideration	71
6.1.1. Coordinate system	71
6.1.2. Domain decomposition and mesh design	71
6.1.3. Curvilinear coordinates	72
6.2. The staggered mesh	74
6.2.1. Description and notation of the staggered grid	74
6.2.2. Boundary cells	75
6.2.3. Staggered discrete operators	77
6.2.4. Discretization around the X-point	80
6.3. Implicit-explicit solving procedure	81
6.3.1. Time discretization schemes	81
6.3.2. Initialization at Restart	82
6.4. Electromagnetic vorticity system	83
6.4.1. Matrix formulation of the electromagnetic system	84
6.4.2. Treatment of flutter	85
6.4.3. Evaluation of the condition number	86
7. Verification and Validation	91
7.1. Verification by the Method of manufactured solutions	91
7.1.1. Test system	91
7.1.2. Analytic solution	93
7.1.3. Order of convergence	93
7.2. Linear Analysis	94
7.2.1. Pure advection	94
7.2.2. Electrostatic case	96
7.2.3. Electromagnetic case	97
7.2.4. Linear transition from Alfvén to thermal electron waves	101
III. Impact of Electromagnetic Effects on Plasma Simulations	104
8. Electromagnetic simulations on analytic geometries	105
8.1. Slab configurations	105
8.1.1. Analysis of a plasma blob	105
8.1.2. Generation of drift waves	106
8.2. Circular geometry	108
8.2.1. Simulation set-up	108
8.2.2. Growth rates	109
8.2.3. Stabilization by flutter	110

9. Electromagnetic simulations on a realistic diverted geometry	111
9.1. Electrostatic versus electromagnetic scenarios	111
9.1.1. Simulation set-up	111
9.1.2. Comparison between the scenarios	113
9.1.3. Numerical performances	114
9.1.4. Comparison to the TCV-X21 reference simulations	116
9.2. Electromagnetic power scan	116
9.2.1. Qualitative evolution of the simulation	116
9.2.2. Mid-plane profiles	116
9.2.3. Flutter in the high-power cases	117
10. Simulations of Magnetic ripple	118
10.1. Motivation for simulating magnetic ripple	118
10.2. Generation of a non-axisymmetric magnetic configuration	119
10.3. Application to a WEST scenario	123
10.4. Conclusion	124
Conclusion	126
Bibliography	127
Index	135
APPENDICES	136
A. New software modules	137
A.1. Grad-Shafranov solver	137
A.2. Poincaré plots	137
A.3. Generation of a modulated magnetic configuration	137
A.4. Toroidal plots in pySOLEDGE3X	137
B. Curvilinear metric operators	138
B.1. Linear algebra	138
B.2. Centered operators	139
B.2.1. Differentiation	139
B.2.2. Scheme for centered 2D parallel diffusion	140
B.2.3. Scheme for 3D parallel diffusion	140
B.3. Staggered operators	140
B.3.1. Parallel gradient	140
B.3.2. Perpendicular Laplacian	141

List of Figures

1.1.	Fusion reaction cross-sections for the most promising pairs of light elements over plasma temperature.	17
2.1.	Trajectory of a positively and a negatively charged particle along a homogeneous magnetic field line.	21
2.2.	Simplified scheme of the magnetic field components on a flux surface (a) and the total magnetic field (b).	22
2.3.	Solution of the Grad-Shafranov equation on a circular cross-section with minor radius $a = 0.3$ m. A Cartesian mesh with $N = 200$ equidistant discretization points is used for the R and Z coordinates. The flux Ψ is forced to 0 at the boundary. The toroidal magnetic field is given by $B_\varphi = B_0 R_0 / R$ with $B_0 = 1$ T. The pressure follows an exponential distribution $p(\Psi) = p_0(e^{-\Psi} - 1)$ with $p_0 = 1$ MPa.	24
2.4.	Cutaway of the ITER tokamak (source: ITER Organization)	25
2.5.	Comparison of the limited and diverted configuration on a WEST geometry.	26
2.6.	Trajectory of the projectile particle (red) colliding with the target particle (green). The vector \mathbf{b} denotes the impact factor and χ is the deflection angle caused by the collision.	28
2.7.	Volume for given db and dx in which collisions on the projectile are considered.	29
4.1.	Dependency on the perpendicular wavenumber k_\perp of the real and imaginary parts of the all solutions ω to the dispersion relation 4.58. Except for k_\perp , all other values derive from: $B = 1$ T, $n = 2 \cdot 10^{19} \text{ m}^{-3}$, $T = 100 \text{ eV}$, $\lambda_p = 0.1 \text{ m}$ and $k_\parallel = 0.6 \text{ m}^{-1}$. On a pair of graphs, a given color represents the same mode. In the left plots for $\text{Re}\{\omega\}$, characteristic frequencies of the system are shown for reference ("—" diamagnetic ω_* , "..." electron sound $\omega_{s,e}$, "---" Alfvén ω_A).	55
4.2.	Relative difference of drift-wave frequency in the electromagnetic scenarios to the reference electrostatic case.	56
6.1.	Example of typical mesh and domain decomposition mapping the real domain (a) to a Cartesian multiple zones domain (b). Each colored zone is isomorphic to a cube, the lines connecting the edges indicate the neighbours mapping.	72

6.2.	General view of the staggered grid points marked as crosses on top of the collocated cells. The red cross at the position $[i_\psi, i_\theta - \frac{1}{2}, i_\varphi - \frac{1}{2}]$ corresponds to the central cell with index $[i_\psi, i_\theta, i_\varphi]$	75
6.3.	General view of the staggered grid points in the $\theta - \varphi$ plane. The field A_{\parallel} is defined at the green crosses and j_{\parallel} at the red circles. Crossed cells are boundary cells where the mask is $\chi = 1$	76
6.4.	Neighbors involved to calculated staggered parallel gradients	77
6.5.	Neighbors involved to calculated the parallel divergence. The arrows indicate the in- and outgoing fluxes that need to be calculated, and the dashed lines connect the arrows to the staggered points they require.	79
6.6.	Depiction of the relevant cell faces to calculate fluxes of a staggered field at coordinate index $[i_\psi, i_\theta - \frac{1}{2}, i_\varphi - \frac{1}{2}]$	80
6.7.	Sketches of the mesh around the X-point. For collocated cells (a), 8 cells touch the X-point at a corner. For staggered cells (b), the X-point is located at the radial face of 4 cells, effectively modifying the shape of the cells to pentagons. Fluxes across the involved faces are hence ill-defined.	81
6.8.	Sketches showing the calculation of gradients for the parallel diffusion scheme. It shows the position where the different gradients are calculated that are relevant for a flux across the cell face with a solid line. Green and red arrows symbolize gradients in the equilibrium and in the radial direction, respectively.	83
6.9.	Impact of different parameters on the condition number. Plasma parameters are taken as constant: $B = 1$, $m_i = 2$, $n_e = n_i = 2$, $m_e = 5.5 \cdot 10^{-4}$, $\beta_0 = 10^{-3}$, $\eta_{\parallel} = 10^{-6}$, $\delta_t = 1$ and $N_{\perp} = 100$. The parameters β_0 and n_e are deliberately chosen large to ensure the validity of the positive-definiteness condition 6.26. Black curves correspond to the electrostatic system, and red curves to the electromagnetic matrices, with full lines indicating electron inertia and dashed lines representing $m_e = 0$	90
7.1.	Distorted MMS mesh geometry with $N = 20$ cells per dimension on a 3rd of a torus	91
7.2.	Relative error between the initial plasma and the solution after one timestep. The x -axis indicates the number of points per zone in each direction, the total number of points is thus $N_{tot}^{3D} = 8 \cdot X^3$ (resp. $N_{tot}^{2D} = 4 \cdot X^2$). The dashed lines indicate the slope of the ideal 2nd order convergence	94
7.3.	Evolution of the 1D SLAB system with 64 cells in poloidal direction over 10000 timesteps with the RK4 scheme. For a better readability only parts of the graphs are represented	96
7.4.	Evolution of the 2D electrostatic SLAB system with 64 cells in radial and poloidal direction over 10000 timesteps with the implicit Euler scheme. The system is grounded at the center of the domain to $\Phi^G = 0V$	97
7.5.	Snapshot of an electromagnetic SLAB simulation on a domain with $N_\psi = 32$ and $N_\theta = 64$ grid points. All point at the radial center with i_ψ^G are grounded.	100

7.6. Relative error for the fits of the frequency ω_0 and the decay rate λ on the evolution of A_{\parallel} with respect to the expected values in a grounded electromagnetic SLAB simulation on a domain with $N_{\psi} = 32$ and $N_{\theta} = 64$ grid points.	101
7.7. Fitted wave frequencies as a function of the perpendicular wave numbers. The lines indicate the theoretical wave frequencies in the electrostatic case with finite electron mass (ES), the electromagnetic case with $m_e = 0$ (EM), and the complete electromagnetic case with electron inertia (ES + EM).	103
8.1. Density profiles [part/m ³] after 9.6 μ s simulated plasma time for the electrostatic (ES), magnetic inductive (EM) and full electromagnetic scenarios (EM-flutter). The first row shows a view of the $R - \varphi$ plane with the maximum density taken along the Z coordinate. The second and third rows show the density on poloidal planes ($R - Z$) at the center of the field lines (1) and in proximity to the sheath (2).	106
8.2. Density profiles [part/m ³] at the toroidal center of the slab, at about 32m from both limiters. The snapshots compare the electrostatic (ES), magnetic inductive (EM) and full electromagnetic scenarios (EM-flutter) scenarios after 8, 16 and 24 μ s simulated plasma time.	108
8.3. Snapshots of the electron temperature T_e fluctuations	109
8.4. Evolution of the perturbation intensity for different values of m_e . The electron mass is artificially increased and the 0 factor corresponds effectively to the electrostatic reference	109
8.5. Evolution of the perturbation intensity for different values of β . The is artificially increased and the 0 factor corresponds effectively to the electrostatic with electron inerita. The electron mass for all scenarios is physical (factor 1 in Fig. 8.4).	110
9.1. Simulation snapshots of the full electromagnetic scenario with flutter. The first poloidal plane is shown after 6 ms simulated plasma time on the TCV case. From left to right, the first row shows the ion density n_i , the electron temperature T_e , the electric potential Φ , and the radial "ExB" drift velocity v_E^{ψ} . The second row shows the parallel magnetic potential A_{\parallel} , the parallel current density j_{\parallel} , the amplitude of the flutter field $\ \tilde{\mathbf{B}}\ $, and the radial flutter advection velocity $v_{\tilde{b}\psi}$	112
9.2. Evolution of the kinetic energy and heat exhaust over time iterations on the turbulent TCV scenario. It indicates the turbulence level and its consequence on the total heat transport.	113
9.3. Radial profiles at the outer mid-plane after 6 ms simulated plasma time. These profiles were obtained by averaging simulation data across all 32 toroidal planes and over the last 20 available plasma saves.	114
9.4. Radial profiles at the outer mid-plane after 4ms.	116
9.5. Poincaré plot of the fluctuating magnetic field in the TCV high-power case.	117

10.1. Infrared camera view of the divertor target, taken from [4]. Red zones correspond to hot regions with high heat deposition. One can see the "snake skin" pattern, where the maximal intensity alternates between the inner and outer strike points.	119
10.2. Exemplary SOLEDGE3X mesh for a WEST single-null geometry	120
10.3. Top views of the perturbated field \mathbf{B}_{pert} on the WEST tokamak at the mid plane. The black dots indicate the position of the toroidal field coils. The amplitude of the perturbated field remains much smaller than the axisymmetric component, whose amplitude ranges around 1T.	121
10.4. Map of the poloidal field B_{pol} [T] at several poloidal planes within a ripple period around the lower X-point and the divertor targets. Streamlines are superposed to the fields to better visualize the position of the X-point and the separatrix at the divertor. The phase shifts 0 and 1/2 with respect to the coil positions are identical to the axisymmetric configuration as B_{pert}^ψ vanishes while the planes at 1/4 and 3/4 correspond to the respective maximum and minimum of B_{pert}^ψ	122
10.5. Poincaré plot at coil-aligned poloidal planes. Seed points are uniformly distributed on the mid-plane along the radial and toroidal directions. Because of the periodicity of the perturbated field, each point corresponds to a field line crossing any of the N_c planes aligned with a coil. The total length of a field line from wall to wall translates in its color, black standing for an infinite closed field line.	123
10.6. Calculated electron wall heat flux in the divertor region from the SOLEDGE3X simulation. View on the target from the top for one ripple period.	124

List of Tables

9.1. Numerical metrics on the four TCV scenarios for one timestep. All quantities are averaged over the last 20000 timesteps of the simulation. The execution time refers to the wall-clock time and must be multiplied by the number of used processors (768) to get the actual used CPU time. .	115
10.1. Technical parameters of the toroidal field coils used to generate the ripple field for the WEST tokamak	121

1. Introduction

The sun is the primary source of energy for Earth, essential for photosynthesis in plants, which forms the basis of most food chains, and for driving the weather and climate systems that shape our environment. Its consistent radiation supports all life forms, regulates global temperatures, and influences fundamental ecological and biological processes that are vital for the Earth's diverse ecosystems. From the very outset of human life, the sun has been a subject of profound admiration, occupying a central role in various religious beliefs and was often synonym of an incomparably vast and potent source of energy. It was not until the beginning of the twentieth century that progress in particle physics allowed to unravel the secret of solar energy: nuclear fusion. It is the physical process where two light atomic nuclei merge to form a heavier nucleus, releasing significant energy as a result of mass-to-energy conversion.

The dream of achieving nuclear fusion in a laboratory to produce energy emerged shortly thereafter. In today's climate crisis, nuclear fusion is even more appealing because it does not emit carbon emissions, does not present the risk of a catastrophic meltdown and its fuel, hydrogen, is readily available. Since replicating the sun's core conditions on Earth, particularly the immense pressure, is not feasible, alternative approaches were searched. A look at the reaction cross-section of various pairs of light atoms shows that deuterium-tritium (D-T) fusion has the highest likelihood at the lowest temperature. These two hydrogen isotopes are hence the most favorable candidates for fusion; deuterium is naturally abundant, but tritium, which is radioactive and has a relatively short half-life, must be artificially produced.

At such elevated temperatures, the binding energy is insufficient to maintain the cohesion of electrons and atomic nuclei, resulting in the formation of a state of matter known as plasma. Fundamentally, plasma is an ionized gas composed of positively charged nuclei and negatively charged electrons, which interact electromagnetically.

Lawson's criterion[46] estimates the necessary plasma conditions to reach the break-even point, when fusion power exceeds heating and conduction losses. For D-T fusion, the triple product of density n , temperature T and confinement time τ_E must exceed:

$$nT\tau_E > 10^{-21} \text{ keV m}^{-3} \text{ s} \quad (1.1)$$

The reaction cross-section determines an optimal temperature of approximately 15-40 keV (150 millions °C) for fusion reactions, leading fusion reactor designs to focus on maximizing either of the two remaining parameters: density or confinement time. Inertial Confinement Fusion (ICF) seeks to compress dense fuel pellets for an ex-

1. Introduction

tremely brief duration using high-powered lasers. Conversely, Magnetic Confinement Fusion (MCF) utilizes strong magnetic fields to sustain stable plasmas at relatively low densities. Both approaches have conducted promising experiments close to the break-even point. Within MCF, there are two primary designs: tokamaks, which use a toroidal chamber with an axisymmetric magnetic field, and stellarators, which use a twisted magnetic configuration to improve plasma confinement.

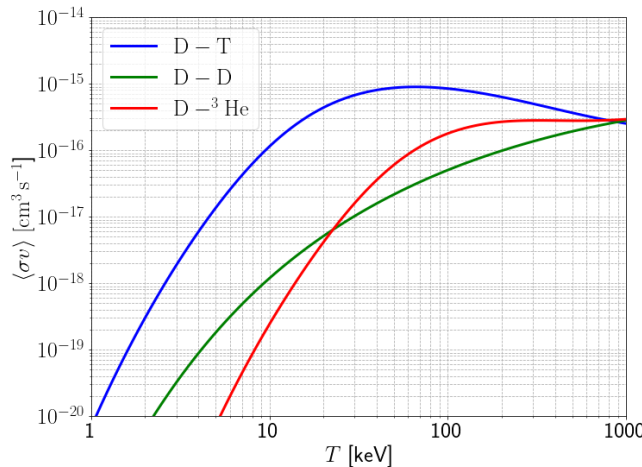


Figure 1.1.: Fusion reaction cross-sections for the most promising pairs of light elements over plasma temperature.

For MCF
 Plasma heating
 - Ohmic heating
 - ICRH, ECRH, NBI

fusion gain Q as essential metric.

show diagram with all machines, scaling laws for fusion performance

The largest fusion experiment ITER, is currently under construction in southern France by an international collaboration of seven member parties. At its full operation it is expected to achieve ignition, a state where the fusion reaction emits sufficiently radiation to maintain the plasma conditions. It requires a heat exhaust ten times higher than the break-even point and is a critical milestone for the development of future commercial fusion reactors.

Introduce necessity for (electromagnetic) turbulent simulations (estimate cross-field transport, power exhaust, ELMs...)

1. Introduction

Currently turbulent SOLEDGE3X limited to L-modes and small machines. Numerical issues and limited model for larger machines. Limitations due to the anisotropy between the parallel (resistive) and perpendicular (from the time evolution of the vorticity) Laplacian on the potential. Problematic if the resistivity gets very small. Even in the electrostatic collisional regime found in the plasma edge, electron inertial and electromagnetic effects play a substantial role. Especially electron inertia replaces resistivity as it approaches zero.

The current implementation of SOLEDGE3X is primarily limited to simulating L-mode plasmas and smaller tokamaks due to various numerical challenges and the limited applicability of its models to larger machines. A significant limitation arises from the anisotropy between the parallel (resistive) and perpendicular (vorticity-driven) Laplacians acting on the electric potential. In the existing electromagnetic model, the vorticity equation is solved implicitly and as the resistivity approaches zero, the condition number of the matrix deteriorates considerably. Even in the electrostatic, collisional regime typically found in edge plasma, electron inertia and electromagnetic effects play a crucial role, and notably the finite electron mass in Ohm's law acts as a lower bound for the resistivity.

As the plasma approaches the LH transition, electromagnetic effects become increasingly important. The H-mode is characterized by a suppression of cross-field transport due to "ExB" drifts, which gets partly replaced by electromagnetic transport. Significant magnetic reconnection processes lead to an important transport of plasma particles from the hot core to the cold edge, with radial fluxes still below "ExB" advection, but non-negligible to understand the physical plasma behavior.

This thesis is dedicated to the implementation of an electromagnetic model within SOLEDGE3X, which includes magnetic induction in the parallel electric field, perturbations of the magnetic equilibrium (flutter), and a finite electron mass in Ohm's law. This development pursues several goals: first, it improves the accuracy of the physical model; second, it enhances the numerical robustness by mitigating the poor matrix conditioning associated with low resistivity; and third, it establishes a foundation for self-consistent turbulent simulations that are relevant to larger machines and higher-power scenarios.

Part I.

Fundamental Concepts of Fluid Models for Magnetized Plasmas

2. Tokamak Concept

Fusion reactions require extreme temperatures at about 15keV to happen. At such high temperatures, any matter transforms into an ionized state, called plasma, where electrons are dissociated from their atomic core. Charged particles are particularly responsive to magnetic fields, a property that will be used by tokamaks to confine the hot plasma and protect the physical walls of the device.

A deuterium plasma is an ionized gas comprising positively charged ions (D^+) and negatively charged electrons (e^-). Initially, both species exhibit independent dynamics. Despite having exactly opposite charges, ions are significantly heavier than electrons, with a mass ratio of $m_i/m_e \approx 3.7 \cdot 10^3$. Both ions and electrons can be described by their respective momenta and temperatures. In Sec. 2.1, we first describe their independent behavior in a magnetized environment, then how species interact in Sec. 2.2 and we finish with Sec. 2.3 about the importance of the Scrape-Off-Layer.

2.1. Particles in a magnetized plasma

This first section is dedicated to elucidate the fundamental working principle of tokamaks. Before all, we must understand how charged particles behave when exposed to strong magnetic fields (in Sec. 2.1.1) and how this knowledge allows us to design a magnetic "cage", in which particles are trapped, or confined (in Sec. 2.1.2). The governing equations of this magnetic configuration are given in Sec. 2.1.3 and Sec. 2.1.4 introduces and compares limited and diverted configurations.

2.1.1. Magnetic confinement

To understand how charged plasma particles can be confined on a magnetic field line, we consider the simplest example of a single particle with charge q in a homogeneous, unidirectional magnetic field \mathbf{B} with directional unit vector \mathbf{b} . The amplitude of the magnetic field is then B such that $\mathbf{B} = B\mathbf{b}$. Solely the magnetic component of Lorentz's force acts on a particle with mass m and charge q , leading to the following equation for its velocity \mathbf{v} :

$$m \frac{d\mathbf{v}}{dt} = q\mathbf{v} \times \mathbf{B} \quad (2.1)$$

To solve this differential equation, it is convenient to decompose the velocity vector into a parallel component $v_{\parallel} = \mathbf{v} \cdot \mathbf{b}$ and a perpendicular component $\mathbf{v}_{\perp} = \mathbf{v} - v_{\parallel}\mathbf{b}$. For a given initial velocity \mathbf{v}_0 , the general solution of this system is:

$$\mathbf{v}(t) = v_{\parallel,0} \mathbf{b} + \mathbf{v}_{\perp,0} \cos(\omega_B t) + \mathbf{b} \times \mathbf{v}_{\perp,0} \sin(\omega_B t) \quad (2.2)$$

with $\omega_B = \frac{qB}{m}$ being the cyclotron frequency. This implies that a charged particle circles around a magnetic field line while following it with its initial velocity. The opposite charges of ions and electrons result in them circling in different directions. The trajectory is qualitatively shown in Fig. 2.1. The radius of this gyromotion is called the Larmor radius ρ_L :

$$\rho_L = \frac{m \|\mathbf{v}_{\perp,0}\|}{qB} \quad (2.3)$$

Because of the high mass ratio, ions have a much larger Larmor radius than electrons. This gyromotion is the fundamental mechanism behind magnetic confinement.

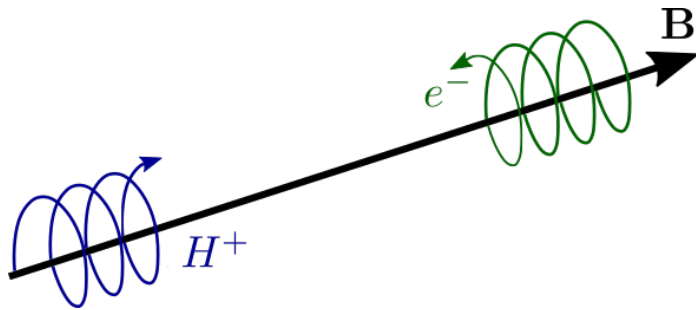


Figure 2.1.: Trajectory of a positively and a negatively charged particle along a homogeneous magnetic field line.

For a non-homogeneous field, Eq. 2.1 does not necessarily have a straightforward solution. To assume gyromotion as the fundamental dynamic for particles, the magnetic field must remain relatively constant along the helical path traced by the field lines. This requirement imposes a criterion on the Larmor radius, known as adiabatic theory:

$$\rho_L \ll \frac{B}{\|\nabla B\|} \quad (2.4)$$

2.1.2. Tokamak configuration

Maxwell's law stipulates that the magnetic field must be divergence-free, $\nabla \cdot \mathbf{B} = 0$. Since constructing an infinitely long machine is impractical, particle confinement requires that a given field line be closed, meaning that following its path would return one to the initial position. This necessitates some bending of the magnetic field lines. The fundamental principle of a tokamak lies in its magnetic configuration, which is designed to confine hot plasma within a toroidal chamber. This configuration comprises two primary magnetic field components: the toroidal field B_ϕ and the poloidal field B_p . Coils encircling the torus generate the toroidal field, which runs

2. Tokamak Concept – 2.1. Particles in a magnetized plasma

parallel to the circular path of the tokamak and serves to confine the plasma. A strong current passing through the plasma itself induces the poloidal field. The combination of these fields creates a twisted, helical magnetic field structure, as shown in Fig. 2.2, that stabilizes the plasma and helps maintain its shape and position within the tokamak.

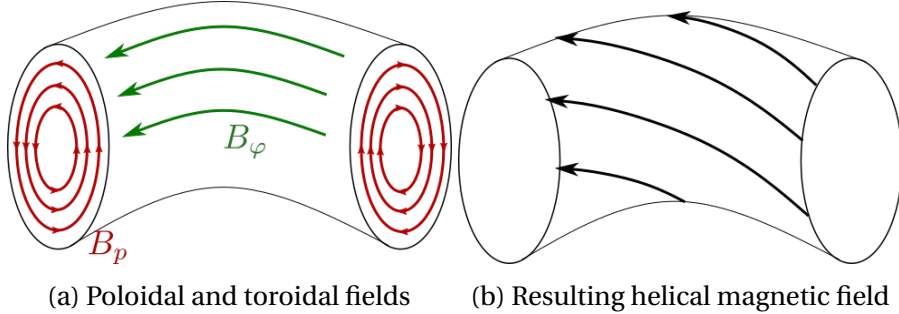


Figure 2.2.: Simplified scheme of the magnetic field components on a flux surface (a) and the total magnetic field (b).

The helical configuration of a magnetic field line in a tokamak ensures that tracing its path remains within the same toroidal surface, ultimately returning to the initial point and forming a closed field line. The ensemble of all such field lines constitutes what is termed a "closed magnetic flux surface." These flux surfaces are radially concentric, and the principle of magnetic confinement is to trap plasma particles within these flux surfaces.

At first glance, the toroidal field appears sufficient to close magnetic field lines. However, internal and external perturbations can cause twisting of the magnetic field lines, potentially leading to disruptions and total loss of plasma confinement. This phenomenon is known as kink instabilities. To suppress them, the poloidal field introduces magnetic shear to the configuration, with field lines circling around the minor radius of the torus. The ratio of toroidal to poloidal rotations of the field lines is known as the safety factor $q = \frac{aB_\varphi}{RB_p}$. In a cylindrical approximation, the Kruskal-Shafranov limit [45, 70] states that kink instabilities are suppressed for $q > 1$. However, the safety factor cannot be too large either, as other instabilities such as tearing [26] or resistive wall [25] modes might appear and deteriorate plasma confinement.

2.1.3. Grad-Shafranov equilibrium

How can the magnetic configuration be described in a more mathematical way? The magnetic configuration of a tokamak can be described mathematically in cylindrical coordinates (R, Z, φ) with the corresponding basis vectors $[\mathbf{e}_R, \mathbf{e}_Z, \mathbf{e}_\varphi]$. The magnetic field consists of two main components: the poloidal field \mathbf{B}_p , which lies in the (R, Z)

2. Tokamak Concept – 2.1. Particles in a magnetized plasma

plane (referred to as the "poloidal plane"), and the toroidal field \mathbf{B}_φ , which is aligned along the φ -direction.

Each magnetic field \mathbf{B} is associated with a vector potential \mathbf{A} such that:

$$\nabla \times \mathbf{A} = \mathbf{B} \quad (2.5)$$

Assuming axisymmetry, gradients along the φ -direction vanish. Let $\mathbf{A} = A_R \mathbf{e}_R + A_Z \mathbf{e}_Z + A_\varphi \mathbf{e}_\varphi$ represent the three components of the vector potential. The magnetic field can then be expressed as:

$$\mathbf{B} = \left(\frac{1}{R} \frac{\partial(RA_\varphi)}{\partial Z} \right) \mathbf{e}_R - \left(\frac{1}{R} \frac{\partial(RA_\varphi)}{\partial R} \right) \mathbf{e}_Z + \left(\frac{\partial A_Z}{\partial R} - \frac{\partial A_R}{\partial Z} \right) \mathbf{e}_\varphi \quad (2.6)$$

Introducing the poloidal flux function $\Psi = -RA_\varphi$, which shapes \mathbf{B}_p , and the toroidal field function $F = RB_\varphi$, the magnetic field components can be written as:

$$\mathbf{B} = \underbrace{\nabla\Psi \times \nabla\varphi}_{\mathbf{B}_p} + \underbrace{F\nabla\varphi}_{\mathbf{B}_\varphi} \quad (2.7)$$

In a tokamak, the plasma is not uniform, leading to a pressure gradient from the colder edge to the hotter core. In a stationary plasma that has reached magnetohydrodynamic (MHD) equilibrium, the magnetic and pressure forces must balance, which is described by the force balance equation:

$$\nabla p = \mathbf{j} \times \mathbf{B} \quad (2.8)$$

Because of the cross-product, ∇p is always perpendicular to \mathbf{B} , implying that p must be constant along a field line. Under the assumption of axisymmetry, $\partial_\varphi p = 0$, meaning that the toroidal component of the magnetic force must be zero. Consequently, only the poloidal field \mathbf{B}_p responds to a pressure gradient. Since the pressure $p(\Psi)$ is both axisymmetric and field-aligned, it can only be a function of the poloidal flux Ψ . The toroidal component of the current density can be expressed as:

$$j_\varphi = R \frac{dp}{d\Psi} + \frac{F}{\mu_0 R} \frac{dF}{d\Psi} \quad (2.9)$$

Ampère's law relates the current density \mathbf{j} to the magnetic field \mathbf{B} , with the vacuum permeability μ_0 :

$$\mu_0 \mathbf{j} = \nabla \times \mathbf{B} \quad (2.10)$$

This gives an alternative expression for the toroidal current:

$$j_\varphi = \frac{1}{\mu_0} \left[\partial_R \left(\frac{1}{R} \partial_R \Psi \right) + \frac{1}{R} \partial_Z^2 \Psi \right] \quad (2.11)$$

By equating both expressions for j_φ , we arrive at the Grad-Shafranov equation [29, 71] for the poloidal flux:

2. Tokamak Concept – 2.1. Particles in a magnetized plasma

$$\Delta^* \Psi = R \partial_R \left(\frac{1}{R} \partial_R \Psi \right) + \partial_Z^2 \Psi = -\mu_0 R^2 \frac{dp}{d\Psi} - \mu_0 F \frac{dF}{d\Psi} \quad (2.12)$$

Here we introduced the Shafranov operator Δ^* . This equation is a second-order non-linear partial differential equation. The procedure outlined in Appendix A.1 solves Eq. 2.12 iteratively using a Newton-Krylov method. A typical solution for Ψ is illustrated in Fig. 2.3.

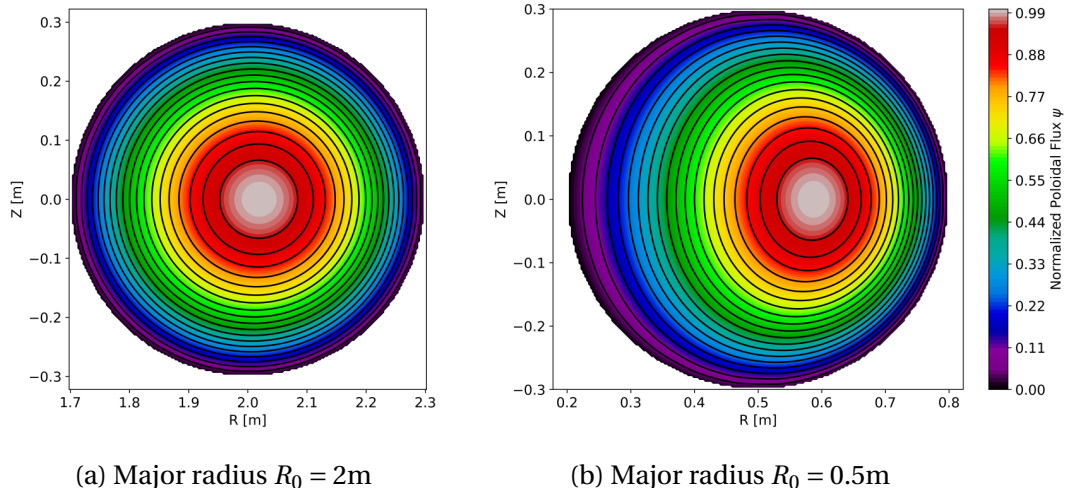


Figure 2.3.: Solution of the Grad-Shafranov equation on a circular cross-section with minor radius $a = 0.3$ m. A Cartesian mesh with $N = 200$ equidistant discretization points is used for the R and Z coordinates. The flux Ψ is forced to 0 at the boundary. The toroidal magnetic field is given by $B_\varphi = B_0 R_0 / R$ with $B_0 = 1\text{T}$. The pressure follows an exponential distribution $p(\Psi) = p_0(e^{-\Psi} - 1)$ with $p_0 = 1\text{ MPa}$.

The plasma pressure causes the magnetic axis to shift outward in a phenomenon known as the Grad-Shafranov shift. The radial displacement from the centerline of the torus can be approximated by:

$$\Delta \approx \frac{2\mu_0 p}{B_p} \frac{a^2}{R_0} \quad (2.13)$$

The two scenarios presented in Fig. 2.3 differ by their major radius. As the Grad-Shafranov shift is inversely proportional to R_0 , we expect that the larger curvature in the case 2.3b $R_0 = 0.5\text{m}$ induces a larger shift, which is precisely what is observed.

2.1.4. Realisation of magnetic configurations

The magnetic tokamak configuration in a tokamak is controlled by a set of coils. An example of the technical realisation in the ITER tokamak is shown in Fig. ???. The fundamental configuration discussed before, is created by the toroidal field coils

2. Tokamak Concept – 2.1. Particles in a magnetized plasma

encircling the plasma chamber, appear in orange on the scheme. As it from the name, they drive the toroidal magnetic field B_φ . The poloidal field, necessary for the helical path of confined plasma particles, is driven by a strong toroidal current, itself induced by the central solenoid (central column with yellow ends).

They are completed by poloidal field coils (light purple), placed outside the main plasma chamber and distributed along the height of the tokamak. They generate a poloidal magnetic field that wraps around the plasma with the minor radius, perpendicular to the toroidal field. By adjusting the current, it is possible to control the vertical position, elongation, and triangularity of the plasma. For example, increasing the current in certain poloidal coils can elongate the plasma, giving it an oval cross-section, or induce triangularity by pulling the plasma boundary inward at the top and bottom.

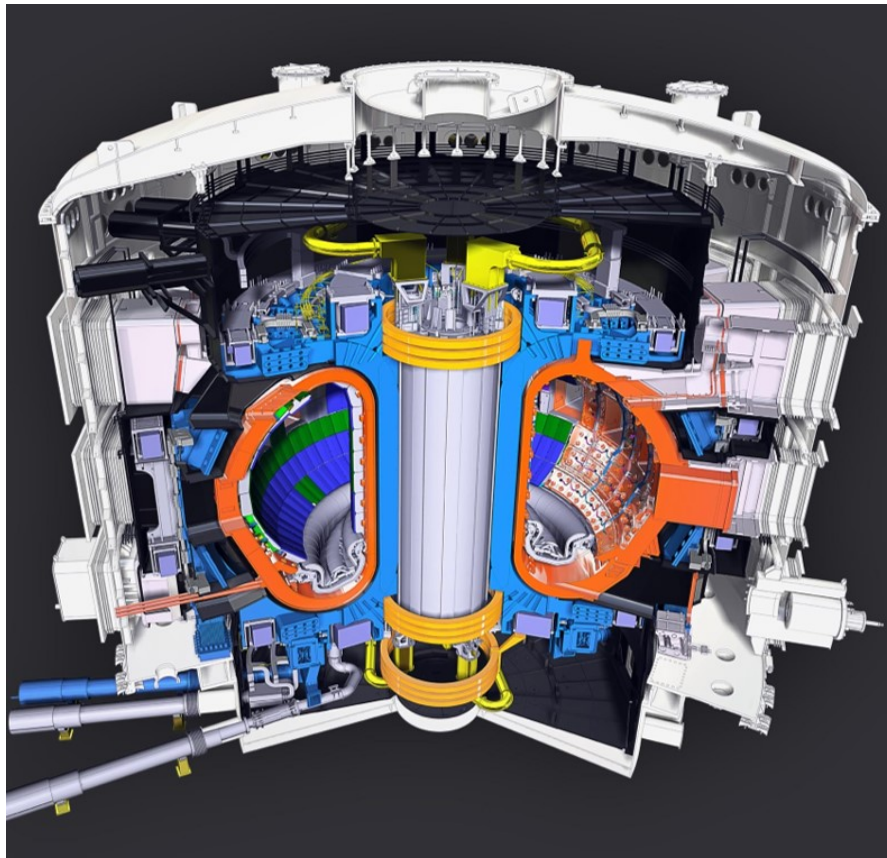


Figure 2.4.: Cutaway of the ITER tokamak (source: ITER Organization)

The limited configuration is one of the simpler magnetic configurations in a tokamak. In this setup, the plasma is in direct contact with material components which act as a limiter (see Fig. 2.5a). The confined plasma boundary is given by the last closed flux surface, tangential to the wall in one point. Such a configuration suffers from significant power loads on the limiters, resulting in high erosion rates and potential contamination of the plasma with impurities. The confinement is generally lower in

2. Tokamak Concept – 2.1. Particles in a magnetized plasma

this configuration.

A diverted configuration, as depicted in Fig. 2.5b, improves the situation by a lot. The poloidal field coils shape the magnetic field lines in a fashion that they do not intersect with solid surfaces within the main plasma chamber but are instead directed to a separate region called the divertor. The last closed flux surface is then called "separatrix" and never touches the tokamak wall. It effectively splits the domain in a confined core region with closed field lines and the Scrape-Off-Layer (SOL), that extends to the wall and where field lines are open, e.g. they cross the wall. The poloidal magnetic field contains now a singularity, the "X-point", and the area where the divertor plate intercepts the continuation of the separatrix is called the "target line". The divertor handles the exhaust of heat and particles from the plasma and this configuration tends to improve overall plasma confinement and reduce impurity levels.

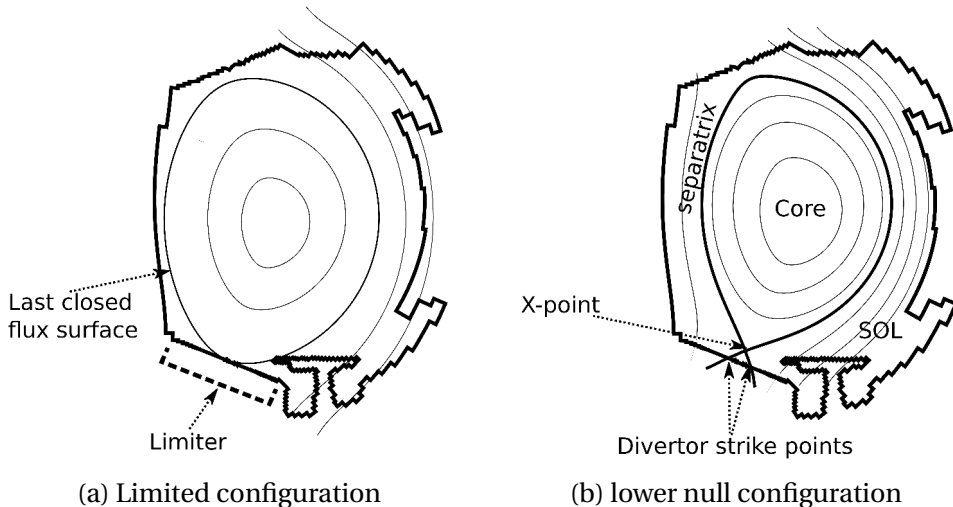


Figure 2.5.: Comparison of the limited and diverted configuration on a WEST geometry.

More exotic configurations are also feasible. In the double-null configuration, there are two divertor regions, typically located above and below the main plasma body. It splits heat loads on both divertor targets and can improve symmetry in power and particle exhaust. This symmetry helps in balancing the plasma dynamics and stabilizing the plasma, particularly with respect to vertical displacement events (VDEs), which are large-scale instabilities that can occur in tokamaks. Similarly, the X-point can be a higher-order singularity and split in more than four branches, spreading the heat load in several branches[67]. Such "snowflake" divertors can be achieved with an additional set of poloidal field coils in proximity to the divertor.

Another important parameter of the magnetic configuration is its triangularity. It refers to the shaping of the plasma cross-section, where the plasma boundary is not circular but has an elongated shape with triangular indentations. The degree of triangularity δ measures the extent of the indentation relative to the plasma's minor radius.

2. Tokamak Concept – 2.2. Interaction between particles

High triangularity configurations can enhance plasma stability and confinement, in particular in the edge region, by allowing for higher pressure gradients.

2.2. Interaction between particles

So far we have seen how particles are confined in magnetic field lines. It gives only a partial picture of the physical processes that occur in a tokamak. A plasma contains positively and negatively charged particles at high energetic levels and they will inevitably interact between themselves. In Sec. 2.2.1 we look at how electrons and ions organize to form a state of quasi-neutrality, in Sec. 2.2.2 we dive into the mechanisms that drive particle collisions and in Sec. ?? we conclude how collisions translate into resistive effects.

2.2.1. Debye shielding

Debye shielding refers to the macroscopic phenomenon that electric fields naturally dissipate in a plasma at rest. When a charged particle is introduced into a plasma, electrons, being lighter and more responsive than ions, quickly redistribute themselves around the introduced charge. There is then a localized region of increased electron density that counteracts the introduced electric field. The characteristic length over which this electric field is significantly attenuated is known as the Debye length λ_D :

$$\lambda_D = \sqrt{\frac{\epsilon_0 T_e}{n_e e^2}} \quad (2.14)$$

The Coulomb potential around a point charge Q exponentially decreases for distances beyond the Debye length:

$$\Phi(r) = \frac{Q}{4\pi\epsilon_0 r} e^{-r/\lambda_D} \quad (2.15)$$

It effectively means that at scales larger than λ_D , the plasma can be considered quasi-neutral, where the electron density compensates the charge of all present ions.

$$n_e = \sum_i q_i n_i \quad (2.16)$$

2.2.2. Particle collisions

At scales below the Debye length, the Coulomb force

$$\mathbf{F}_C = \frac{q_1 q_2}{4\pi\epsilon_0} \frac{\mathbf{r}}{\|\mathbf{r}\|^3} \quad (2.17)$$

drives collisions between two particles with charges q_1 and q_2 at a distance $\mathbf{r} = \mathbf{r}_2 - \mathbf{r}_1$, where ϵ_0 is the vacuum permittivity. By Newton's first and third laws of motion, this

2. Tokamak Concept – 2.2. Interaction between particles

force defines the acceleration of each particle $m_{1/2} \frac{d^2 \mathbf{r}_{1,2}}{dt^2} = \mathbf{F}_{12/21}$ and acts in opposite directions $\mathbf{F}_{12} = -\mathbf{F}_{21}$ for the respective particles.

Following the derivation in Chapter 3 of Hutchinson et al. [41], we can combine the two equations of motion to express the dynamics of a single particle (projectile) with position \mathbf{r} and reduced mass $m_r = \frac{m_1 m_2}{m_1 + m_2}$, that collides with a stationary second particle (target) at the origin. This description corresponds to a reference frame attached to the common center of mass. For an initial velocity \mathbf{v}_r , the projectile will be deviated by the collision as represented in Fig. 2.6.

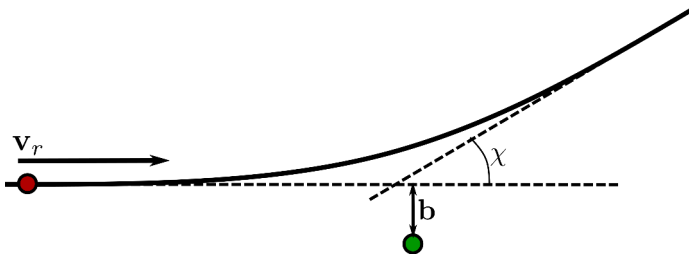


Figure 2.6.: Trajectory of the projectile particle (red) colliding with the target particle (green). The vector \mathbf{b} denotes the impact factor and χ is the deflection angle caused by the collision.

To conserve angular momentum, the deflection of the projectile depends on the impact factor or the distance $b = \|\mathbf{b}\|$ of the initial trajectory to the target. Let

$$b_{90} = \frac{q_1 q_2}{4\pi\epsilon_0} \frac{1}{m_r \|\mathbf{v}_r\|^2} \quad (2.18)$$

be the impact factor at which the projectile is deflected by a 90° angle. We can then express the deflection angle χ at a given b :

$$\chi = \tan^{-1} \frac{b_{90}}{b} \quad (2.19)$$

This angle represents the deflection of the particle relative to the common center of mass. If we now consider two individual particles with finite mass, where the projectile approaches a stationary target with velocity $\mathbf{v}_1 = (v_1, 0)^T$, the deflection observed in an external frame is approximately $\chi_1 \approx \frac{m_2}{m_1 + m_2} \chi$ (using the small angle approximation). To conserve momentum in the initial direction, the target also starts moving. The projectile exits the collision with:

$$\mathbf{v}'_1 = \left(\frac{\frac{m_1 v_1}{m_1 + m_2} + \frac{m_2 v_1}{m_1 + m_2} \cos \chi}{\frac{m_2 v_1}{m_1 + m_2} \sin \chi} \right) \quad (2.20)$$

2. Tokamak Concept – 2.2. Interaction between particles

At each collision, kinetic energy is transferred, and the projectile loses:

$$\begin{aligned}\Delta K = K - K' &= \frac{1}{2} m_1 \|\mathbf{v}_1\|^2 - \frac{1}{2} m_1 \|\mathbf{v}'_1\|^2 \\ &= \frac{2m_1^2 m_2}{(m_1 + m_2)^2} v_1^2 \sin^2 \frac{\chi}{2} \\ &\approx \frac{2m_1^2 m_2}{(m_1 + m_2)^2} v_1^2 \left(\frac{b_{90}}{b} \right)^2\end{aligned}\quad (2.21)$$

where the last line uses the small angle approximation $\chi \ll 1$.

In practice, we do not want to study every collision but are interested in the total number of collisions a particle experiences over a given length when traversing a medium with density n . For that, we consider all collisions with particles at an impact factor between b and $b + db$ over a distance dx (see Fig. 2.7). This means we look at the volume $V = 2\pi bdbdx$ in which we count a total of nV collisions.

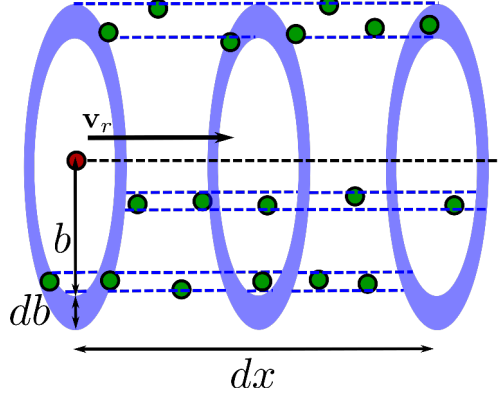


Figure 2.7.: Volume for given db and dx in which collisions on the projectile are considered.

Using Eq. 2.21 for the energy loss at each collision, we can estimate the energy our projectile loses after all collisions with the targets in the volume:

$$\Delta_V K = \frac{2m_1^2 m_2}{(m_1 + m_2)^2} v_1^2 \left(\frac{b_{90}}{b} \right)^2 n 2\pi bdbdx \quad (2.22)$$

The stopping power $\frac{dK}{dx}$ describes the rate of energy loss per unit path length. It requires integrating over all possible impact factors b :

$$\frac{dK}{dx} = \frac{2m_1^2 m_2}{(m_1 + m_2)^2} v_1^2 n 2\pi b_{90}^2 \int_{b_{min}}^{b_{max}} \frac{1}{b} db \quad (2.23)$$

This integral diverges in both limits $b_{min} \rightarrow 0$ and $b_{max} \rightarrow \infty$. We need to define cut-off values:

- $b_{min} = b_{90}$ because the small angle approximation in Eq. 2.21 implies that

2. Tokamak Concept – 2.2. Interaction between particles

$$b > b_{90}$$

- $b_{max} = \lambda_D$ because the Coulomb potential from Eq. 2.15 vanishes quickly at distances beyond the Debye length and so does the effective Coulomb force \mathbf{F}_C

With these bounds, we evaluate the integral and define the Coulomb logarithm:

$$\ln \Lambda = \int_{b_{90}}^{\lambda_D} \frac{1}{b} db = \ln \left(\sqrt{\frac{\epsilon_0 T_e}{n_e e^2}} \right) - \ln \left(\frac{q_1 q_2}{4\pi \epsilon_0} \frac{1}{m_r \|\mathbf{v}_r\|^2} \right) \quad (2.24)$$

For ion-ion collisions, masses $m_1 = m_2$ and charges $q_1 = q_2$ are equal. The collision frequency ω_c describes at which rate a particle loses energy through collisions relative to its total energy. The power loss is proportional to the stopping power with the particle velocity $\frac{dK}{dt} = v \frac{dK}{dx}$. We can then relate ω_c to the stopping power:

$$\omega_c = \frac{v}{K} \frac{dK}{dx} \quad (2.25)$$

If we now inject Eqs. 2.19, 2.23 and 2.24 we obtain following expression for ω_c :

$$\omega_c = \frac{q^4 n}{16\pi \epsilon_0^2 \sqrt{2m} K^{3/2}} \ln \Lambda \quad (2.26)$$

Assuming that the kinetic energy follows directly the plasma temperature with the relation $K = 3/2T$, we can express the characteristic collision time τ_c and mean free path λ_c :

$$\tau_c = \frac{1}{\omega_c} = \frac{52\sqrt{3}\pi \epsilon_0^2 \sqrt{m}}{q^4 \ln \Lambda} \frac{T^{3/2}}{n} \quad (2.27)$$

$$\lambda_c = \frac{v}{\omega_c} = \frac{32\sqrt{3/2}\pi \epsilon_0^2}{q^4 \ln \Lambda} \frac{T^2}{n} \quad (2.28)$$

It is worth noting that τ_c is proportional to $T^{3/2}/n$ and λ_c to T^2/n as all other terms are near-constant for a given ion in a tokamak.

2.2.3. Macroscopic effects of plasma collisions

!!!!!!

Spitzer-Härm model:

Shortly state viscosity, heat resistivity and electric resistivity !

!!!!!!

2.3. Scrape-Off-Layer

!!!!!! Add Intro !!!!!!!

2.3.1. Fundamental sheath physics

The SOL is characterized by open flux surfaces and where magnetic field lines cross the wall, the quasi-neutrality assumption from Sec. 2.2.1 does not hold anymore. The much lighter electrons travel much faster towards the wall (about $\sqrt{m_i/m_e}$ faster than ions), creating a net negative charge in the direct proximity to the wall. It is not until a few Debye lengths λ_D before shielding restores known plasma conditions forming a region known as "electrostatic sheath". The negative charge attracts ions and repulses electrons, and we can assume that the electron density decreases exponentially approaching the wall. This eventually leads to the Bohm criterion[61], which states that at the sheath entrance the ion speed must be equal or larger than the sound speed of the plasma.

$$v_{se} \geq c_s = \sqrt{\frac{T_i + T_e}{m_i}} \quad (2.29)$$

From there, it is possible to calculate a sheath particle flux:

$$\gamma_{se} = n v_{se} \quad (2.30)$$

and a heat flux:

$$q_{se} = \gamma n T \gamma_{se} \quad (2.31)$$

with the sheath transmission coefficient γ . As the sheath is not collisional, these coefficients have to be determined from kinetic theory[73]. For hydrogen plasma, it is common to take the values $\gamma_i = 2.5$ for ions and $\gamma_e = 4.5$ for electrons.

2.3.2. Confinement characteristics

An important metric for the confinement quality is the ratio β of plasma pressure over magnetic pressure.

$$\beta = \frac{p}{p_{mag}} = \frac{n e T}{B^2 / 2\mu_0} \quad (2.32)$$

There is a concurrent dynamic between thermodynamic and magnetic pressures: the former exerts an expansive force on the plasma, while the latter seeks to confine the plasma particles within their magnetic flux surfaces. A lower value of β is generally desired for a more effective plasma confinement, but requires strong magnetic fields. However, generating such intense magnetic fields entails considerable costs and technical challenges. β typically takes values between 1% and 5% in present large tokamaks.

It is possible to distinguish between two operational regimes: L-mode and H-mode. The (L)ow-confinement mode is the standard operational mode. The plasma loses much of its energy to the wall with a consequent short confinement time. In 1982, the (H)igh-confinement mode was first observed on ASDEX in Germany and subsequently thoroughly investigated[78]. Its key feature is a strong reduction of turbulence around the separatrix, which reduces particle transport from the core to the SOL. As a consequence, temperature and density gradients steepen, forming a "pedestal" and creating a transport barrier.

2.3.3. Problematic of heat exhaust

An important part of the heat produced in a tokamak, whether it originates from external heating or from the fusion reaction, is evacuated by hot plasma particles. Cross-field transport allows confined particles from the hot core to cross the separatrix. As they enter the SOL, they follow the magnetic field lines until they impact the divertor on the thin target band. This region is extremely critical as large amounts of power are directed on a fairly small area. It is projected for ITER that heat loads at the targets are very close to material limits[31]. The peak heat flux q_{peak} could reach values over $10MW/m^2$. For a safe tokamak operation, it is essential to well understand and predict heat fluxes on the strike points. An important metric to take into the consideration is the heat flux o power fall-off width λ_q . It describes the spread of the heat flux on the divertor targets, and a larger value allows to spread the power exhaust on a larger area. It allows to describe the heat flux at a distance r from the target:

$$q(r) = q_{peak} e^{-\frac{r}{\lambda_q}} \quad (2.33)$$

Eich et al.[24] developed a scaling law to estimate λ_q for H-mode operation based on machine parameters. It states that the width is inversely proportional to the toroidal magnetic field $\lambda_q \propto B_\phi^{-0.8}$, meaning that larger machines with stronger coils will also have a thinner target line.

3. Description of Plasmas

Plasmas can be modeled using various sets of equations that trade off between accuracy and computational feasibility. Generally, more accurate models are prohibitively expensive and are beyond the capabilities of current high-performance computing (HPC) infrastructure when applied to large systems. In this chapter, we introduce the major approaches that are used nowadays, with a special care to highlight how they are connected and where they differ. The most comprehensive approach in Sec. 3.1 rely on plasma particles themselves or their statistical distribution. From there, the Chapman-Enskog expansion in Sec. 3.2 allows to express conservation equations on averaged plasma quantities and lay the foundations for fluid models. Finally, MHD models in Sec. 3.3 offer a framework to combine those conservation equations with the evolution of electromagnetic properties of the plasma.

3.1. Direct description of Plasma Particles

Particles are the foundation of the first set of models. They can either be solved individually as in Sec. 3.1.1 or represented by their distribution functions in the so-called kinetic models (Sec. 3.1.2).

3.1.1. Particle Tracking

In the most general description, each particle in a tokamak—whether neutron, ion, atom, or electron—is represented individually with three degrees of freedom for both position \mathbf{x} and velocity \mathbf{v} . The system’s dynamics are governed by the Lorentz force:

$$\frac{\partial \mathbf{v}}{\partial t} = \mathbf{F} = q\mathbf{E} + q\mathbf{v} \times \mathbf{B} \quad (3.1)$$

$$\frac{\partial \mathbf{x}}{\partial t} = \mathbf{v} \quad (3.2)$$

where \mathbf{E} is the electric field, \mathbf{B} the magnetic field, and q the charge of the particle. Given that a medium-sized tokamak like WEST contains approximately $N_p \approx 10^{20}$ particles, each with six degrees of freedom, direct numerical simulation is infeasible. Computational effort can be reduced by using macro-particles, which represent many real particles. A prominent approach utilizing this concept is the particle-in-cell (PIC) method [79], where macro-particles evolve in pre-calculated fields on a mesh or interact directly with one another. PIC methods are employed to study phenomena such

as collisions with neutral particles [2], plasma-wall interactions [44], or instabilities induced by fusion products [13].

3.1.2. Kinetic Models

As a further abstraction, an ensemble of particles can be described statistically through a distribution function $f(\mathbf{x}, \mathbf{v}, t)$. This kinetic description replaces individual particles with a probability distribution, avoiding the need to calculate exact positions and velocities at each moment in time. The behavior of the distribution function is governed by the Boltzmann equation:

$$\frac{\partial f}{\partial t} + \mathbf{v} \cdot \nabla_{\mathbf{x}} f + \frac{\mathbf{F}}{m} \cdot \nabla_{\mathbf{v}} f = C_{\text{coll}} + C_{\text{other}} \quad (3.3)$$

where C_{coll} represents the collision operator, handling Coulomb collisions as introduced in Sec. 2.2.2, and C_{other} includes additional source terms. Substituting the force vector \mathbf{F} with the Lorentz force (Eq. 3.1) yields the Vlasov equation.

To achieve sufficient accuracy, approximately $N_x = 10^9$ spatial discretization points and $N_\sigma = 10^6$ points for the distribution function are required. Considering that both position and velocity have three components each, this results in $6 \cdot 10^{15}$ degrees of freedom—significantly fewer than in the particle description.

Further simplification is achieved through the gyrokinetic approach. While particles in a plasma predominantly follow magnetic field lines, their motion forms a helical trajectory characterized by the Larmor frequency and radius:

$$\omega_L = \frac{qB}{m} \quad l_L = \frac{mv_\perp}{qB} \quad (3.4)$$

This allows the elimination of one degree of freedom in the distribution function, as the velocity can be described by its parallel component v_\parallel along the magnetic field line and its perpendicular component v_\perp . This simplification is valid only when the Larmor frequency and radius are much smaller than any characteristic frequency or length in the system, which is typically true in the core of the tokamak but not in the scrape-off layer (SOL), where the gyrokinetic approach is less suitable.

3.2. Three Fluid Moments of the Kinetic Equation

Deriving transport equations for plasma quantities analogous to the Navier-Stokes equations in classical fluid dynamics is highly desirable. Such an approach would enable the use of established computational fluid dynamics (CFD) methods for turbulence modeling, significantly reducing the number of degrees of freedom. Starting with the distribution function f , the k -th moment of the transport equation is obtained by applying the tensor product $\mathbf{v} \otimes \dots$ k times and then integrating over the velocity:

3. Description of Plasmas – 3.2. Three Fluid Moments of the Kinetic Equation

$$\mathcal{M}^k = \int_{\mathbf{v}} f \mathbf{v}^k d\mathbf{v}^3 \quad (3.5)$$

Substituting the kinetic equation 3.3 into this expression yields the following equation for the k -th moment:

$$\begin{aligned} \partial_t \int_{\mathbf{v}} f \mathbf{v}^k d\mathbf{v}^3 + \int_{\mathbf{v}} \mathbf{v}^k \nabla_{\mathbf{x}} f d\mathbf{v}^3 + \int_{\mathbf{v}} \mathbf{v}^k \frac{\mathbf{F}}{m} \cdot \nabla_{\mathbf{v}} f d\mathbf{v}^3 &= \int_{\mathbf{v}} \mathbf{v}^k C d\mathbf{v}^3 \\ \partial_t \mathcal{M}^k + \nabla_{\mathbf{x}} \cdot \mathcal{M}^{k+1} - \frac{k}{m} \mathbf{F} \otimes \mathcal{M}^{k-1} &= \int_{\mathbf{v}} \mathbf{v}^k C d\mathbf{v}^3 \end{aligned} \quad (3.6)$$

Expressing the k -th moment requires knowledge of the $k-1$ -th and $k+1$ -th moments. Consequently, a fully consistent plasma description would require infinitely many equations, which is impractical. Therefore, we typically consider only the first three moments, using fluid closures to compensate for the missing higher-order equations. These moments effectively allow us to replace a particle-based description with averaged quantities:

$$\text{Particle density: } \mathcal{M}^0 = n = \int_{\mathbf{v}} f d\mathbf{v}^3 \quad [\text{m}^{-3}] \quad (3.7)$$

$$\text{Momentum density: } \mathcal{M}^1 = \boldsymbol{\gamma} = n \mathbf{u} = \int_{\mathbf{v}} f \mathbf{v} d\mathbf{v}^3 \quad [\text{m}^{-2} \cdot \text{s}^{-1}] \quad (3.8)$$

$$\text{Pressure tensor: } m \mathcal{M}^2 = \boldsymbol{\Pi} = m \int_{\mathbf{v}} f \mathbf{v} \otimes \mathbf{v} d\mathbf{v}^3 \quad [\text{kg} \cdot \text{m}^{-1} \cdot \text{s}^{-2}] \quad (3.9)$$

where \mathbf{u} is the fluid velocity and m the particle mass. This framework sets the stage for deriving the three fundamental conservation equations for fluid models of plasmas.

3.2.1. Mass Balance ($k = 0$)

Starting from Eq. 3.3, the mass balance equation for the unknowns n and \mathbf{u} is derived as follows:

$$\partial_t n + \nabla \cdot (n \mathbf{u}) = S_n \quad (3.10)$$

This equation provides one relation but involves four unknowns, necessitating additional equations to fully describe the system. The term S_n accounts for particle sources arising from non-elastic collisions in C_{other} , such as ionization or recombination processes.

3.2.2. Momentum Balance ($k = 1$)

For the first moment equation, we multiply the Boltzmann equation 3.3 by \mathbf{v} and integrate over the velocity space, yielding:

$$\partial_t \left(\int_{\mathbf{v}} \mathbf{v} f d\mathbf{v} \right) + \int_{\mathbf{v}} \mathbf{v} \otimes \mathbf{v} \cdot \nabla_{\mathbf{x}} f d\mathbf{v} + \int_{\mathbf{v}} \mathbf{v} \frac{\mathbf{F}}{m} \cdot \nabla_{\mathbf{v}} f d\mathbf{v} = \int_{\mathbf{v}} C v d\mathbf{v} \quad (3.11)$$

To simplify the tensor product, we decompose the velocity \mathbf{v} into the fluid velocity \mathbf{u} and a new quantity \mathbf{w} , such that $\mathbf{v} = \mathbf{u} + \mathbf{w}$. We introduce the static pressure tensor:

$$\mathbf{P} = m \int_{\mathbf{w}} f \mathbf{w} \otimes \mathbf{w} d\mathbf{w} \quad (3.12)$$

The pressure tensor $\mathbf{\Pi}$ can then be expressed as:

$$\mathbf{\Pi} = m \int_{\mathbf{w}} f \mathbf{u} \otimes \mathbf{u} d\mathbf{w} + m \int_{\mathbf{w}} f \mathbf{w} \otimes \mathbf{w} d\mathbf{w} = mn \mathbf{u} \otimes \mathbf{u} + \mathbf{P} \quad (3.13)$$

Substituting this into the first moment equation, we obtain the conservation equation for momentum:

$$m \partial_t (n \mathbf{u}) + m \nabla \cdot (n \mathbf{u} \otimes \mathbf{u} + \mathbf{P}) = q n \mathbf{E} + q n \mathbf{u} \times \mathbf{B} + S_u + R \quad (3.14)$$

Here, S_u represents the momentum source term, and R accounts for friction, both arising from C_{coll} and C_{other} .

3.2.3. Energy Balance ($k = 2$)

Finally, to solve for the static pressure tensor \mathbf{P} , we assume isotropic pressure in the plasma, simplifying the pressure tensor to a scalar pressure p such that $\mathbf{P} = p \mathbf{I}$. This reduces the nine unknowns in \mathbf{P} to a single scalar p . Given that $p = nT$, the second moment can be expressed as an energy conservation equation. The total energy density ϵ is the sum of kinetic and thermal energy in the plasma:

$$\epsilon = \frac{3}{2} n T + \frac{1}{2} m n \|\mathbf{u}\|^2 \quad (3.15)$$

To derive a conservation equation for ϵ , we multiply Vlasov's equation 3.3 by the kinetic energy per unit mass:

$$\partial_t \left(\int_{\mathbf{v}} \frac{1}{2} u^2 f d\mathbf{v} \right) + \int_{\mathbf{v}} \frac{1}{2} u^2 \mathbf{v} \cdot \nabla_{\mathbf{x}} f d\mathbf{v} + \int_{\mathbf{v}} \frac{1}{2} u^2 \frac{\mathbf{F}}{m} \cdot \nabla_{\mathbf{v}} f d\mathbf{v} = \int_{\mathbf{v}} \frac{1}{2} u^2 C d\mathbf{v} \quad (3.16)$$

This simplifies to:

$$\partial_t \epsilon + t' \nabla \cdot (\epsilon \mathbf{u} + [n \mathbf{u} \otimes \mathbf{u} + \mathbf{P}] \cdot \mathbf{u} + \mathbf{q}) = q n \mathbf{E} \cdot \mathbf{u} + Q + R_{\epsilon} \quad (3.17)$$

The collisional heat flux \mathbf{q} arises from the fluid closure, replacing all higher-order moments. The term Q represents a collisional heat source, while R_e accounts for sources associated with non-Coulombian collisions in C_{other} . Notably, the magnetic field term $\mathbf{u} \times \mathbf{B}$ does not appear in the energy equation, as the torque $\frac{1}{2} u^2 \mathbf{u} \times \mathbf{B} \cdot \nabla_{\mathbf{v}} f$ does not perform work and therefore does not contribute to energy changes.

The three conservation equations for density n , momentum γ , and energy ϵ form the foundation of the SOLEDGE3X model. These terms will be further developed in Chapter ??.

3.3. MHD description of plasmas

In the magnetohydrodynamics (MHD) approach, the conservation equations are coupled to Maxwell's and Ohm's laws, introducing electromagnetic behavior into the system. Unlike earlier models, the magnetic equilibrium is not static; the electric and magnetic fields evolve over time. MHD models typically differentiate between ideal MHD and extended models that include resistive and two-fluid effects, which are essential for accurately describing tokamak plasmas. The ideal MHD model and its extension with tokamak-specific terms in Sec. 3.3.1 is the most accurate approach to simulate the electromagnetic intrications in plasmas. Fast wave dynamics represent a major restriction and reduced models in Sec. 3.3.2 are therefore much more widespread.

3.3.1. Extended MHD Model

Many of the explanations in this section are based on the lecture notes by E. Franck[50]. The complete set of MHD equations is as follows:

$$m\partial_t n + \nabla \cdot (n\mathbf{u}) = 0 \quad (3.18)$$

$$mn\partial_t \mathbf{u} + mn\mathbf{u} \cdot \nabla \mathbf{u} + \nabla p = \mathbf{j} \times \mathbf{B} \boxed{-\nabla \cdot \boldsymbol{\Pi}} \quad (3.19)$$

$$\frac{3}{2}\partial_t p_i + \frac{3}{2}\mathbf{u} \cdot \nabla p_i + \frac{5}{2}p_i \nabla \cdot \mathbf{u} = \boxed{-\nabla \cdot \mathbf{q}_i - \nabla \cdot (\boldsymbol{\Pi}_i : \nabla \mathbf{u})} \quad (3.20)$$

$$\frac{3}{2}\partial_t p_e + \frac{3}{2}\mathbf{u} \cdot \nabla p_e + \frac{5}{2}p_e \nabla \cdot \mathbf{u} = \boxed{-\nabla \cdot \mathbf{q}_e - \nabla \cdot (\boldsymbol{\Pi}_e : \nabla \mathbf{u}) + \eta \|\mathbf{j}\|^2 + \frac{3}{2}\mathbf{j} \cdot \mathcal{P}} \quad (3.21)$$

$$\partial_t \mathbf{B} = -\nabla \times \left(-\mathbf{u} \times \mathbf{B} \boxed{+ \eta \mathbf{j} - \mathcal{P} + \mathcal{H}} \right) \quad (3.22)$$

$$\nabla \cdot \mathbf{B} = 0 \quad (3.23)$$

$$\nabla \times \mathbf{B} = \mu_0 \mathbf{j} \quad (3.24)$$

Equations 3.18 through 3.24 are derived directly from the fluid moments described in Sec. 3.2, where the pressure replaces the energy and is solved for both ions and electrons. These equations are coupled with Ohm's law (Eq. 3.22) under the magnetostatic assumption, Gauss's law for magnetism (Eq. 3.23), and Ampère's law (Eq.

[3.24](#)). In ideal steady-state, we see that the momentum balance is dominated by the equilibrium between thermodynamic and magnetic forces $\nabla p = \mathbf{j} \times \mathbf{B}$. In combination with Ampère's law, all components are available to derive the Grad-Shafranov equation [2.12](#) as it has been done in Sec. [2.1.3](#).

The terms enclosed in boxes represent the additional terms required for extending the model from ideal MHD. These include viscous-resistive effects, as well as a pressure term \mathcal{P} and a Hall term \mathcal{H} . Without these boxed terms, the system describes the ideal MHD model. Linearizing the ideal MHD equations results in three types of waves:

- **Alfvén waves:** These incompressible waves cause the magnetic field lines to bend and propagate only in the parallel direction. In the low-beta limit, their propagation speed, $v_A^2 = \frac{B^2}{mn\mu_0}$, is much greater than the speed of sound in the plasma, $c_s^2 = \frac{eT}{m}$.
- **Slow magnetoacoustic waves:** These waves propagate only in the parallel direction, causing compression in the plasma without perturbing the magnetic field lines. Their propagation speed v_s is similar to the speed of sound.
- **Fast magnetoacoustic waves:** These waves can propagate in any direction and compress magnetic field lines. They have a propagation speed approximately given by $v_f^2 = v_A^2 + c_s^2$.

Fast waves, in particular, pose challenges for numerical modeling as they require very small timesteps and implicit methods to be accurately resolved. The full MHD model introduces two additional dispersive waves into the system.

3.3.2. Reduced MHD model

To eliminate the fast magnetoacoustic waves and to reduce the size of the system, physicists often resort to reduced MHD models. Instead of solving for all components of \mathbf{B} , we decompose the magnetic field into the poloidal flux Ψ and the toroidal field function F as in Eq. [2.7](#). The toroidal field B_φ and F are imposed, so we only remain with the unknown scalar Ψ to replace the three unknowns of \mathbf{B} . As a reminder from Sec. [2.1.3](#), Ψ is equivalent to the toroidal component A_φ of the magnetic vector potential and uniquely defines the poloidal field B_p . Consequently, Ampère's law [3.24](#) reduces to:

$$\mu_0 j_\varphi = \Delta^* \Psi = R^2 \nabla \cdot \left(\frac{1}{R^2} \nabla_p \Psi \right) \quad (3.25)$$

with the poloidal gradient ∇_p .

In the second simplification for the reduced MHD model, the velocity vector is decomposed into a parallel and a perpendicular component. The projected fields are:

$$u_{\perp} = \mathbf{e}_{\varphi} \cdot \nabla \times (R^2 \mathbf{u}) \quad (3.26)$$

$$u_{\parallel} = \mathbf{B} \cdot \mathbf{u} \quad (3.27)$$

$$(3.28)$$

This projection is consequently applied to all terms in the momentum conservation equation 3.19, that can then be solved independently for both velocities. In addition to reducing the number of equations from three to two, it permits to split the slow magnetoacoustic waves, that propagate at sound speed in the parallel directions, from the much slower dynamics in the poloidal plane that consist of electric and diamagnetic drifts (A proper introduction to the various plasma drifts will be given in the next chapter).

3.3.3. Reduced Ohm's law

!!!!!! Introduce reduced Ohm's law here !!!!!!

3.4. Fluid closures

We only considered MHD models up to the second moment. To maintain the validity of the model, we need additional closure terms in the momentum and energy equations. They rely on the fact that plasma collisions dominate higher-order moments.

!!!!!! Shortly present Braginskii / Zhdanov !!!!!

4. Drift-reduced models for plasma turbulence

The mechanisms at play at the plasma boundary result from the complex interplay of transport processes in the plasma, losses at the wall, and complex atomic and molecular interactions. In this region, particles experience very fast transport along the magnetic field lines and slower, often turbulence-driven, anomalous cross-field transport [51]. The ratio between these phenomena characterizes the decay length of density and temperature profiles, which further determine the confinement quality of the core plasma and the total heat exhaust on the divertor target.

The difficulty in obtaining global experimental measurements in tokamaks requires complementary numerical simulations. Currently, these numerical data are essential to complement experimental measurements and support their interpretation. In the longer term, they will be used to make predictions and support the design of ITER experiments. Self-consistent simulations of the plasma edge are challenged by a complex geometry and the variety of involved scales. The magnetic equilibrium exhibits both open and closed magnetic field lines, breaking the toroidal symmetry. Turbulent fluctuations typically have sizes on the order of the ion gyroradius ρ_α (≥ 0.4 mm) [39] in the perpendicular direction to the magnetic field lines, and compete with phenomena occurring along them on the order of the parallel connection length $\propto q_s R_0$ (where q_s is the safety factor, and R_0 the tokamak major radius), which can extend up to 100 meters.

In this context, kinetic models based on the particle distribution function [18, 43] are still limited to fundamental studies because of their very high numerical cost in a (5) 6-dimensional phase space. Thus, when realistic configurations are considered, reduced-dimension (2D/3D) fluid models remain the only feasible option for studying transport and turbulence at the edge of the plasma, although they are only rigorously valid in collisional regimes. A wide range of models have been derived in the literature and implemented in state-of-the-art codes [22, 28, 74] (see also an exhaustive presentation in the recent review by Schwander et al. [68]). The basic assumption they share is that the turbulence is characteristically low frequency and long wavelength in nature, leading to a strong scale separation between the parallel and perpendicular directions to the magnetic field. Therefore, the plasma fluid motion perpendicular to the magnetic field can be described explicitly by the so-called velocity drifts given by the quasi-static balance between Lorentz force, pressure gradient, and electromotive force due to magnetic and electric field inhomogeneities.

Sec. 4.1 introduces the origin of drift waves, main driver for plasma turbulence, and the drift-ordering approximation that typically applied in edge plasma.

4.1. Drift wave turbulence

4.1.1. Plasma drifts

Plasma drifts refer to the movement of charged particles under the influence of electric and magnetic fields. These drifts do not account for the primary motion along the guiding center, as described in Section 2.1.1. To study drift velocities, it is convenient to decompose every vector quantity into an average parallel component and a fluctuating perpendicular component, such that $\mathbf{X} = X_{\parallel}\mathbf{b} + \mathbf{X}_{\perp}$. We then express the Lorentz force equation as:

$$m\partial_t(v_{\parallel}\mathbf{b} + \mathbf{v}_{\perp}) = q [E_{\parallel}\mathbf{b} + \mathbf{E}_{\perp} + (v_{\parallel}\mathbf{b} + \mathbf{v}_{\perp}) \times \mathbf{B}] \quad (4.1)$$

Focusing on the particle's acceleration in the perpendicular direction, we derive the equation of motion:

$$m\partial_t\mathbf{v}_{\perp} = q [\mathbf{E} + (\mathbf{v}_{\perp} \times \mathbf{B})] \quad (4.2)$$

In steady-state conditions, the electric force compensates the Lorentz force, leading to the electric drift \mathbf{v}_E , commonly referred to as the "E cross B" or simply "ExB" drift:

$$\mathbf{v}_E = \frac{\mathbf{E}_{\perp} \times \mathbf{B}}{B^2} \quad (4.3)$$

This velocity applies uniformly to all particles at all times, as it depends only on the electric and magnetic fields in place. Since neither the mass nor the charge contributes to \mathbf{v}_E , both electrons and ions move in the same direction at the same speed, and under the quasi-neutrality assumption, no current is generated.

For the next drift, we consider the gyromotion of a particle in a non-uniform magnetic field. Under the adiabatic condition from Eq. 2.4, the magnetic moment μ of the gyrating particle is conserved along its trajectory:

$$\mu = \frac{m\|\mathbf{v}_{\perp}\|^2}{2B} \quad (4.4)$$

This moment leads to a potential $U = -\mu B$, which exerts a force on the particle:

$$F_{\nabla B} = -\nabla U = \frac{mv_{\perp}^2}{2B} \nabla B \quad (4.5)$$

This force acts in the direction of the gradient ∇B , where the magnetic field strength is lower, allowing the particle to reduce its potential energy. This results in the "grad B" drift:

$$\mathbf{v}_{\nabla B} = \frac{mv_{\perp}^2}{2q} \frac{\mathbf{B} \times \nabla B}{B^3} \quad (4.6)$$

The helical configuration of a tokamak causes magnetic field lines to bend. To follow the direction of \mathbf{B} , the particle's trajectory is curved, and a centripetal force is exerted on the particle. With the curvature radius $\mathbf{R}_c = \mathbf{b} \cdot \nabla \mathbf{b}$, the force is given by:

$$\mathbf{F}_c = \frac{mv_{\parallel}^2}{R_c} \mathbf{R}_c = -mv_{\parallel}^2 \frac{\mathbf{B} \cdot \nabla \mathbf{B}}{B^2} \quad (4.7)$$

This force induces the "curvature" drift \mathbf{v}_c :

$$\mathbf{v}_c = \frac{mv_{\parallel}^2}{q} \frac{\mathbf{B} \times (\mathbf{B} \cdot \nabla \mathbf{B})}{B^4} \quad (4.8)$$

The polarization drift occurs if the electric field in the plasma varies with time.

$$\mathbf{v}_p = \frac{m}{qB^2} \frac{d\mathbf{E}}{dt} \quad (4.9)$$

Note that the directions of "grad B", curvature or polarization drifts depend on the particle's charge, causing electrons and ions to move in opposite directions and generating an effective current. The total perpendicular velocity acting on a confined particle is the sum of all these drifts:

$$\mathbf{v}_d = \mathbf{v}_E + \mathbf{v}_{\nabla B} + \mathbf{v}_c + \mathbf{v}_p \quad (4.10)$$

In fact, any force perpendicular to the magnetic field will cause a drift:

$$\mathbf{v}_F = \frac{\mathbf{B} \times \mathbf{F}_{\perp}}{qB^2} \quad (4.11)$$

All other eventual forces, such as magnetic or gravitational forces, play a subordinate role in the plasma edge and are usually not considered in fluid models. Drift velocities are always orientated in perpendicular direction to the magnetic fields. They do not interfere with (the averaged) parallel fluxes, at a magnitude of v_{th} , and are primarily responsible for cross-field fluxes.

4.1.2. Drift-ordering approximation

We focus on low- β collisional plasmas, typically found in the edge region of a tokamak. In such plasmas, we can define a characteristic length scale L_{\parallel} for parallel phenomena, which is on the order of the machine size (e.g., the major radius R), where gradients in plasma fields such as density, temperature, or magnetic field strength are established. The perpendicular scale L_{\perp} is characteristic of cross-field structures. These scales define the parallel and perpendicular wave numbers k_{\parallel} and k_{\perp} . In the drift ordering, the following relationships hold[72]:

$$\beta = \frac{2\mu_0(p_e + p_i)}{B^2} \ll 1 \quad \frac{\rho_L}{L_\perp} \sim \frac{\lambda_c}{L_\parallel} \ll 1 \quad (4.12)$$

where ρ_L is the ion Larmor radius, and λ_c is the mean free path between collisions. The electric force is much weaker than the magnetic force. Similarly, characteristic plasma frequencies should be much lower than the ion cyclotron frequency, giving rise to the following ordering parameters:

$$\epsilon_E = \frac{mE}{qB^2} \ll 1 \quad \epsilon_l = \frac{L_\perp}{L_\parallel} \ll 1 \quad \epsilon_t = \frac{\omega_\perp}{\omega_L} \ll 1 \quad (4.13)$$

The averaged gyromotion of particles is parallel to the magnetic field lines, with parallel velocities $v_\parallel \approx \sqrt{2T/m}$ consistent with the kinetic energy in the plasma. Drift velocities, on the other hand, are typically much slower. Since ∇B and the curvature radius R_c occur at machine scales L_\parallel , we can provide orders of magnitude for the three drifts introduced earlier:

$$v_E \sim \epsilon_E v_\parallel \quad v_{\nabla B} \sim \epsilon_l v_\parallel \quad v_c \sim \epsilon_l v_\parallel \quad v_p \sim \epsilon_t v_\parallel \quad (4.14)$$

This leads to the assumption in the Lorentz equation 4.1 that the perpendicular acceleration is negligible compared to parallel dynamics, such that $m\partial_t v_\perp \approx 0$. The perpendicular direction is assumed to always be in force equilibrium, allowing us to equate the terms $\mathbf{v} \times \mathbf{B}$ and \mathbf{E}_\perp . Consequently, the polarization drift can be rewritten as:

$$\mathbf{v}_p = \frac{m}{qB^2} \mathbf{B} \times \frac{d\mathbf{v}}{dt} \quad (4.15)$$

Unlike other drifts, the polarization drift depends on the variation of the total velocity. To still obtain an expression for \mathbf{v}_\perp , we compute it in two steps, first considering the zeroth-order and then the first-order drifts:

$$\mathbf{v}_\perp^{(0)} = \mathbf{v}_E + \mathbf{v} \nabla B + \mathbf{v}_c \quad (4.16)$$

$$\mathbf{v}_\perp^{(1)} = \mathbf{v}_\perp^{(0)} + \frac{m}{qB^2} \mathbf{B} \times \left(\partial_t + \left(v_\parallel \mathbf{b} + \mathbf{v}_\perp^{(1)} \right) \cdot \nabla \right) \mathbf{v}_\perp^{(0)} \quad (4.17)$$

In the first order, the evolution of the perpendicular electric field derives from the evolution of the potential gradient $d\mathbf{E}_\perp/dt = -d\nabla_\perp \Phi/dt$. The full electric field is given by:

$$\mathbf{E}_\perp = -\nabla_\perp \Phi \quad E_\parallel = -\nabla_\parallel \Phi - \partial_t A_\parallel \quad (4.18)$$

where the time variation $\partial_t A_{\parallel}$ accounts for magnetic induction effects.

For the perpendicular velocity, the momentum conservation equation requires several algebraic transformations:

$$\begin{aligned} \mathbf{b} \times [\partial_t (mn\mathbf{u}) + \nabla \cdot (mn\mathbf{u} \otimes \mathbf{u})] &= -\mathbf{b} \times \nabla p_{\perp} - \mathbf{b} \times \nabla \cdot \bar{\Pi} + nq\mathbf{b} \times \mathbf{E} \\ &\quad + nq(\mathbf{b} \times \mathbf{u} \times \mathbf{B}) + \mathbf{b} \times \mathbf{R} + \mathbf{b} \times \mathbf{S}_u \\ \Leftrightarrow \mathbf{u}_{\perp} &= \frac{\mathbf{b} \times \nabla p}{qnB} + \frac{\mathbf{b} \times \nabla \cdot \bar{\Pi}}{qnB} + \frac{\mathbf{E} \times \mathbf{b}}{B} - \frac{\mathbf{b} \times (R + S)}{qnB} \\ &\quad + \frac{\mathbf{b}}{qnB} \times (\partial_t (mn\mathbf{u}) + \nabla \cdot (mn\mathbf{u} \otimes \mathbf{u})) \end{aligned} \quad (4.19)$$

The expression for the perpendicular velocity \mathbf{u}_{\perp} is not explicit as the right-hand side depends on the full velocity vector. However, we can fairly well approximate it with two calculation steps. All terms that do not depend on u are first evaluated to get $\mathbf{u}_{\perp}^{(0)}$ (and with equation 5.11 we can also calculate $\mathbf{u}^{(0)}$), and then $\mathbf{u}_{\perp}^{(1)}$ is calculated by replacing every occurrence of \mathbf{u} by $\mathbf{u}^{(0)}$. The terms \mathbf{u}^* , \mathbf{u}_E , $\mathbf{u}_{\perp,\Pi}$, $\mathbf{u}_{\perp,S}$ and \mathbf{u}_p are respectively called diamagnetic, "E cross B", parallel viscous stress, friction force and polarization drifts.

$$\mathbf{u}_{\perp}^{(0)} = \frac{\mathbf{b} \times \nabla p}{qnB} + \frac{\mathbf{E} \times \mathbf{b}}{B} = \mathbf{u}^* + \mathbf{u}_E \quad (4.20)$$

$$\begin{aligned} \mathbf{u}_{\perp}^{(1)} &= \frac{\mathbf{b} \times \nabla \cdot \bar{\Pi}(\mathbf{u}^{(0)})}{qnB} - \frac{\mathbf{b} \times (R(\mathbf{u}^{(0)}) + S(\mathbf{u}^{(0)}))}{qnB} \\ &\quad + \frac{\mathbf{b}}{n\omega_c} \times (\partial_t (n\mathbf{u}^{(0)}) + \nabla \cdot (n\mathbf{u}^{(0)} \otimes \mathbf{u}^{(0)})) \end{aligned} \quad (4.21)$$

$$\mathbf{u}_{\perp} \approx \mathbf{u}_{\perp}^{(0)} + \mathbf{u}_{\perp}^{(1)} \quad (4.22)$$

This simplification holds because the contribution of $\mathbf{u}_{\perp}^{(1)}$ is small, of the order of τ_c/τ_{ad} or τ_c/τ_{coll} . Next, let us extract the divergence free contribution from the diamagnetic flux $n\mathbf{u}^*$.

$$\begin{aligned} n\mathbf{u}^* &= -\nabla \times \frac{p_{\perp}\mathbf{B}}{qB^2} + n\tilde{u}^* \\ \text{with: } \tilde{u}^* &= \frac{2T_{\perp}\mathbf{B} \times \nabla B}{qB^3} + \frac{T_{\perp}}{qB^2}\nabla \times \mathbf{B} \end{aligned} \quad (4.23)$$

The second term in \tilde{u}^* is usually very small and can be neglected if magnetic fields do not fluctuate.

The last term u_p in Equation 4.21 is called the polarization drift. A simple expression

for the associated flux can be found through algebraic manipulations and neglecting some small curvature terms.

$$n\mathbf{u}_p = \partial_t \omega - \nabla \cdot (\tilde{u}^{(0)} \otimes \omega)$$

with: $\omega = \frac{m}{qB^2} \left(n\nabla_{\perp}\Phi + \frac{1}{q}\nabla_{\perp} \left(p - \frac{\pi_{\parallel}}{3} \right) \right) - \frac{m}{q^2B^2} S_{u_{\perp}}$ (4.24)

The electric potential in the plasma appears here in the variable Φ and is a new unknown that needs to be solved for.

The separation of scales allows for fluid-drift models, where the parallel and perpendicular momentum equations are treated independently. Mikhailovskii and Tsypin[54] first described slow drift dynamics from a theoretical viewpoint in 1971 with $\rho_L = 0$. Hazeltine et al.[37] extended the framework to include a finite ion Larmor radius. To understand their approach, it is useful to introduce the vorticity $\boldsymbol{\Omega} = \nabla \times \mathbf{v}$, which measures the local rotation of a fluid element. It is a vector quantity, where the direction indicates the axis of rotation and its magnitude indicates the strength of the rotational motion. As perpendicular phenomena are essentially described by the parallel component of $\boldsymbol{\Omega}$, we only solve for the conservation of Ω_{\parallel} . Furthermore, assuming that the electric drift dominates the perpendicular direction, we can express:

$$\Omega_{\parallel} = \mathbf{b} \cdot \nabla \times \mathbf{v}_E = \nabla_{\perp}^2 \Phi + \frac{1}{n} \nabla_{\perp}^2 p$$
 (4.25)

Taking the curl of the perpendicular (drift) momentum balance, we obtain a conservation equation for the ion vorticity:

$$\frac{n_i m_i}{q_i B^2} (\partial_t \Omega_{\parallel} + (\nu_{i,\parallel} \mathbf{b} + \mathbf{v}_{i,\perp}) \cdot \nabla \Omega_{\parallel}) = \nabla \cdot (j_{\parallel} \mathbf{b} + \mathbf{j}_{\perp} - e \mathbf{v}_E)$$
 (4.26)

where the perpendicular current arises from drifts in opposite directions for electrons and ions, $\mathbf{j}_{\perp} = q_i n_i \mathbf{v}_{i,\perp} - q_e n_e \mathbf{v}_{e,\perp}$. There is a "grad B," curvature, and polarization current, but no "ExB" current, as the electric drift is independent of the species' mass and charge. The parallel current density is given by Ohm's law:

$$\eta_{\parallel} j_{\parallel} + \frac{m_e}{e} \frac{d j_{\parallel}}{dt} = E_{\parallel} + \frac{\nabla_{\parallel} p_e}{n_e e} + \frac{0.71}{e} \nabla_{\parallel} T_e$$
 (4.27)

A full derivation of the drift-reduced equations, including all possible terms, was provided by Simakov and Catto[72]. Notably, they derived a self-consistent expression for the ion parallel and gyroviscous stress tensors, ensuring full energy conservation in the fluid model.

4.1.3. Linear plasma instabilities

To understand how turbulent structures appear and travel in the plasma, it is essential to understand the physical mechanisms covered by the drift-reduced equations. In

this section, we delve into the different linear phenomena that appear plasma in the SOL.

4.1.3.1. Non-adiabatic drift waves

One key mechanism within this framework is the non-adiabatic density response to potential perturbations. In this context, resistivity induces a phase shift between density and potential perturbations, which can either amplify or dampen these perturbations. The Hasegawa-Wakatani model [34] provides a foundational understanding of this process. This model considers an isothermal plasma with an unsheared magnetic field, where particles are advected solely by the electric drift, and parallel ion motion is neglected. We assume that the magnetic field is purely toroidal, and radial density gradients are imposed by the pressure gradient. We then remain with two degrees of freedom on which to perform the linear analysis: a perpendicular, poloidal direction and a parallel, toroidal direction. Perturbations on any quantity are expressed as $X = X_0(\psi) + \tilde{X}(\theta, \varphi)$, with $\tilde{X}(\theta, \varphi) = \epsilon e^{i(-\omega t + k_\perp \theta + k_\parallel \varphi)}$ and the equilibrium fields X_0 varies across flux surfaces. Radial density gradients are imposed from the pressure gradient and can be approximated $\partial_\psi n_0 = \bar{n}_0 / \lambda_p$ where λ_p is a characteristic length for the pressure gradient. In a slab equations, the perpendicular direction is hence perpendicular to both the magnetic field and the density gradient. The governing equations are:

$$\partial_t n + \mathbf{v}_E \cdot \nabla n = \frac{1}{e} \nabla \cdot (j_\parallel \mathbf{b}) \quad (4.28)$$

$$\eta_\parallel j_\parallel = T_0 \nabla_\parallel \log(n) - \nabla_\parallel \Phi \quad (4.29)$$

$$\frac{n m_i}{B^2} (\partial_t \nabla_\perp^2 \Phi + \mathbf{v}_E \cdot \nabla \nabla_\perp^2 \Phi) = \nabla \cdot (j_\parallel \mathbf{b}) \quad (4.30)$$

The advection term by the electric drift can be expressed using Poisson brackets:

$$\begin{aligned} \mathbf{v}_E \cdot \nabla n &= -\frac{1}{B} (\nabla \Phi \times \mathbf{b}) \cdot \nabla n = -\frac{1}{B} (\partial_\theta \Phi \partial_\psi n - \partial_\psi \Phi \partial_\theta n) \\ &= -\frac{1}{B} [\Phi, n]_{\psi, \theta} \end{aligned} \quad (4.31)$$

The wavenumber vector \mathbf{k} contains both parallel and perpendicular components, such that in the Fourier space $k_\parallel^2 \sim \nabla_\parallel^2$ and $k_\perp^2 \sim \nabla_\perp^2$. Using the ion Larmor radius $\rho_L^2 = T_0 m_i / (e B^2)$, the dispersion relation for the system is:

$$\omega^2 + i \frac{1 + \rho_L^2 k_\perp^2}{\rho_L^2 k_\perp^2} \frac{T_0 k_\parallel^2}{e n_0 \eta_\parallel} \omega - i \frac{1}{\rho_L^2 k_\perp^2} \frac{T_0^2 k_\perp k_\parallel^2}{e n_0 B \lambda_p \eta_\parallel} = 0 \quad (4.32)$$

The solution to this system can be decomposed into a real component ω_* that corresponds to the natural frequency of the system and an imaginary component γ that describes the growth or damping rate. From the drift-ordering parameters, we

know that $k_{\perp}^2 \rho_L^2$ must be small, simplifying the system. If we assume the resistivity small, we can estimate the solutions:

$$\omega_* = \frac{T_e k_{\perp}}{B \lambda_p} \quad \gamma = \frac{\rho_L^2 k_{\perp}^2 e n_0 \eta_{\parallel}}{T_0 k_{\parallel}^2} \omega_*^2 \quad (4.33)$$

The system frequency ω_* is called the diamagnetic frequency and is driven by the density gradient. We observe that the growth rate γ is positive, indicating that under certain conditions, perturbations may grow indefinitely. The more resistive a plasma is, the faster perturbations grow and in an ideal plasma with zero resistivity, the system remains stable with the single real solution ω_* . In this case, the interaction is adiabatic, and density and potential oscillate in phase at the diamagnetic frequency.

4.1.3.2. Sound waves

Parallel ion motion produces sound waves. If we consider only the parallel velocity, the conservation equation can be expressed in a reduced form:

$$\partial_t n + \nabla \cdot (v_{\parallel} n \mathbf{b}) = 0 \quad (4.34)$$

$$m_i n \left(\partial_t v_{\parallel} + \nabla \cdot (v_{\parallel}^2 \mathbf{b}) \right) = -\nabla_{\parallel} (p_i + p_e) \quad (4.35)$$

Density and velocity perturbations then travel in the parallel direction at the sound speed $c_s = \sqrt{e(T_e + T_i)/m_i}$. Sound waves do not lead to instabilities nor do they grow or damp, but they naturally arise with perturbations and interact with other wave dynamics. The associated frequency is $\omega_s = c_s k_{\parallel}$.

4.1.3.3. Shear Alfvén waves

They appear as one introduces electromagnetic induction to the parallel electric field $E_{\parallel} = -\nabla_{\parallel} \Phi - \partial_t A_{\parallel}$. The parallel magnetic vector potential in turn is known from the parallel current via Ampère's law.

$$\nabla \cdot \left[\frac{m_i n_i}{B^2} \partial_t \nabla_{\perp}^2 \Phi \right] = \nabla \cdot (j_{\parallel} \mathbf{b}) \quad (4.36)$$

$$\nabla_{\perp}^2 A_{\parallel} = -\mu_0 j_{\parallel} \quad (4.37)$$

$$\eta_{\parallel} j_{\parallel} = (-\nabla_{\parallel} \Phi - \partial_t A_{\parallel} + T_e \nabla_{\parallel} \log(n_e)) \quad (4.38)$$

$$\partial_t n_e = \frac{1}{e} \nabla \cdot (j_{\parallel} \mathbf{b}) \quad (4.39)$$

It will modify the parallel current, and introduce a new wave dynamics that travel at the Alfvén velocity $v_A = \frac{B}{\sqrt{m_i n_i \mu_0}}$. The dispersion relation for the system above is:

$$\omega_A^2 = \left(v_A^2 + \frac{T_0 k_\perp^2}{n_e \mu_0} \right) k_\parallel^2 - \frac{\eta_\parallel^2}{4\mu_0^2} \quad (4.40)$$

In the zero-resistivity limit, the dispersion relation has a single real solution. It describes shear Alfvén, travelling in parallel direction along magnetic field lines at the Alfvén velocity v_A .

4.1.3.4. Resistive ballooning modes

Magnetic curvature also plays an important role in the formation of drift waves. The effective gravity force opposes the pressure gradient, leading to inherent plasma instability and the development of resistive ballooning modes [36]. In the vorticity conservation equation, as given in Eq. 4.26, the term $\nabla \cdot \mathbf{v}_\perp$ appears. Both the electric and diamagnetic drifts take the form $(\mathbf{B} \times \nabla X)/B^2$. In a homogeneous magnetic field, as assumed above, the divergence of the drifts vanishes. However, in a curved magnetic field, this term introduces additional coupling between the vorticity and the density and potential gradients. In a realistic tokamak configuration with both poloidal and toroidal field components and a high aspect ratio R/a , poloidal perturbations can be expressed as $\tilde{X} = \sum_m \tilde{X}_m e^{im\theta}$. A perturbation mode m in the density or potential is then coupled to the modes $m-1$ and $m+1$ of the other fields.

So far we have considered several wave dynamics in the plasma individually, with each their own characteristic frequency.

———— WRITE DOWN CHARACTERISTIC VALUES ————

In reality, all these modes impact the plasma simultaneously. The actual linear behavior is far more complex and combines all frequencies.

Leddy et al. [47] compared the linear behavior of drift-reduced and full-velocity descriptions of plasmas. They found that while the drift reduction suppresses fast wave dynamics, easing timestep constraints and motivating the use of reduced MHD models as introduced in Sec. 3.3.2, the linear behavior of the two approaches only agrees within a limited parameter space, generally including tokamak conditions. However, the agreement is only robust in the edge region, with significant discrepancies appearing in the core, limiting the validity of drift-reduced models in simulation that consider both sides of the separatrix.

4.2. Electromagnetic effects in edge plasma

Numerous studies have demonstrated the electromagnetic effects on edge dynamics, both on blob dynamics in simple geometries [48, 75], and on turbulence and transport properties in real tokamak geometries [88, 89]. Their impact increases with β and can become crucial, particularly when approaching the L-H transition or in large machines like ITER operating in the high confinement mode (H-mode) [88]. In these

electromagnetic models, magnetic fluctuations are explicitly determined by Ampère's and Ohm's laws [20, 22, 28, 60, 74, 87]. Thus, electron inertia is retained, and magnetic effects occur both through magnetic induction and flutter.

Magnetic induction is captured by the time derivative of the parallel vector potential A_{\parallel} , which is principally a linear phenomenon, with the Coulomb gauge $E_{\parallel} = -\nabla_{\parallel}\Phi - \partial_t A_{\parallel}$, such that fluctuations in the electrostatic potential induce magnetic fluctuations. Magnetic flutter[10], on the other hand, refers to additional transport by magnetic fluctuations appearing through the perturbed parallel gradient such as $A_{\parallel} = (\mathbf{b} + \tilde{\mathbf{B}}/B) \cdot \nabla$ (where \mathbf{b} is the equilibrium magnetic field unit vector and $\tilde{\mathbf{B}} = \nabla \times (\tilde{A}_{\parallel} \mathbf{b})$), involving purely nonlinear phenomena. However, up to very recently, most studies did not discuss these effects [22], their implementation being motivated by improving numerical stability when using explicit time solvers [28, 74].

One particular interaction we want to study is the impact of electromagnetic effects on edge plasma turbulence. Shear Alfvén waves have already been introduced above, however they travel at much higher speeds than drift waves. In this section, we focus more on drift-Alfvén waves, which appear with the presence of a magnetic induction term in the non-adiabatic response. We then discuss the nonlinear impact of fluctuations of the magnetic equilibrium on the plasma.

4.2.1. Magnetic induction

As early as 1997, Scott[69] questioned the importance of magnetic induction for the evolution of drift waves. In the electrostatic model, whose existing implementation in Soledge3X was described in the previous chapter, the parallel current density in Ohm's law balances the plasma pressure with electric forces and resistive friction. As soon as we consider a finite β , the variation of the electromagnetic vector potential \mathbf{A} adds to the electric potential gradient in the definition of the electric field $\mathbf{E} = -\partial_t \mathbf{A} - \nabla \Phi$. At drift scales, $k_{\parallel} \ll k_{\perp}$ and only the parallel component $A_{\parallel} = \mathbf{A} \cdot \mathbf{b}$ of the electromagnetic potential effectively impacts electric forces. It is directly linked to the current density via Ampère's law:

$$\nabla \cdot \nabla A_{\parallel} = -\mu_0 j_{\parallel} \quad (4.41)$$

If we then include A_{\parallel} in the parallel electric field, magnetic induction leads to an extended, electromagnetic Ohm's law:

$$E_{\parallel} = -\nabla_{\parallel}\Phi - \partial_t A_{\parallel} \quad (4.42)$$

$$\partial_t A_{\parallel} + \eta_{\parallel} j_{\parallel} = -\nabla\Phi + \frac{1}{n_e e} \nabla p_{\parallel} + \frac{1}{n_e e} R_{\parallel} \quad (4.43)$$

Magnetic induction introduces drift Alfvén waves to the system with a velocity $v_A^2 = B^2/(m_i \mu_0 n_i)$. Because of the interplay between Ampère's (??) and Ohm's (??) laws, the magnetic induction term quickly dominates over the parallel resistivity. This occurs as soon as the perpendicular scale exceeds the collisionless skin depth, or

if $\beta > (k_{\perp} \rho_s)^2 (m_e / m_u)$ [53]. In drift-wave turbulence the characteristic scales may be much larger than the Larmor radius, in which case electromagnetic effects are dominant even at plasmas with low β values of 10^{-6} [69]. It is apparent that magnetic induction strongly impacts the response of the parallel current to the force balance and as such wave speeds in the plasma. For higher β , it essentially replaces the electric resistivity as the driver of the current response.

4.2.2. Electron inertia

Electron inertia effects are then needed to complete the resistive dissipation in Ohm's law. We introduce a transport term to Ohm's law on the parallel current:

$$\partial_t A_{\parallel} + \eta_{\parallel} j_{\parallel} + \frac{m_e}{e} (\partial_t + v_E \cdot \nabla) j_{\parallel} = -\nabla \Phi + \frac{1}{n_e e} \nabla p_{\parallel} + \frac{1}{n_e e} R_{\parallel} \quad (4.44)$$

Dudson et al.[21] further pointed out that a uniquely resistive current response does not prevent the Alfvén velocity to exceed the speed of light. It may particularly occur in the upper k_{\perp} limit. With electron inertia the parallel transport is limited the thermal electron speed and hence within physical realistic values.

The introduction of electromagnetic effects in Soledge3X in form of magnetic induction driven by the parallel electromagnetic potential A_{\parallel} , also requires a finite electron mass in Ohm's law to avoid unphysical speeds in the plasma and .

It was found on HSX that electron inertia effect might dominate resistivity for the generation of resistive ballooning modes[59].

!!!!!! introduce effective mu and beta from Scott !!!!!!!

4.2.3. Electromagnetic flutter

The magnetic field can be decomposed in equilibrium and fluctuation components:

$$\mathbf{B} = \mathbf{B}_{eq} + \tilde{\mathbf{B}} \quad (4.45)$$

The fundamental definition 2.5 of the magnetic field through its vector potential will be used. In the drift-reduced framework, we only consider the parallel projection of the magnetic vector potential $\mathbf{A} \approx A_{\parallel} \mathbf{b}$. It is then possible to calculate the fluctuating field $\tilde{\mathbf{B}}$:

$$\tilde{\mathbf{B}} = \nabla A_{\parallel} \times \mathbf{b}_{eq} + A_{\parallel} \nabla \times \mathbf{b}_{eq} \quad (4.46)$$

The second term contains the plain A_{\parallel} without its derivative, which might seem counterintuitive from the the definition of the magnetic field. It is needed to maintain \mathbf{B} divergence-free as we assume that the fluctuation is always perpendicular to the equilibrium field. The contribution of this second term to the flutter field is however negligible compared to the first.

With respect to the equilibrium field, flutter can be viewed as an additional drift acting on the plasma. Indeed, a new advection . In reality it is not an actual drift as flutter transport is in fact a deformation of the magnetic field lines and a redirection of the parallel advection.

4.3. Comparison to reduced MHD models

Introducing electromagnetic effects to the drift-reduced equations results reduces the gap to reduced MHD descriptions of plasma, presented in Sec. 3.3.2. There are however some considerable difference: Instead of the parallel current and magnetic vector potential, the MHD model retains only their toroidal component. The magnetic vector potential there is then self-similar to the poloidal flux function $A_\varphi = \Psi$.

With the knowledge of Ψ , it is much more convenient to reconstruct the exact poloidal field driven by flutter. MHD codes are directly connected to a Grad-Shafranov solver.

Drift-reduced codes are well suited for turbulence in the edge plasma and SOL regions, with an accurate modeling. With MHD codes, it is possible to analyze instabilities in the core plasma, such as tearing or kink modes, and how they lead to the formation of edge localized modes (ELMs).

4.4. Drift-Alfvén waves

In this section, we take a more formal approach to the interaction between the three new terms (magnetic induction, electron inertia and flutter) and the well-known resistive drift-wave instabilities. As they all terms appear in Ohm's law, this is the place where they will all compete and modify the non-adiabatic response of the plasma.

4.4.1. Dispersion relation

Let us consider the same system as in Sec. 4.1.3.1 and combine it with the shear Alfvén dynamics from Sec. 4.1.3.3. We then have the system:

$$\partial_t n + \mathbf{v}_E \cdot \nabla n = \frac{1}{e} \nabla \cdot (j_{\parallel} \mathbf{b}) \quad (4.47)$$

$$\frac{n m_i}{B^2} \partial_t \nabla_{\perp}^2 \Phi = \nabla \cdot (j_{\parallel} \mathbf{b}) \quad (4.48)$$

$$\left(\eta_{\parallel} + \frac{m_e}{n_e e^2} \partial_t \right) j_{\parallel} = \frac{T_e}{n} \nabla_{\parallel} n - \nabla_{\parallel} \Phi - \partial_t A_{\parallel} \quad (4.49)$$

$$\nabla_{\perp}^2 A_{\parallel} = -\mu_0 j_{\parallel} \quad (4.50)$$

Here parallel gradients and divergence use the total magnetic field \mathbf{b} . As in the previous setting the equilibrium field is purely toroidal and $\mathbf{b}_{eq} = (0, 0, 1)^T$. Again, only consider poloidal and toroidal perturbations with respective wavenumbers k_\perp and k_\parallel . If we only consider the dominating term of $\tilde{\mathbf{b}}$, any gradient $\nabla_\parallel f$ can be expressed as:

$$\begin{aligned}\mathbf{b} \cdot \nabla f &= \mathbf{b}_{eq} \cdot \nabla f + \tilde{\mathbf{b}} \cdot \nabla f \\ &= \mathbf{b}_{eq} \cdot \nabla f + \frac{1}{B} (\nabla A_\parallel \times \mathbf{b}) \cdot \nabla f \\ &= \partial_\varphi f + \frac{1}{B} [A_\parallel, f]_{\psi, \theta}\end{aligned}\quad (4.51)$$

One can see from this expression the similarity between the flutter contribution to the advection and the "ExB" advection in Eq. 4.31, reassuring us in the idea to consider flutter as a new drift. Parallel divergences can be written in the exact same way, as on a slab geometry the terms $f \partial_\psi \partial_\theta A_\parallel$ and $f \partial_\theta \partial_\psi A_\parallel$ cancel out.

$$\nabla \cdot (f \mathbf{b}) = \partial_\varphi f + \frac{1}{B} [A_\parallel, f]_{\psi, \theta} \quad (4.52)$$

From the thermodynamic force, radial density gradients are prescribed to n_0/λ_p , but $\partial_\psi \Phi$, $\partial_\psi j_\parallel$ or $\partial_\psi A_\parallel$ are assumed to zero in the linear analysis. The system of study can then be rewritten as:

$$\partial_t n - \frac{n_0}{B \lambda_p} \partial_\theta \Phi - \frac{1}{e} \partial_\varphi j_\parallel = 0 \quad (4.53)$$

$$\frac{n m_i}{B^2} \partial_t \nabla_\perp^2 \Phi - \partial_\varphi j_\parallel = 0 \quad (4.54)$$

$$\left(\eta_\parallel + \frac{m_e}{n_e e^2} \partial_t \right) j_\parallel - \frac{T_e}{n_0} \partial_\varphi n + \partial_\varphi \Phi + \left(\frac{T_e}{\partial_t - B \lambda_p} \partial_\theta \right) A_\parallel = 0 \quad (4.55)$$

$$\partial_\theta^2 A_\parallel + \mu_0 j_\parallel = 0 \quad (4.56)$$

This system can now be transformed to the Fourier space:

$$\begin{pmatrix} -i\omega & i\frac{n_0}{T_0} \omega_* & -i\frac{1}{e} k_\parallel & 0 \\ 0 & i\frac{en_0}{T_0} \rho_L^2 k_\perp^2 \omega & -ik_\parallel & 0 \\ -i\frac{T_0}{n_0} k_\parallel & ik_\parallel & \eta_\parallel - i\frac{m_e}{(n_e e^2)} \omega & i\omega_* - i\omega \\ 0 & 0 & \mu_0 & -k_\perp^2 \end{pmatrix} \begin{pmatrix} \hat{n} \\ \hat{\Phi} \\ \hat{j}_\parallel \\ \hat{A}_\parallel \end{pmatrix} = \begin{pmatrix} 0 \\ 0 \\ 0 \\ 0 \end{pmatrix} \quad (4.57)$$

To get the complex system frequencies, we need to solve the determinant of the matrix for ω . We can express the dispersion relation as a third order polynomial

equation on ω :

$$i \left(\underbrace{\rho_{L,e}^2 k_\perp^2}_{\text{finite } m_e} + \underbrace{\beta_0}_{\text{induct.}} \right) \omega^3 + \left(-i \underbrace{\beta_0 \omega_*}_{\text{flutter}} - \underbrace{\frac{\eta \| e n_0 T_0 k_\perp^2}{B^2}}_{\text{resistivity}} \right) \omega^2 - i \omega_s^2 (\omega_* - (1 + \rho_L^2 k_\perp^2) \omega) = 0 \quad (4.58)$$

with the electron Larmor radius $\rho_{L,e}^2 = m_e T_0 / (e B^2)$ and the pressure ratio $\beta_0 = e n_0 T_0 \mu_0 / B^2$. The terms arising from the different components of the electromagnetic model are clearly labeled.

4.4.2. Perturbative solution

The solution to the dispersion relation takes the form $\omega_{DAW} = \omega_0 + i\gamma$. To obtain a neat expression for the wave phase frequency ω_0 and the growth rate γ , let us assume that the drift-Alfvén frequency ω_{DAW} is close to the diamagnetic frequency, with $\delta = \omega_{DAW} - \omega_*$ such that higher orders δ^n can be ignored. To improve the readability, let us refer to the resistive term as $R = \eta \| e n_0 T_0 / B^2$. We can then express δ :

$$\delta = \frac{R k_\perp \omega_*^2 - i \rho_{L,e}^2 k_\perp^2 \omega_*^3}{i (\beta_0 - 3 \rho_{L,e}^2 k_\perp^2) \omega_*^2 - 2 R k_\perp \omega_* - i \omega_s^2} \quad (4.59)$$

If we further assume a small but still finite resistivity R (dropping higher-order terms), we can concisely express the real and imaginary parts of δ .

$$\delta \approx \frac{\rho_{L,e}^2 k_\perp^2 \omega_*^3}{(\beta_0 - 3 \rho_{L,e}^2 k_\perp^2) \omega_*^2 + \omega_s^2} + i \frac{R k_\perp \omega_*^2}{(\beta_0 - 3 \rho_{L,e}^2 k_\perp^2) \omega_*^2 + \omega_s^2} \quad (4.60)$$

At this point, a single term remains for electromagnetic induction and flutter. This is because the flutter has a stabilizing effect on the inductive term. It already appears in the dispersion relation 4.58 that the flutter term largely compensates the electromagnetic induction in the difference $i \beta_0 (\omega - \omega_*) \omega^2$. Without the flutter correction, one would get for δ :

it is interesting to discuss how the electromagnetic terms modify the characteristic drift-wave frequency ω_* known from the electrostatic setting. Since we estimated the drift-Alfvén wave by $\omega_{DAW} = \omega_* + \delta$, it is also essential to justify the assumptions made above. For that, let us compare of δ to the diamagnetic frequency.

$$\frac{\text{Re}\{\delta\}}{\omega_*} = \frac{\rho_{L,e}^2 k_\perp^2 \omega_*^2}{(\beta_0 - 3 \rho_{L,e}^2 k_\perp^2) \omega_*^2 + \omega_s^2} \quad (4.61)$$

The resistive terms do not contribute to a change of frequency.

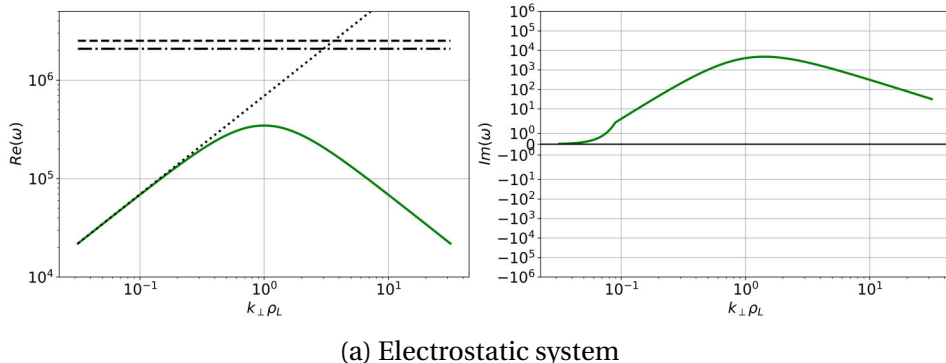
This discussion is only valid in cases where $\rho_L^2 k_\perp^2$ is small and hence ω_{DAW} is close

to the diamagnetic frequency ω_* . This is not necessarily the case everywhere in the edge, and in the next section we consider numerically the raw dispersion relation.

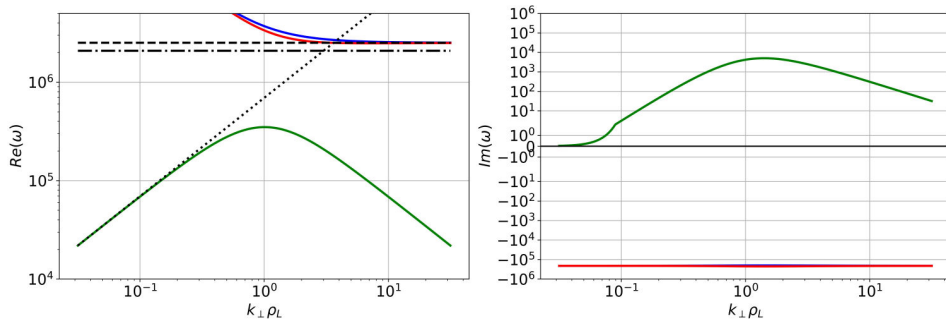
4.4.3. Electromagnetic mode excitation

The objective of this section is to analyze the impact of electromagnetic terms on drift-wave turbulence within the linearized system. Specifically, we compare the effects of a finite electron mass (EI-inert), electromagnetic induction with electron mass (EM), and electromagnetic induction with both flutter and electron mass (EM-flutter) in comparison to the baseline electrostatic case. The dispersion relation from Eq. 4.58 is adjusted to each of the four scenarios and solved exactly using the Python library SymPy for symbolic computation. Notably, we use the full dispersion relation without applying the simplifications used in the previous section's discussion.

Given the coupled nature system, there are several complex solutions for ω for each scenario, where each corresponds to a different mode. In Fig. 4.1, the real and imaginary components of all modes are plotted as functions of the perpendicular wave number k_\perp , with typical parameters for a mid-sized tokamak. The real component ω_R represents the wave phase frequency, while the imaginary component γ describes the growth or damping rate of each mode. A positive γ indicates an unstable mode with exponential growth, whereas a negative γ corresponds to a stable mode that is damped over time.



(a) Electrostatic system



(b) Electrostatic system with electron inertia

4. Drift-reduced models for plasma turbulence – 4.4. Drift-Alfvén waves

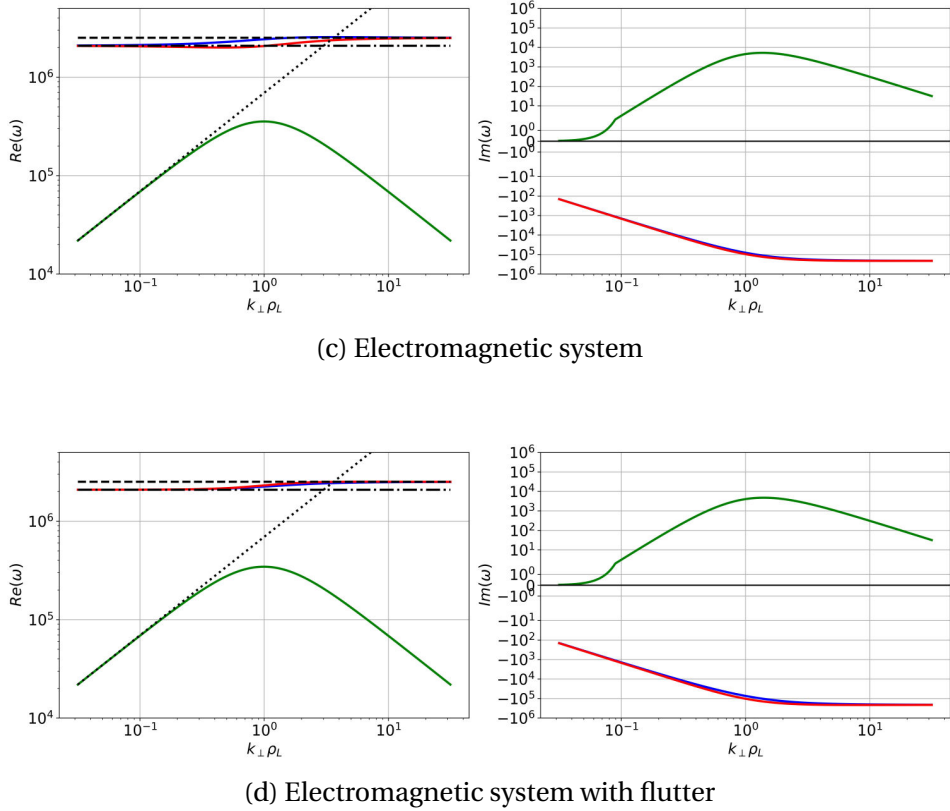


Figure 4.1.: Dependency on the perpendicular wavenumber k_{\perp} of the real and imaginary parts of the all solutions ω to the dispersion relation 4.58. Except for k_{\perp} , all other values derive from: $B = 1\text{T}$, $n = 2 \cdot 10^{19}\text{m}^{-3}$, $T = 100\text{eV}$, $\lambda_p = 0.1\text{m}$ and $k_{\parallel} = 0.6\text{m}^{-1}$. On a pair of graphs, a given color represents the same mode. In the left plots for $\text{Re}\{\omega\}$, characteristic frequencies of the system are shown for reference ("—" diamagnetic ω_* , "..." electron sound $\omega_{s,e}$, "---" Alfvén ω_A).

In the green curve, we observe the characteristic drift-wave frequency, which initially follows the diamagnetic frequency ω_* in the lower k_{\perp} limit and reaches its maximum at $k_{\perp}\rho_L = 1$, before declining again. When the electron inertia term is introduced, a new mode emerges, starting at a significantly higher frequency before stabilizing at the electron sound frequency $\omega_{s,e} = v_{th,e}k_{\parallel}$. The introduction of electromagnetic terms governs the behavior of the new modes in the lower k_{\perp} limit, which are then bounded by the shear Alfvén phase velocity. Qualitatively, the phase frequencies exhibit similar characteristics with or without flutter, with the primary difference being a more pronounced separation between the two modes as they transition from ω_A to $\omega_{s,e}$ in the pure induction. Overall, the characteristic frequencies of the electromagnetic modes are several orders of magnitude higher than the drift-wave frequency.

Looking at the growth rates associated with the modes, we first observe that drift waves are unstable with strong positive growth rates where the frequency is maximal,

4. Drift-reduced models for plasma turbulence – 4.4. Drift-Alfvén waves

consistent with the earlier discussion about drift-wave instabilities. On the other hand, electromagnetic (and electron inertial) modes are very stable, showing strong negative γ . If one intends to study the growth and propagation of turbulent structures and their global impact, Alfvénic modes will only marginally contribute. It is hence possible to avoid the numerical costs involved with the high-frequency modes without much loss of accuracy.

It is more important to consider the effects of electromagnetic contributions on the drift-wave mode. For this purpose, Fig. 4.2 compares the real and imaginary parts of the drift-wave modes in the three electromagnetic scenarios with those in the electrostatic scenario.

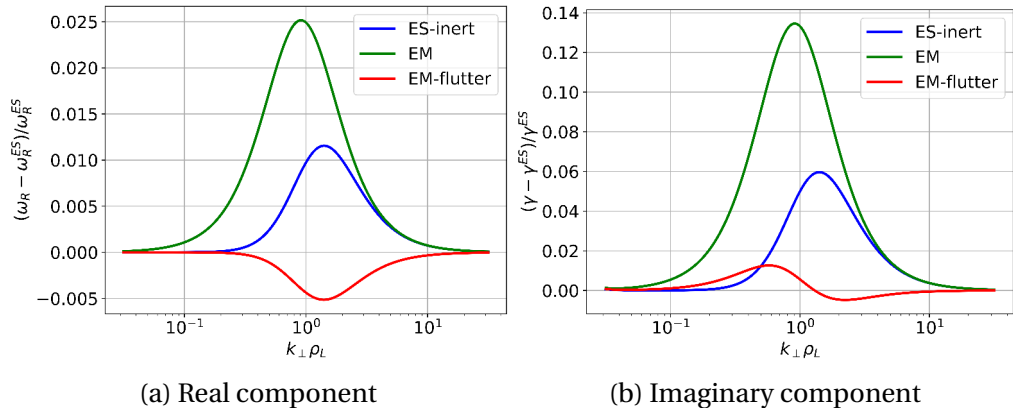


Figure 4.2.: Relative difference of drift-wave frequency in the electromagnetic scenarios to the reference electrostatic case.

The real part is altered by the electromagnetic additions, but the change of phase frequency will only have a minor impact on production cases. On the other hand, the growth rate increases with electron inertia and even more with electromagnetic induction. Electromagnetic flutter on the other largely mitigates the instabilities, and can even reduce the growth rate observed in electrostatic drift waves.

Part II.

An Electromagnetic Model for SOLEDGE3X

5. Electromagnetic effects in the SOLEDGE3X framework

In the previous chapter, we laid the foundations of drift-reduced models for edge plasma. The project SOLEDGE3X was born with the merge of the 3D turbulence code TOKAM3X[76] and the 2D transport code SolEdge2D[8]. It stands as a comprehensive multi-species 2D/3D fluid solver to investigate transport and turbulence at the plasma edge up to the first wall, with a particular focus on modeling plasma-wall interactions. This has allowed successful investigations of numerous facets of edge plasma dynamics, such as turbulence[7] impurity transport[11] or ITER first-wall fluxes[62]. Until now, however, the model has been limited to electrostatic turbulence, with only fluctuations in the electric potential, determined by the non-adiabatic response to density fluctuations, being taken into account.

By the end of this chapter, we will have formulated a set of self-consistent transport equations that include electromagnetic effects. The existing SOLEDGE3X framework is extended to accomodate a finite electron mass in Ohm's law, an inductive term in the parallel electric field and flutter perturbations of the magnetic equilibrium. This requires the addition of two new fields: the parallel current density j_{\parallel} and the parallel magnetic vector potential A_{\parallel} .

In the first section 5.1, we introduce reference values for all quantities against which all variables are normalized, including the new electromagnetic fields. Then, section 5.2 recaps the density, momentum, energy and charge conservation equations and their exact formulation in SOLEDGE3X. The entire section 5.3 is dedicated to the electromagnetic model and its formulation within the charge balance equation. Finally, section 5.4 describes boundary conditions imposed at the sheath, the core and the first wall.

5.1. Dimensionless fields

To simplify the equations and improve the numerical stability, the code solves the equation for dimensionless physical quantities. It means that each variable X is scaled by a factor X_0 to obtain a dimensionless $\hat{X} = X/X_0$, where X_0 is representative for the range of values of X . Therefore, all quantities \hat{X} have similar values and we can prevent some numerical issues that might occur in equations containing variables with strongly different orders of magnitude.

The reference density n_0 , temperature T_0 and magnetic field B_0 are free parameters that must be specified by the user to best match the conditions of the simulated scenario. Masses are expressed as factors of the atomic unit mass m_u and the Coulomb logarithm for particle collisions is set to $\Lambda = 15$. In the sheath-dominated SOL, the electric potential Φ is proportional to the temperature with $\Phi_{se} = \ln(\sqrt{m_i/(2\pi m_e)}) T \approx 3T$. The potential is hence of the same order of magnitude as the temperature and it is convenient to set $\Phi_0 = T_0$. In this context, it is important to remember that temperatures are always expressed as energies in units of electronvolts [eV]. From the set of free parameters, we can derive spatial and temporal reference values to match the cyclotronic time τ_0 and the Larmor radius ρ_0 :

$$\tau_0 = \frac{m_u}{eB_0} \quad (5.1)$$

$$\rho_0^2 = \frac{T_0 m_u}{e B_0^2} \quad (5.2)$$

$$\rho_0 = c_0 \tau_0 \quad \text{with the reference thermal ion speed } c_0 = \sqrt{\frac{e T_0}{m_u}} \quad (5.3)$$

In addition, dimensionless versions of the Spitzer-Härm viscosity $\nu_{\parallel,\alpha}$, conductivity $\kappa_{\parallel,\alpha}$ and resistivity η_{\parallel} may be defined:

$$\nu_{\parallel,\alpha}^0 = \frac{\tau_0}{n_0 \rho_0^2 m_u} T_0^{2.5} \quad \kappa_{\parallel,\alpha}^0 = \frac{\tau_0}{e n_0 \rho_0^2} T_0^{2.5} \quad \eta_{\parallel}^0 = \frac{e n_0}{B_0} T_0^{-1.5} \quad (5.4)$$

As for all other physical quantities, the newly introduced fields A_{\parallel} and j_{\parallel} are replaced by dimensionless quantities in the code. First of all we need to define two constants A_{\parallel}^0 and j_{\parallel}^0 so that the dimensionless quantities \hat{A}_{\parallel} and \hat{j}_{\parallel} have about the same magnitude as the existing fields:

$$\hat{j}_{\parallel} = j_{\parallel} / j_{\parallel}^0 \quad \hat{A}_{\parallel} = A_{\parallel} / A_{\parallel}^0 \quad (5.5)$$

As the main occurrence of j_{\parallel} is in the vorticity conservation equation 4.26, it is wise to normalize j_{\parallel} to it. An expression for j_{\parallel}^0 can be derived:

$$\begin{aligned} & \hat{\nabla} \cdot \left[\frac{m_u n_0 \Phi_0}{\tau_0 B_0^2 \rho_0^2} \frac{\hat{m}_\alpha \hat{n}_\alpha}{\hat{B}^2} \hat{\partial}_t \hat{\nabla}_\perp \hat{\Phi} \right] \sim \hat{\nabla} \cdot \left[\frac{j_{\parallel}^0}{\rho_0} \hat{j}_{\parallel} \mathbf{b} \right] \\ \Rightarrow \quad & j_{\parallel}^0 = \frac{m_u n_0 \Phi_0}{\tau_0 B_0^2 \rho_0} = e n_0 c_0 \end{aligned} \quad (5.6)$$

This reference value is coherent with the definition of the parallel current density as the difference of electron and ion momentum balances.

To define A_{\parallel}^0 , there are essentially two different possible choices: the first option originates in Ampère's law 4.41 and compels $A_{\parallel}^{0(1)}$ to depend on the magnetic permeability μ_0 and the reference parallel current j_{\parallel}^0 .

$$\frac{A_{\parallel}^{0(1)}}{\rho_0^2} = \mu_0 j_{\parallel}^0 \quad \Leftrightarrow \quad A_{\parallel}^{0(1)} = \mu_0 e n_0 c_0 \rho_0^2 \quad (5.7)$$

The second option relies on the revised definition of the parallel electric field in Eq. 4.42 and states that $\partial_t A_{\parallel}$ is homogeneous to $\nabla \Phi$. This yields:

$$\frac{A_{\parallel}^{0(2)}}{\tau_0} = \frac{\Phi_0}{\rho_0} \quad \Leftrightarrow \quad A_{\parallel}^{0(2)} = \frac{\Phi_0 \tau_0}{\rho_0} \quad (5.8)$$

Both variants are valid, and they differ by a factor:

$$\frac{A_{\parallel}^{0(1)}}{A_{\parallel}^{0(2)}} = \beta_0 \quad (5.9)$$

where the reference plasma parameter β_0 is the ratio between reference plasma and magnetic pressures:

$$\beta_0 = \frac{e n_0 T_0}{B_0^2 / \mu_0} \quad (5.10)$$

$A_{\parallel}^{0(1)}$ and $A_{\parallel}^{0(2)}$ are about four orders of magnitude away in the edge. From a numerical point of view, we need both relations, so an occurrence of the parameter β_0 is inevitable in the dimensionless formulation of the system. The first option, based on Ampère's law, is chosen for the implementation. In the continuation of this chapter, all relations are expressed with the dimensionless fields.

5.2. Transport equations

For simulations of the SOL in SOLEDGE3X, the three fluid moments in Eqs. 3.10, 3.14 and 3.17 are used for the ion density and momentum conservation, electron and ion energy conservation, and vorticity conservation equations. In the drift-reduced formulation, to compute the different drifts that compose the velocity \mathbf{u} , it is convenient to decompose it into a parallel component u_{\parallel} along the magnetic field lines \mathbf{b} and orthogonal \mathbf{u}_{\perp} components. This relationship is given by:

$$\mathbf{u} = u_{\parallel} \mathbf{b} + \mathbf{u}_{\perp} \quad \text{with} \quad u_{\parallel} = \mathbf{u} \cdot \mathbf{b} \quad \text{and} \quad \mathbf{u}_{\perp} = \mathbf{b} \times \mathbf{u} \quad (5.11)$$

This decomposition also applies to any other vector field. The perpendicular velocity is calculated with the plasma drifts in Eq. 4.17. Similarly, we define parallel and perpendicular gradient operators as follows:

$$\nabla_{\parallel} = \mathbf{b} \cdot \nabla \quad \nabla_{\perp} = \nabla - \nabla_{\parallel} \quad (5.12)$$

Anomalous perpendicular diffusion is included in all conservation equations via a term \mathfrak{D}_X^{α} :

$$\mathfrak{D}_X^{\alpha} = \nabla \cdot (D \nabla_{\perp} X_{\alpha}) \quad (5.13)$$

Its usage is twofold: for transport simulations, it accounts for the total cross-field transport with a correspondingly larger diffusion coefficient D , such that perpendicular drift velocities are not required. In turbulent simulations with self-consistent drifts, D is much smaller but remains finite to capture phenomena at scales below the mesh resolution and to improve numerical stability. A typical value for the diffusion coefficient is $D = 10^{-2} \text{ m}^2/\text{s}$.

In general, the code is capable of handling multiple species, with the index i referring to any of the ion species. Further, the index e denotes electrons, and α variables that apply to both electrons and ions. We can now formulate the balance equations that constitute the SOLEDGE3X model.

5.2.1. Mass balance

The mass conservation equation for ions is straight-forward:

$$\partial_t n_i + \nabla \cdot (n_i \mathbf{u}) = S_{n,i} - \mathfrak{D}_n^i \quad (5.14)$$

The ion source term $S_{n,i}$ in the mass balance comes from imposed external sources or from recombination and ionization processes after particle collisions with neutrals.

It is sufficient to solve the mass balance for ions, as the fluid density of electrons can be easily retrieved with the quasi-neutrality assumption:

$$n_e = \sum_i Z_i n_i \quad (5.15)$$

5.2.2. Momentum balance

In the drift-reduced approach, the momentum conservation equation is primarily solved in parallel direction on $\gamma_i = n_i u_{\parallel,i}$.

$$m_i \partial_t \gamma_i + m_i \nabla \cdot (\gamma_{\parallel,i} \mathbf{u}) = +Z_i n_i E_{\parallel} - \nabla_{\parallel} p_i - \mathbf{b} \cdot \nabla \cdot \boldsymbol{\Pi}_i + S_{\gamma,i} + R_{\parallel,i} - \mathfrak{D}_{\gamma}^i \quad (5.16)$$

The source term $S_{\gamma,i}$ is again due to ionization, recombination and radiation processes. Collisions between particles lead to the parallel friction term $R_{\parallel,i}$, which is known from Braginskii's and Zhdanov's closures. The parallel projection of the stress tensor Π_i can be expressed as[3, 38, 86]:

$$\mathbf{b} \cdot \nabla \cdot \boldsymbol{\Pi}_i = \frac{2}{3} \nabla \parallel \pi_{\parallel} + \pi_{\parallel} \nabla \cdot \mathbf{b} \quad \text{with: } \pi_{\parallel} = 3\nu_{\parallel} \left(\nabla_{\parallel} u_{\parallel,i} - \boldsymbol{\kappa} \cdot \mathbf{u}_{\perp,i} - \frac{1}{3} \nabla \cdot \mathbf{u} \right) \quad (5.17)$$

including the curvature of the magnetic field $\kappa = \mathbf{b} \cdot \nabla \mathbf{b}$. In the most simple model, the electron velocity is calculated under full ambipolarity assumption:

$$\gamma_{\parallel,e} = \sum_i Z_i \gamma_i \quad (5.18)$$

with more accurate models currently under development.

5.2.3. Energy balance

The energy conservation equation is solved for both electrons and ions. As already described in Sec. 3.2.3, the total energy is the sum of thermal and kinetic energy:

$$\varepsilon_{\alpha} = \frac{3}{2} n_{\alpha} T_{\alpha} + \frac{1}{2} m_{\alpha} n_{\alpha} u_{\alpha}^2 \quad (5.19)$$

where the kinetic contribution is negligible for electrons. The transport equation for energy is then:

$$\partial_t \varepsilon_{\alpha} + \nabla \cdot ((\varepsilon_{\alpha} + p_{\alpha}) \mathbf{u}_{\alpha} + \boldsymbol{\Pi}_i \cdot \mathbf{u}_{\alpha} + q_{\alpha}) = \mathbf{u}_{\alpha} \cdot (Z_{\alpha} n_{\alpha} \mathbf{E}_{\alpha} + \mathbf{R}_{\alpha}) + Q_{\alpha} + S_{\varepsilon,\alpha} - \mathfrak{D}_{\varepsilon}^{\alpha} \quad (5.20)$$

For q_{α} , we currently only consider the parallel heat flux $q_{\parallel,\alpha} = \kappa_{\parallel,\alpha} \nabla T_{\alpha}$ from the Spiter-Härm model. Additional heat fluxes Q_{α} and sources $S_{\varepsilon,\alpha}$ arise from the fluid closure.

5.2.4. Charge balance

To complete the system, a last equation on the charge balance is needed. This approach is equivalent to the vorticity conservation equation from Eq. 4.26. Because of the quasineutrality assumption the volume charge ρ is assumed to be 0 and charge conservation is ensured if the total current divergence is 0.

$$\nabla \cdot \mathbf{j} = 0 \quad (5.21)$$

The total current is due to charge transport by plasma species. It is hence calculated as:

$$\mathbf{j} = \sum_{\alpha} Z_{\alpha} n_{\alpha} \mathbf{u}_{\alpha} \quad (5.22)$$

As the current is directly linked to the plasma species transport, it is decomposed into the same terms as the velocities in equations 4.20 and 4.21. The "E cross B" drift is the same for all species therefore its contribution to the current vanishes with the quasineutrality assumption.

jDia jPi jPolarS

Neglecting curvature terms, we can derive an expression for the perpendicular polarization current from [Equation 4.24](#).

$$\mathbf{j}_p = -\partial_t \boldsymbol{\omega}_s - \sum_i Z_i \nabla \cdot (\mathbf{u}_i^{(0)} \otimes \boldsymbol{\omega}_i) \quad (5.23)$$

$$\text{with: } \boldsymbol{\omega}_s = \sum_i Z_i \boldsymbol{\omega}_i$$

Only the zero-th order drift velocities from Eq. 4.20 contribute to the polarization current. The problem is not solved on \mathbf{j} itself but on the vorticity defined as $\Omega = \nabla \cdot \boldsymbol{\omega}_s$ which gives the expression on \mathbf{j}_p :

$$\nabla \cdot \mathbf{j}_p = -\partial_t \Omega + \nabla \cdot \sum_i Z_i \nabla \cdot (\mathbf{u}_i^{(0)} \otimes \boldsymbol{\omega}_i) = -\partial_t \Omega \quad (5.24)$$

The divergence of the total current can then be transformed into a transport equation on the vorticity:

$$\begin{aligned} & \nabla \cdot \mathbf{j} = 0 \\ \Leftrightarrow & -\nabla \cdot \mathbf{j}_p = \nabla \cdot (j_{\parallel} \mathbf{b} + \mathbf{j}^* + \mathbf{j}_{\perp,\Pi} + \mathbf{j}_{\pi}) \\ \Leftrightarrow & \partial_t \Omega = \nabla \cdot \sum_i Z_i \nabla \cdot (\mathbf{u}_i^{(0)} \otimes \boldsymbol{\omega}_i) + \nabla \cdot (j_{\parallel} \mathbf{b} + \mathbf{j}^* + \mathbf{j}_{\perp,\Pi} + \mathbf{j}_{\pi}) \end{aligned} \quad (5.25)$$

If this equation is combined with [Equation 4.24](#) we get :

$$\begin{aligned} & \boldsymbol{\omega}_i = \frac{m_i}{Z_i B^2} \left(n_i \nabla_{\perp} \Phi + \frac{1}{Z_i} \nabla_{\perp} \left(p_i - \frac{\pi_{\parallel,i}}{3} \right) \right) - \frac{m_i}{Z_i^2 B^2} \mathbf{S}_{u_{\perp,i}} \\ \Leftrightarrow & \sum_i Z_i \boldsymbol{\omega}_i = \sum_i Z_i \left[\frac{m_i}{Z_i B^2} \left(n_i \nabla_{\perp} \Phi + \frac{1}{Z_i} \nabla_{\perp} \left(p_i - \frac{\pi_{\parallel,i}}{3} \right) \right) - \frac{m_i}{Z_i^2 B^2} \mathbf{S}_{u_{\perp,i}} \right] \\ \Leftrightarrow & \Omega = \nabla \cdot \sum_i \left[\frac{m_i}{B^2} \left(n_i \nabla_{\perp} \Phi + \nabla_{\perp} \left(p_i - \frac{\pi_{\parallel,i}}{3} \right) \right) - \frac{m_i}{Z_i B^2} \mathbf{S}_{u_{\perp,i}} \right] \\ \Leftrightarrow & \partial_t \Omega = \nabla \cdot \left[\frac{m_i n_i}{B^2} \partial_t \nabla_{\perp} \Phi \right] + \partial_t \Omega_{\pi} - \mathcal{D}_{\Omega} \\ \Leftrightarrow & \nabla \cdot \left[\frac{m_i n_i}{B^2} \partial_t \nabla_{\perp} \Phi \right] = \nabla \cdot (j_{\parallel} \mathbf{b} + \mathbf{j}^* + \mathbf{j}_{\perp,\Pi} + \mathbf{j}_{\pi}) - \partial_t \Omega_{\pi} - \mathcal{D}_{\Omega} \end{aligned} \quad (5.26)$$

In this calculation we used the Boussinesq approximation and the Einstein summation convention.

tion over the ion index i allows for a more compact expression. Since we express a conservation on the vorticity Ω , we also introduced an anomalous diffusion term \mathfrak{D}_Ω . All pressure terms are regrouped in Ω_π :

$$\Omega_\pi = \nabla \cdot \sum_i \left(\frac{m_i}{Z_i B^2} \nabla_\perp [n_i T_i] \right) \quad (5.27)$$

The parallel current density is calculated from the generalized Ohm's law neglecting the electron mass (for now) and using Spitzer-Härm resistivity η_\parallel :

$$j_\parallel = \sigma_\parallel \left(E_\parallel + \frac{\nabla_\parallel p_e}{n_e} + 0.71 \nabla_\parallel T_e \right) \quad \text{with:} \quad \sigma_\parallel = 1/\eta_\parallel \quad (5.28)$$

For now, we assume a static magnetic field and define the parallel electric field as the negative gradient of the electrostatic potential in parallel direction $E_\parallel = -\nabla_\parallel \Phi$. With the electron pressure $p_e = n_e T_e$, we get:

$$\frac{1}{n_e} \nabla_\parallel p_e = T_e \nabla_\parallel \log(n_e) + \nabla_\parallel T_e$$

If we now inject Equation 5.28 into the vorticity equation Equation 5.26, we obtain:

$$\nabla \cdot \left[\frac{m_i n_i}{B^2} \partial_t \nabla_\perp \Phi \right] = \nabla \cdot \sigma_\parallel \left[-\nabla_\parallel \Phi + T_e \nabla_\parallel \log(n_e) + 1.71 \nabla_\parallel T_e \right] \mathbf{b} + F_\Omega \quad (5.29)$$

where $F_\Omega = (\mathbf{j}^* + \mathbf{j}_\Pi + \mathbf{j}_\pi) - \partial_t \Omega_\pi - \mathfrak{D}_\Omega$ regroups the remaining terms.

The vorticity equation gives a relation for the electric potential Φ , required to calculate "ExB" drifts and therefore essential to simulate plasma turbulence. Because of the low resistivity η_\parallel , this problem is actually numerically hard to solve. Explicit approaches are then strongly constrained by a timestep size of the order of the collision time. Implicit approaches have to handle a numerically difficult problem, with two Laplacian operators, one perpendicular and one parallel, with a high anisotropy because of the unfavorable ratio $\sigma_\parallel B^2 / m_i n_i$ between the respective diffusion coefficients. The hardness to solve the system is a major obstacle for turbulent simulations on larger tokamaks because of prohibitive solve times of iterative solvers. Hotter scenarios, as they would occur in fusion-relevant devices, pose an additional problem as $\eta_\parallel \propto T_e^{-1.5}$, resulting in an even poorer numerical condition of the problem.

5.3. Electromagnetic Model in SOLEDGE3X

Until now we have expressed the SOLEDGE3X transport equations as they are used in the existing electrostatic version of the code. It lays the framework on which we are now going to build the electromagnetic model. As demonstrated in the previous Sec. 4.2, it consists of three key elements: electron inertia, magnetic induction and flutter. In this section, each of the ingredients will be introduced separately, to clearly identify the impact of each on the vorticity equation.

5.3.1. Electron Inertia

The first element to the electromagnetic model is the electron inertia term in the generalized Ohm's law. To properly derive this term, we start with the parallel momentum conservation equations for electrons 5.30 and ions 5.31.

$$m_e \partial_t \gamma_e + m_e \nabla \cdot (\gamma_{\parallel,e} \mathbf{u}_e) = -n_e E_{\parallel} - \nabla_{\parallel} p_e - \mathbf{b} \cdot \nabla \cdot \boldsymbol{\Pi}_e + S_{\gamma,e} + R_{\parallel,e} - m_e \mathfrak{D}_{\gamma}^e \quad (5.30)$$

$$m_i \partial_t \gamma_i + m_i \nabla \cdot (\gamma_{\parallel,i} \mathbf{u}_i) = +Z_i n_i E_{\parallel} - \nabla_{\parallel} p_i - \mathbf{b} \cdot \nabla \cdot \boldsymbol{\Pi}_i + S_{\gamma,i} + R_{\parallel,i} - m_i \mathfrak{D}_{\gamma}^i \quad (5.31)$$

Next we multiply the equation for the electrons by $-1/m_e$ and the equation for ions Z_i/m_i . If we then take the sum over all species (electrons and all ions), we get a conservation equation for the parallel current density $j_{\parallel} = \sum_{\alpha} Z_{\alpha} \gamma_{\parallel,\alpha}$ (defining $Z_e = -1$).

$$\begin{aligned} \frac{m_e}{n_e} \partial_t j_{\parallel} + \frac{m_e}{n_e} \nabla \cdot (Z_i \gamma_{\parallel,i} \mathbf{u}_i - \gamma_{\parallel,e} \mathbf{u}_e) &= \left(1 + \frac{m_e}{m_i} \frac{Z_i^2 n_i}{n_e}\right) E_{\parallel} + \frac{1}{n_e} \nabla_{\parallel} p_e - \frac{m_e}{m_i} \frac{Z_i}{n_e} \nabla_{\parallel} p_i \\ &\quad + \frac{1}{n_e} \mathbf{b} \cdot \nabla \cdot \boldsymbol{\Pi}_e - \frac{m_e}{m_i} \frac{Z_i}{n_e} \mathbf{b} \cdot \nabla \cdot \boldsymbol{\Pi}_i - \frac{1}{n_e} S_{\gamma,e} + \frac{m_e}{m_i} \frac{Z_i}{n_e} S_{\gamma,i} \\ &\quad + \frac{1}{n_e} R_{\parallel,e} + \frac{m_e}{m_i} \frac{Z_i}{n_e} R_{\parallel,i} + \frac{m_e}{n_e} \mathfrak{D}_{\gamma}^e - \frac{m_e Z_i}{n_e} \mathfrak{D}_{\gamma}^i \end{aligned} \quad (5.32)$$

Here the sum over ion species is not written explicitly, but every term involving the index i should be seen as a sum over all ions. Braginskii's closure provides a neat expression for the electron friction terms $R_{\parallel,\alpha}$. It involves an Ohmic term, caused by collisions between charged particles that dissipate the current, and a thermoelectric force, where a temperature gradient can create currents.

$$R_{\parallel,e} = n_e [0.71 \nabla_{\parallel} T_e - \eta_{\parallel} j_{\parallel}] \quad (5.33)$$

If we neglect all terms involving the electron mass, we exactly recover the electrostatic Ohm law from Eq. 5.28. The aim of this section is to consider a finite m_e , so we keep all terms. To truly obtain a transport equation on the current, we need to reformulate the advection term. There is no effective advection velocity for j_{\parallel} readily available and the poor ambipolar definition of $\gamma_{\parallel,e}$ is of little help here. We can instead develop this term to obtain a formulation where j_{\parallel} is advected by the electron velocity:

$$\nabla \cdot \left(\sum_i Z_i \gamma_{\parallel,i} \mathbf{u}_i - \gamma_{\parallel,e} \mathbf{u}_e \right) = \nabla \cdot \left(\sum_i Z_i \gamma_{\parallel,i} (\mathbf{u}_i - \mathbf{u}_e) - j_{\parallel} \mathbf{u}_e \right) \quad (5.34)$$

If we now rewrite Eq. 5.32 with the considerations above, we get:

$$\frac{m_e}{n_e} \partial_t j_{\parallel} + \frac{m_e}{n_e} \nabla \cdot (j_{\parallel} \mathbf{u}_e) - \frac{m_e}{n_e} \nabla \cdot \left(\sum_i Z_i \gamma_i \mathbf{u}_e \right) = E_{\parallel} + \frac{\nabla_{\parallel} p_e}{n_e} + 0.71 \nabla_{\parallel} T_e - \eta_{\parallel} j_{\parallel} + \sum_i Z_i \partial_t \gamma_i - \frac{m_e}{n_e} \mathfrak{D}_j^e \quad (5.35)$$

With this transport equation on the parallel current, the anomalous diffusion is also calculated with j_{\parallel} . The term $\sum_i Z_i \partial_t \gamma_i$ contains all other terms in Eq. 5.32, but they do not need to be explicated in the implementation as they are already known from the ion momentum conservation equations. Numerical experiments have proven the necessity to carefully treat all the terms, especially the advection of j_{\parallel} , to avoid numerical instabilities.

If we now combine Ohm's with electron inertia with the electrostatic vorticity equation 5.29, we obtain following system:

$$\begin{cases} \nabla \cdot \left[\frac{m_i n_i}{B^2} \partial_t \nabla_{\perp} \Phi \right] - \nabla \cdot [j_{\parallel} \mathbf{b}] = F_{\Omega} \\ j_{\parallel} + \frac{\sigma_{\parallel} m_e}{n_e} [\partial_t j_{\parallel} + \nabla \cdot (j_{\parallel} \mathbf{u}_e)] = \sigma_{\parallel} (-\nabla_{\parallel} \Phi + T_e \nabla_{\parallel} \log n_e + 1.71 \nabla_{\parallel} T_e) \\ \quad + \frac{\sigma_{\parallel} m_e}{n_e} \left[\sum_i Z_i [\nabla \cdot (\gamma_i \mathbf{u}_e) + \partial_t \gamma_i] - \mathfrak{D}_j^e \right] \end{cases} \quad (5.36)$$

For better readability let us express the system in matrix form, where \circ shall be replaced by the corresponding field within operators and all advection terms in j_{\parallel} and γ_i are regrouped in the term \mathcal{A}_j .

$$\begin{pmatrix} \nabla \cdot \left[\frac{m_i n_i}{B^2} \partial_t \nabla_{\perp} \circ \right] & -\nabla \cdot [\circ \mathbf{b}] \\ \sigma_{\parallel} \nabla_{\parallel} \circ & 1 + \frac{\sigma_{\parallel} m_e}{n_e} \partial_t \circ \\ 0 & 1 \end{pmatrix} \begin{pmatrix} \Phi \\ j_{\parallel} \\ \mathcal{A}_j \end{pmatrix} = \begin{pmatrix} F_{\Omega} \\ \sigma_{\parallel} \left(T_e \nabla_{\parallel} \log n_e + 1.71 \nabla_{\parallel} T_e - \frac{m_e}{n_e} \mathfrak{D}_j^e \right) + \mathcal{A}_j \end{pmatrix} \quad (5.37)$$

5.3.2. Electromagnetic Induction

Magnetic induction is added to the system with the term $\partial_t A_{\parallel}$ to the definition of the parallel electric field. It appears in the generalized Ohm's law for the parallel current 5.28, which in turn is member of the vorticity equation 5.25.

$$E_{\parallel} = -\nabla_{\parallel} \Phi - \beta_0 (\partial_t A_{\parallel} + \mathfrak{D}_A) \quad (5.38)$$

The parallel magnetic vector potential A_{\parallel} was never calculated before and needs to be introduced to the system. In Ampère's law under the Coulomb gauge, j_{\parallel} is equal to the perpendicular diffusion of A_{\parallel} :

$$\nabla \cdot \nabla_{\perp} A_{\parallel} = -j_{\parallel} \quad (5.39)$$

As we evolve the magnetic potential together with the electric potential gradient, we also introduce an anomalous diffusion on A_{\parallel} by the term \mathfrak{D}_A . It does not have any physical meaning and primarily serves to numerically stabilize the system from sub-mesh instabilities. The electric potential Φ is thus implicitly linked to j_{\parallel} and A_{\parallel} and all three unknowns need to be solved in one common system. To summarize, the new set of equations reads:

$$\begin{cases} \nabla \cdot \left[\frac{m_i n_i}{B^2} \partial_t \nabla_{\perp} \Phi \right] - \nabla \cdot [j_{\parallel} \mathbf{b}] &= F_{\Omega} \\ j_{\parallel} &= \sigma_{\parallel} (-\nabla_{\parallel} \Phi - \beta_0 \partial_t A_{\parallel} - \beta_0 \mathfrak{D}_A + T_e \nabla_{\parallel} \log n_e + 1.71 \nabla_{\parallel} T_e) \\ \nabla \cdot \nabla_{\perp} A_{\parallel} &= -j_{\parallel} \end{cases} \quad (5.40)$$

It can also be compactly expressed in matrix form:

$$\begin{pmatrix} \nabla \cdot \left[\frac{m_i n_i}{B^2} \partial_t \nabla_{\perp} \circ \right] & -\nabla \cdot [\circ \mathbf{b}] & 0 \\ \sigma_{\parallel} \nabla_{\parallel} \circ & 1 \circ & \sigma_{\parallel} \beta_0 \partial_t \circ \\ 0 & 1 & \nabla \cdot [\nabla_{\perp} \circ] \end{pmatrix} \begin{pmatrix} \Phi \\ j_{\parallel} \\ A_{\parallel} \end{pmatrix} = \begin{pmatrix} F_{\Omega} \\ \sigma_{\parallel} (T_e \nabla_{\parallel} \log n_e + 1.71 \nabla_{\parallel} T_e - \beta_0 \mathfrak{D}_A) \\ 0 \end{pmatrix} \quad (5.41)$$

These equations use Ohm's law without the electron inertia term previously introduced in [subsection 5.3.1](#). It is obviously possible (and even necessary) to include the temporal j_{\parallel} in the electromagnetic equations and it is recommended to do so. To allow for maximal flexibility, any combination of Φ with A_{\parallel} and/or j_{\parallel} can be used and we will discuss each of these combinations in later chapters.

5.3.3. Electromagnetic Flutter

Due to the strong anisotropy in tokamaks, most edge turbulence codes rely on alignment to the magnetic equilibrium (see discussion in Ref.[68]). However, in the electromagnetic model, small perturbations of \mathbf{B}_{eq} can exist and are driven by fluctuations of A_{\parallel} such as $\tilde{\mathbf{B}} = \nabla \times (\tilde{A}_{\parallel} \mathbf{b})$. Therefore, these fluctuations of A_{\parallel} have to be estimated and A_{\parallel} cannot be used directly. Indeed, the diamagnetic current induced by the evolution of the full plasma pressure is balanced by a stationary background parallel current, the Pfirsch-Schlüter current, which induces a stationary part of significant amplitude in A_{\parallel} through Ampere's law (Eq. 5.39). This latter is denoted $A_{\parallel,0}$, and corresponds to the Grad-Shafranov shift due to Pfirsch-Schlüter currents that are accounted for in the parallel current. This shift $A_{\parallel,0}$ is obviously accounted for in B_{eq} , and therefore it has to be subtracted from A_{\parallel} in nonlinear parallel operators. This is done in this work by simply removing the toroidal average as proposed by Ref.[28] in the GBS code:

$$\tilde{A}_{\parallel} = A_{\parallel} - \langle A_{\parallel} \rangle_{\varphi} \quad (5.42)$$

Therefore, the flutter is computed as follows:

$$\nabla \times (\mathbf{A}_{\parallel,0} + \tilde{A}_{\parallel} \mathbf{b}_{eq}) = \mathbf{B}_{eq} + \tilde{\mathbf{B}} \quad (5.43)$$

This leads to:

$$\tilde{\mathbf{b}} = \beta_0 \left(-\frac{\mathbf{b}_{eq} \times \nabla \tilde{A}_{\parallel}}{\|\mathbf{B}\|} + \frac{\tilde{A}_{\parallel} \nabla \times \mathbf{b}_{eq}}{\|\mathbf{B}\|} \right) \quad (5.44)$$

The gradient $\nabla \tilde{A}_{\parallel}$ scales with the characteristic turbulent length $1/L_{\perp}$ and the curl $\nabla \times \mathbf{b}$ with the machine dimension $1/a$. Therefore, $\frac{\mathbf{b}_{eq} \times \nabla \tilde{A}_{\parallel}}{\|\mathbf{B}\|}$ is the main contributor to the flutter field.

Note that Hager et al. [33] have suggested an additional time-averaged $\langle A_{\parallel} \rangle_{\varphi,t}$ to evaluate fluctuations in the parallel electromagnetic potential, arguing that turbulent structures might appear at the same position on all poloidal planes and should therefore not be removed in the flutter calculation. This approach has been used in recent work in the GRILLIX code [87], but was not adopted in the present work, as it was estimated that the gain in accuracy did not compensate for the additional computation and memory costs.

The perturbed magnetic unit field $\tilde{\mathbf{b}}$ is calculated at the beginning of each timestep and added to the equilibrium unit vector \mathbf{b}_{eq} . The complete vector $\mathbf{b} = \mathbf{b}_{eq} + \tilde{\mathbf{b}}$ is then used in all parallel advection, gradient, and diffusion terms. Since we base our calculations on plasma fields from the previous timestep, this perturbation can be seen as an additional first-order drift in the equations. The expression in the framework of the conservation equations does not change with flutter, but the underlying definition of parallel gradients and divergence surely increases in complexity.

Notwithstanding the smallness of the flutter field, it is important to maintain the total magnetic field divergence-free. Let us verify this property with our definition of the flutter field:

$$\begin{aligned} \nabla \cdot \mathbf{B} &= \nabla \cdot B \mathbf{b}_{eq} + \nabla \cdot B \tilde{\mathbf{b}} \\ &= -\beta_0 \mathbf{b}_{eq} \times \nabla \tilde{A}_{\parallel} + \beta_0 \tilde{A}_{\parallel} \nabla \times \mathbf{b}_{eq} \\ &= \beta_0 \left[-(\nabla \times \mathbf{b}_{eq}) \cdot \nabla A_{\parallel} + \mathbf{b}_{eq} \cdot (\nabla \times \nabla A_{\parallel}) + A_{\parallel} \nabla \cdot (\nabla \times \mathbf{b}_{eq}) + \nabla A_{\parallel} \cdot (\nabla \times \mathbf{b}_{eq}) \right] \\ &= 0 \end{aligned} \quad (5.45)$$

The equilibrium field is externally provided such that it is divergence free, so $\nabla \cdot B \mathbf{b}_{eq} = 0$. We further used the vector calculus identities on second-order derivatives $\nabla \times \nabla X = 0$ and $\nabla \cdot (\nabla \times \mathbf{X})$. It further proves the importance of the second (small)

term in the definition of $\tilde{\mathbf{b}}$ (with $\nabla \times \mathbf{b}_{eq}$), as without it, the flutter field would not be divergence-free.

5.3.4. Formulation of the electromagnetic vorticity system

One open question remains on how to formulate the parallel current in the vorticity equation. In the electrostatic equation 5.29, we directly expanded the constitutive terms of j_{\parallel} , clearly showing the anisotropic double Laplacian on Φ . In the electromagnetic systems 5.36 and 5.40, we opted to express j_{\parallel} as a separate equation, mostly for clarity and to identify the new terms. We then remain with a single perpendicular Laplacian on Φ , whereas the parallel Laplacian appears as a gradient in the equation on j_{\parallel} succeeded by a divergence. This reveals however some hidden features of the system.

If we decompose the electrostatic vorticity system in the same way, this system essentially takes the form of a Hessenberg index-1 DAE where j_{\parallel} is the algebraic variable —cite—:

$$\begin{cases} \nabla \cdot \left[\frac{m_i n_i}{B^2} \partial_t \nabla_{\perp} \Phi \right] - \nabla \cdot [j_{\parallel} \mathbf{b}] = F_{\Omega} \\ j_{\parallel} = \sigma_{\parallel} (-\nabla_{\parallel} \Phi + T_e \nabla_{\parallel} \log n_e + 1.71 \nabla_{\parallel} T_e) \end{cases} \quad (5.46)$$

However such systems tend to be numerically hard to solve and one common approach —cite— is to replace the zero-side side of the algebraic equation by the time derivative of the algebraic variable with a small coefficient, which effectively transforms the system into a (stiff) ODE. Exactly this has been done in the new formulation of Equation 5.36 with the further benefit that the j_{\parallel} has a physical meaning.

Let us now consider the electromagnetic system with electron inertia, magnetic induction and flutter. The full vorticity system is then given by:

$$\begin{cases} \nabla \cdot \left[\frac{m_i n_i}{B^2} \partial_t \nabla_{\perp} \Phi \right] - \nabla \cdot [j_{\parallel} \mathbf{b}] = F_{\Omega} \\ j_{\parallel} + \frac{\sigma_{\parallel} m_e}{n_e} [\partial_t j_{\parallel} + \nabla \cdot (j_{\parallel} \mathbf{u}_e)] = \sigma_{\parallel} (-\nabla_{\parallel} \Phi + T_e \nabla_{\parallel} \log n_e + 1.71 \nabla_{\parallel} T_e) \\ \quad - (\beta_0 \partial_t A_{\parallel} + \beta_0 \mathcal{D}_A) \\ \quad + \frac{\sigma_{\parallel} m_e}{n_e} \left[\sum_i Z_i [\nabla \cdot (\gamma_i \mathbf{u}_e) + \partial_t \gamma_i] - \mathcal{D}_j^e \right] \\ \nabla \cdot \nabla_{\perp} A_{\parallel} = -j_{\parallel} \end{cases} \quad (5.47)$$

We then have a system over the parallel current j_{\parallel} and the potential fields Φ and A_{\parallel} . In matrix form, this final system reads:

$$\begin{aligned}
 & \begin{pmatrix} \nabla \cdot \left[\frac{m_i n_i}{B^2} \partial_t \nabla_{\perp} \circ \right] & -\nabla \cdot [\circ \mathbf{b}] & 0 \\ \sigma_{\parallel} \nabla_{\parallel} \circ & 1 + \frac{\sigma_{\parallel} m_e}{n_e} \partial_t \circ & \sigma_{\parallel} \beta_0 \partial_t \circ \\ 0 & 1 & \nabla \cdot [\nabla_{\perp} \circ] \end{pmatrix} \begin{pmatrix} \Phi \\ j_{\parallel} \\ A_{\parallel} \end{pmatrix} \\
 & = \begin{pmatrix} F_{\Omega} \\ \sigma_{\parallel} \left(T_e \nabla_{\parallel} \log n_e + 1.71 \nabla_{\parallel} T_e - \frac{m_e}{n_e} \mathfrak{D}_j^e - \beta_0 \mathfrak{D}_A \right) + \mathcal{A}_j \\ 0 \end{pmatrix} \quad (5.48)
 \end{aligned}$$

5.4. Boundary conditions

Boundary conditions are required at the tokamak wall and at the core edge boundary. They need to be defined in both parallel and perpendicular directions to the magnetic field lines.

- In the perpendicular direction, zero Neumann boundary conditions for all plasma variables, i.e., $\partial_{\perp}(\cdot) = 0$, are imposed both at the wall and the core edge boundary except for the electromagnetic potential, which is fixed to $A_{\parallel} = 0$ at the two radial boundaries.
- In the parallel direction, boundary conditions are derived from the generalized Bohm-Chodura sheath boundary conditions [73]. They model the physics of the sheath located next to the limiter wall, where many assumptions used to derive the fluid models (quasi-neutrality, drift-ordering) are no longer valid. They can be expressed as:

- $|\mathbf{v} \cdot \mathbf{n}_{\text{wall}}| \geq |c_s \mathbf{b} \cdot \mathbf{n}_{\text{wall}}|$ with \mathbf{n}_{wall} being the outward normal to the wall, meaning that the outgoing velocity normal to the wall is larger than the parallel sound speed normal to the wall. This property guarantees that the total plasma velocity is oriented outward.
- $\phi_{\mathcal{E},se} = \gamma T \phi_{n,se}$. For each species, $\phi_{\mathcal{E},se}$ is the total energy flux at the sheath entrance, $\phi_{n,se}$ is the particle flux at the sheath entrance, and γ is the sheath transmission factor equal to 2.5 for ions and 4.5 for electrons.
- $j_{\text{wall}} = \left[1 - \exp \left(\Lambda - \frac{\phi}{T_e} \right) \right] \phi_{n,se}$ is the total plasma current on the wall. The ion saturation current is computed from ion particle fluxes $\phi_{n,se}$, and Λ denotes the normalized potential drop in the sheath with $\Lambda \sim 3$.
- $A_{\parallel} = 0$ at the magnetic pre-sheath entrance.

6. Numerical Implementation

6.1. Geometrical consideration

6.1.1. Coordinate system

Let R_0 be the major radius on the magnetic axis and (R, Z, φ) a fixed cylindrical coordinate system. The magnetic equilibrium is assumed to be toroidally symmetric and to encompass both closed and open flux surfaces with singularities at one or more X-points. The last closed flux surface located at the X-point is identified as the separatrix, marking the beginning of the scrape-off layer (SOL), as shown in Fig. ???. The 2D equilibrium magnetic field $\mathbf{B}_{eq} = B_{eq}\mathbf{b}_{eq}$ is a combination of a toroidal field, $\mathbf{B}_{eq,\varphi}$, and a poloidal field, $\mathbf{B}_{eq,p}$, as described in Ref. [83]:

$$\mathbf{B}_{eq} = \mathbf{B}_{eq,\varphi} + \mathbf{B}_{eq,p} = F\nabla\varphi + \nabla\Psi \times \nabla\varphi \quad (6.1)$$

where φ is the toroidal angle, F a toroidal flux function, and $\Psi(R, Z)$ a poloidal flux function from which $\mathbf{B}_{eq,\varphi}$ and $\mathbf{B}_{eq,p}$ are respectively derived (see Sec. 2.1.3). The iso- Ψ surfaces are tangent to the magnetic field and Ψ labels flux surfaces (one value for each flux surface). It is thus natural to define a curvilinear system of coordinates denoted (ψ, θ, φ) . ψ defines a radial coordinate based on the poloidal magnetic flux Ψ , which is by construction always perpendicular to a magnetic flux surface. θ denotes a curvilinear abscissa along the poloidal direction in the (R, Z) plane that defines the poloidal plane, i.e., along iso- Ψ surfaces and orthogonal to $\nabla\varphi$.

In the base $(\mathbf{e}_\psi, \mathbf{e}_\theta, \mathbf{e}_\varphi)$ associated with (ψ, θ, φ) , the magnetic equilibrium field is written as:

$$\mathbf{B}_{eq} = B_{eq,p} \frac{\mathbf{e}_\theta}{|\mathbf{e}_\theta|} + B_{eq,\varphi} \frac{\mathbf{e}_\varphi}{|\mathbf{e}_\varphi|} \quad (6.2)$$

6.1.2. Domain decomposition and mesh design

In order to keep a structured flux-surfaces aligned mesh for any magnetic equilibrium, the real domain is mapped into a Cartesian domain decomposed into multiple connected zones [76]. Each point of the domain is distinctly identified by the set of curvilinear coordinates $[\psi, \theta, \varphi]$ defined in Sec. 6.1.1. The domain is segmented along the toroidal coordinate φ , into N_φ poloidal planes. Tables of data fields are provided for each subdomain. Ghost cells store the information on the neighborhood within a matrix that defines how these subdomains are connected to each other. Depending on

6. Numerical Implementation – 6.1. Geometrical consideration

the domain, these ghost cells contain either the values of the neighboring subdomains' fields or the values imposed by the boundary conditions. An example of the mesh and its zone decomposition is shown in Fig. 6.1, where the X-point requires six zones.

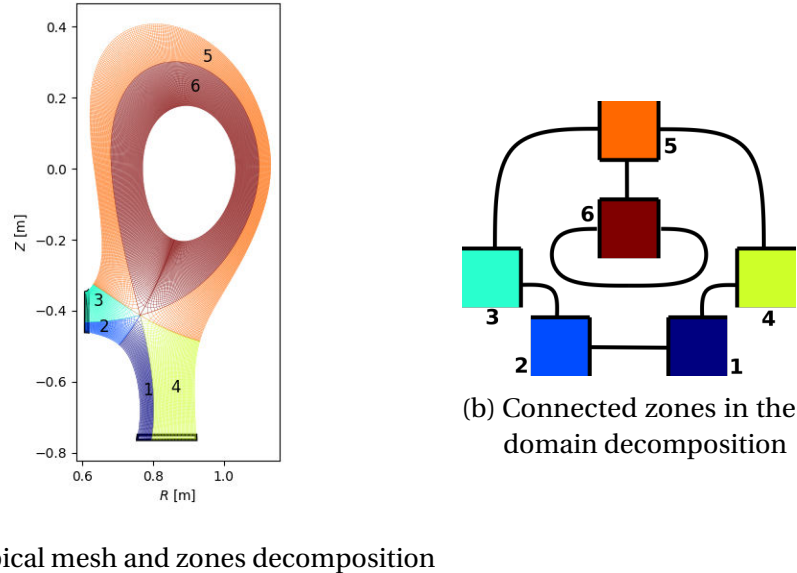


Figure 6.1.: Example of typical mesh and domain decomposition mapping the real domain (a) to a Cartesian multiple zones domain (b). Each colored zone is isomorphic to a cube, the lines connecting the edges indicate the neighbours mapping.

6.1.3. Curvilinear coordinates

The flux-surface-aligned discretization involves a curved grid in poloidal θ and toroidal φ directions. To map the real geometry to the orthonormal grid on each subdomain, we require a metric transformation. The second chapter of the book by D'haeseleer et al [14] describes well the numerical implications of curvilinear grids and serves as the basis of the present implementation.

Let $U = [u^\psi, u^\theta, u^\varphi]^T$ be the three parameters that describe every point in the domain Ω with respect to the curvilinear system of coordinates. On a torus, we can find an invertible transformation R that maps each possible $U \in \Omega$ to a unique point in cartesian coordinates, thus:

$$\begin{bmatrix} x \\ y \\ z \end{bmatrix} = \mathbf{R}(u^\psi, u^\theta, u^\varphi) \quad (6.3)$$

If we fix one parameter and allow the two remaining to vary freely, we obtain the so-called coordinate surface. Analogously if we fix two parameters, we obtain the

6. Numerical Implementation – 6.1. Geometrical consideration

coordinate curve associated to the free parameter and an accommodating choice for the scalar values u^i is the curve length from an arbitrary reference point. At any point $P \in \Omega$, a local basis $\mathbf{e}_\psi, \mathbf{e}_\theta, \mathbf{e}_\varphi$ can be defined by the tangents to the respective coordinate curves crossing this point. Consequently, the basis vectors are easily expressed as:

$$\mathbf{e}_\psi = \frac{\partial \mathbf{R}}{\partial u^\psi} \quad \mathbf{e}_\theta = \frac{\partial \mathbf{R}}{\partial u^\theta} \quad \mathbf{e}_\varphi = \frac{\partial \mathbf{R}}{\partial u^\varphi} \quad (6.4)$$

The parameter choice of u^i can be seen as the curve length and it might or might not be a unit length. The dimension index appears in subscript e_i to indicate that the basis vectors originate from a u^i located below the fraction line.

An alternative basis can be defined from the gradients of the parameters u^i which hence uses a superscript notation:

$$\mathbf{e}^\psi = \nabla u^\psi \quad \mathbf{e}^\theta = \nabla u^\theta \quad \mathbf{e}^\varphi = \nabla u^\varphi \quad (6.5)$$

These basis vectors are orthogonal to the respective coordinate surfaces at the point P . It can be shown that both basis are reciprocal, thus:

$$e^i \cdot e_j = \delta_j^i$$

where δ_j^i is the Kronecker delta.

This leads to the introduction of the covariant (linked to subscripts) and contravariant (linked to the superscripts) components of a vector. As it is known from linear algebra, any vector \mathbf{v} can be expressed with respect to an arbitrary basis $\tilde{\mathbf{e}}_i$ as $\mathbf{v} = \tilde{v}_i \tilde{\mathbf{e}}_i$. For the two previously introduced basis, the respective components of \mathbf{v} are given by:

$$\text{Covariant components: } v_i = \mathbf{v} \cdot \mathbf{e}_i \quad \Rightarrow \quad \mathbf{v} = v_i \mathbf{e}^i \quad (6.6)$$

$$\text{Contravariant components: } v^i = \mathbf{v} \cdot \mathbf{e}^i \quad \Rightarrow \quad \mathbf{v} = v^i \mathbf{e}_i \quad (6.7)$$

$$(6.8)$$

It is common practice to call the representation of \mathbf{v} using the co-/contravariant components the co-/contravariant vector of \mathbf{v} albeit the co- and contravariant vectors both naturally describe the same vector \mathbf{v} .

Next, we introduce the metric coefficients $g_{ij} = \mathbf{e}_i \cdot \mathbf{e}_j$ and their reciprocal metric coefficients $g^{ij} = \mathbf{e}^i \cdot \mathbf{e}^j$. If available, they allow for an easy both-way conversion of contravariant to covariant vectors and consequently an easy change of basis.

$$v_i = g_{ij} v^j \quad \mathbf{e}_i = g_{ij} \mathbf{e}^j \quad (6.9)$$

$$v^i = g^{ij} v_j \quad \mathbf{e}^i = g^{ij} \mathbf{e}_j \quad (6.10)$$

It may be noted that the matrices formed by the indices $i, j \in \{\theta, \psi, \varphi\}$ are each other's inverse matrix.

6.2. The staggered mesh

In order to benefit from the first-order parallel derivative that separates the A_{\parallel} and j_{\parallel} from the other plasma fields Φ , n_e , and T_e (Eqs. ?? and ??), these two variables are defined on a toroidally φ and poloidally θ staggered grid. They are calculated at cell edges in the parallel direction and can be directly matched to the fluxes entering and leaving the collocated cells. One of the major benefits is to minimize numerical diffusion and preserve turbulent structures, following findings in FVM simulations for fluid mechanics [52]. In the radial ψ direction, we keep the collocated position as the only parallel gradient in ψ comes from the flutter term, which in nature is much smaller than the equilibrium field. If the mesh were also staggered in ψ , we would face strong numerical radial diffusion of parallel fluxes, defying the motivation of a staggered grid for A_{\parallel} and j_{\parallel} .

6.2.1. Description and notation of the staggered grid

The scalar variable A_{\parallel} is the magnitude of the parallel magnetic vector potential that is a factor of the unit vector \mathbf{b} in direction of the externally induced magnetic field lines. By construction of the domain, \mathbf{b} has only components in φ and θ directions. So far, all physical quantities are calculated on the collocated grid points at the domain cell centers. In the newly introduced equation on A_{\parallel} , the magnetic vector potential appears homogeneous to the potential, pressure and temperature gradients and the additional A_{\parallel} term in the original equation states that the divergence of A_{\parallel} accounts for the change in vorticity. Thus, A_{\parallel} is always one spatial derivative away from the original quantities. As it is common in classical CFD simulation the velocity, A_{\parallel} is not defined on cell centers but on a staggered grid on the cell edges in ψ -direction. Because the magnetic field lines do not evolve in radial direction and only parallel gradients contribute to A_{\parallel} , its grid is only staggered in poloidal and toroidal directions. To distinguish quantities on both grids, the indexes $[i_{\psi}, i_{\theta} - \frac{1}{2}, i_{\varphi} - \frac{1}{2}]$ describe discrete positions on the staggered grid.

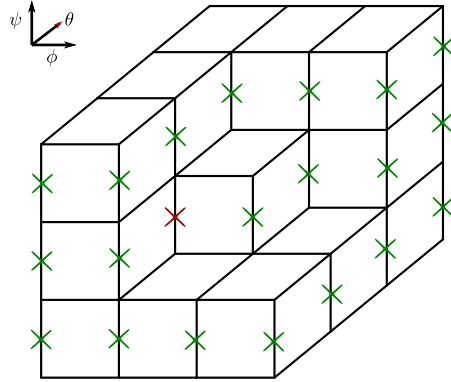


Figure 6.2.: General view of the staggered grid points marked as crosses on top of the collocated cells. The red cross at the position $[i_\psi, i_\theta - \frac{1}{2}, i_\varphi - \frac{1}{2}]$ corresponds to the central cell with index $[i_\psi, i_\theta, i_\varphi]$

In the following work, quantities evaluated at staggered grid points are indicated either by the superscript stg or by a $-\frac{1}{2}$ shift in the index. This means that following notations are equivalent:

$$X_{[i_\psi, i_\theta, i_\varphi]}^{stg} = X_{[i_\psi, i_\theta - \frac{1}{2}, i_\varphi - \frac{1}{2}]} \quad \text{or} \quad X_{[i_\psi, i_\theta + 1, i_\varphi]}^{stg} = X_{[i_\psi, i_\theta + \frac{1}{2}, i_\varphi - \frac{1}{2}]}$$

6.2.2. Boundary cells

Staggered quantities require a different treatment at the domain boundary. On the collocated mesh, cells are located either entirely in the plasma or in the physical wall. Staggered quantities in the boundary layer are thus always half a cell width away from the wall and boundary conditions are enforced accordingly. For the magnetic vector potential this holds for walls in ψ direction but in φ and θ directions, the staggered grid points are on the tokamak wall for the boundary cells with lowest index and one cell width away at the highest index. For consistency, accuracy and symmetry purposes, the staggered solvable domain shall be either extended by one row of cells at the upper index to include the wall in the solution or reduced by one row at the lower end. In both cases, the number of collocated and staggered grid points do not match anymore and inhibit all eventual symmetry properties of the matrix in the dual-grid system (??). A_{\parallel} requires Dirichlet boundary conditions with the value 0 everywhere, thus the solution on the wall is already known and is not needed in the system. The parallel current j_{\parallel} is fixed by the sheath current perpendicular to the wall, but is still needed for the parallel component tangential to the sheath. In Fig. 6.3, the

6. Numerical Implementation – 6.2. The staggered mesh

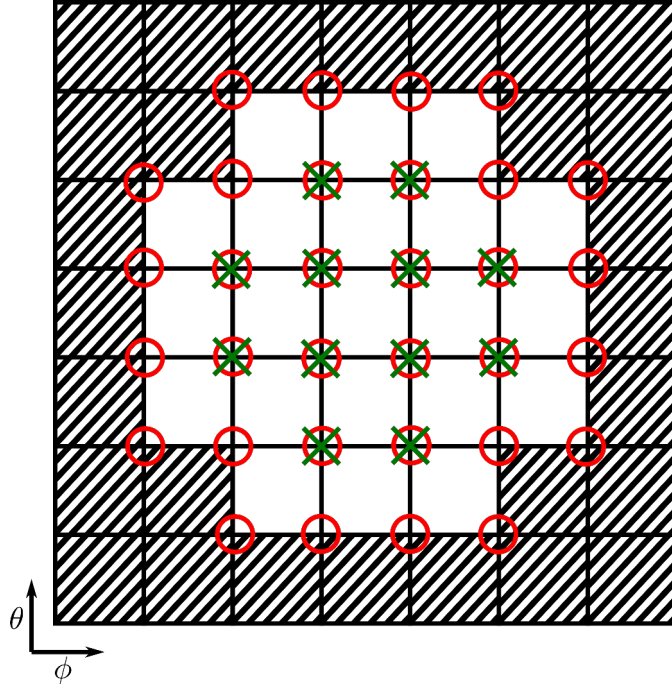


Figure 6.3.: General view of the staggered grid points in the $\theta - \varphi$ plane. The field A_{\parallel} is defined at the green crosses and j_{\parallel} at the red circles. Crossed cells are boundary cells where the mask is $\chi = 1$.

To ensure a correct implementation of the system and the stencils that appear in it, a new mask describes which cells contain staggered grid points in the solvable domain. It is defined from the original collocated wall mask χ as:

$$\chi_{[i_\psi, i_\theta, i_\varphi]}^{A_{\parallel}} = 1 - (1 - \chi_{[i_\psi, i_\theta, i_\varphi]})(1 - \chi_{[i_\psi, i_\theta-1, i_\varphi]})(1 - \chi_{[i_\psi, i_\theta, i_\varphi-1]})(1 - \chi_{[i_\psi, i_\theta-1, i_\varphi-1]}) \quad (6.11)$$

$$\chi_{[i_\psi, i_\theta, i_\varphi]}^{j_{\parallel}} = \chi_{[i_\psi, i_\theta, i_\varphi]} \chi_{[i_\psi, i_\theta-1, i_\varphi]} \chi_{[i_\psi, i_\theta, i_\varphi-1]} \chi_{[i_\psi, i_\theta-1, i_\varphi-1]} \quad (6.12)$$

The value of $\chi^{A_{\parallel}}$ is therefore 1 if the staggered cell with index $[i_\psi, i_\varphi, i_\theta]$ overlaps with the wall and is 0 inside the solvable domain. Conversely, the mask $\chi^{j_{\parallel}}$ is 0 unless the entire cell lies in the wall.

Let us discuss a bit further sheath boundary conditions for staggered fields, where A_{\parallel} and j_{\parallel} lie on the domain boundary. For collocated fields, we impose sheath fluxes from the Bohm-Chodura model (see Sec. 5.4) on the first cell in the simulation domain. For the magnetic potential A_{\parallel} , the 0-Dirichlet condition is imposed in the concerned cell. For the parallel current j_{\parallel} , we add the sheath current j_{wall} to any parallel currents tangential to the wall. Indeed, if the sheath boundary is in the θ direction, the φ component of the parallel current remains unaffected and needs to be solved.

6.2.3. Staggered discrete operators

As the parallel current j_{\parallel} and the magnetic vector potential A_{\parallel} are defined on a staggered grid, new stencil operators are needed to be compatible with the electric potential Φ defined on the collocated grid at the cell centers.

6.2.3.1. Parallel gradient

To calculate the parallel current in Ohm's law, we require the parallel gradients of potential, density and electron temperature. The three fields are defined on the collocated grid, and the result of the operator shall lie on the staggered grid.

$$[\nabla_{\parallel} X]_{[i_{\psi}, i_{\theta}, i_{\varphi}]}^{stg} \quad (6.13)$$

Wave structure travel along the parallel direction, dominated by the equilibrium field \mathbf{b}_{eq} in θ and φ -directions. Because of the high anisotropy given $B_{eq,p} \ll B_{eq,\varphi}$, this operator is prone to numerical dissipation if not properly implemented. Both directions are calculated in a common step

$$\begin{aligned} [\mathbf{b}_{eq} \cdot \nabla X]_{[i_{\psi}, i_{\theta}, i_{\varphi}]}^{stg} = & \frac{1}{2} \left((+b_{stg}^{\theta} + b_{stg}^{\varphi}) X_{[i_{\psi}, i_{\theta}, i_{\varphi}]} + (-b_{stg}^{\theta} + b_{stg}^{\varphi}) X_{[i_{\psi}, i_{\theta}-1, i_{\varphi}]} \right. \\ & \left. + (+b_{stg}^{\theta} - b_{stg}^{\varphi}) X_{[i_{\psi}, i_{\theta}, i_{\varphi}-1]} + (-b_{stg}^{\theta} - b_{stg}^{\varphi}) X_{[i_{\psi}, i_{\theta}-1, i_{\varphi}-1]} \right) \end{aligned} \quad (6.14)$$

This discrete operator involves four neighbors, as shown in Fig. 6.4a. It is appreciated in the finite elements community for anisotropic wave propagation [35, 66, 85] for its good numerical properties and is used in the anisotropic heat diffusion problem in magnetized plasmas by Günter et al [32].

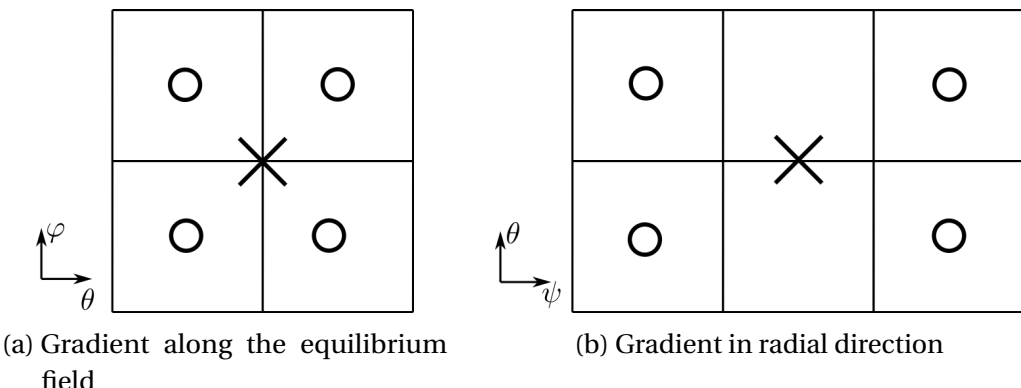


Figure 6.4.: Neighbors involved to calculate staggered parallel gradients

The gradient in radial direction, that comes from the magnetic flutter, is treated in a separate step. Because of the staggered grid configuration, that does not apply to

6. Numerical Implementation – 6.2. The staggered mesh

the radial direction, the gradient requires 8 neighbors, of which four are shown in Fig. 6.4b, the other four being out of plane in the next poloidal plane.

$$\begin{aligned} [\tilde{\mathbf{b}} \cdot \nabla X]_{[i_\psi, i_\theta, i_\varphi]}^{stg} = & \frac{1}{4} b_{stg}^\psi \left(X_{[i_\psi+1, i_\theta, i_\varphi]} - X_{[i_\psi-1, i_\theta, i_\varphi]} + X_{[i_\psi+1, i_\theta, i_\varphi-1]} - X_{[i_\psi-1, i_\theta, i_\varphi-1]} \right. \\ & \left. + X_{[i_\psi+1, i_\theta-1, i_\varphi]} - X_{[i_\psi-1, i_\theta-1, i_\varphi]} + X_{[i_\psi+1, i_\theta-1, i_\varphi-1]} - X_{[i_\psi-1, i_\theta-1, i_\varphi-1]} \right) \end{aligned} \quad (6.15)$$

The poloidal and toroidal components of the magnetic fluctuations are solved together with the equilibrium part in Eq. 6.14.

6.2.3.2. Parallel divergence

The divergence of j_{\parallel} needs to be calculated at the collocated grid in the vorticity equation. It is the counterpart to the gradient operator above, and calculates the divergence on the collocated grid based on staggered fields.

$$[\nabla \cdot X^{stg} \mathbf{b}]_{[i_\psi, i_\theta, i_\varphi]} \quad (6.16)$$

In Equation B.11, the divergence of a parallel vector field has been introduced. We consider a collocated cell as in Figure 6.2. The divergence is then the sum of all in- and outgoing fluxes $\frac{\partial(JXb^i)}{\partial u^i}$ across the six cell faces.

$$[\nabla \cdot X^{stg} \mathbf{b}]_{[i_\psi, i_\theta, i_\varphi]} = \frac{1}{J_{[i_\psi, i_\theta, i_\varphi]}} \left(F_{[i_\psi, i_\theta, i_\varphi]}^{X, \psi} - F_{[i_\psi+1, i_\theta, i_\varphi]}^{X, \psi} + F_{[i_\psi, i_\theta, i_\varphi]}^{X, \theta} - F_{[i_\psi, i_\theta+1, i_\varphi]}^{X, \theta} + F_{[i_\psi, i_\theta, i_\varphi]}^{X, \varphi} - F_{[i_\psi, i_\theta, i_\varphi+1]}^{X, \varphi} \right) \quad (6.17)$$

We want calculate these fluxes from the flux $F^{X, i} = JXb^i$ of the staggered field X^{stg} . As centered cell faces do not overlap with the staggered grid, we need to take the interpolate the fluxes calculated at the staggered mesh onto the cell face. For the equilibrium direction it involves two neighbors per flux (see Fig. 6.5a). As an example, here are the fluxes written out for the incoming poloidal flux:

$$F_{[i_\psi, i_\theta, i_\varphi]}^{X, \theta} = \frac{1}{2} \left(F_{[i_\psi, i_\theta - \frac{1}{2}, i_\varphi - \frac{1}{2}]}^{X, \theta} + F_{[i_\psi, i_\theta - \frac{1}{2}, i_\varphi + \frac{1}{2}]}^{X, \theta} \right)$$

In the radial direction, we need, again, the fluxes at eight neighboring staggered locations to calculate a flux on a single cell face.

$$\begin{aligned} F_{[i_\psi, i_\theta, i_\varphi]}^{X, \psi} = & \frac{1}{8} \left(F_{[i_\psi, i_\theta - \frac{1}{2}, i_\varphi - \frac{1}{2}]}^{X, \psi} + F_{[i_\psi, i_\theta - \frac{1}{2}, i_\varphi + \frac{1}{2}]}^{X, \psi} + F_{[i_\psi, i_\theta + \frac{1}{2}, i_\varphi - \frac{1}{2}]}^{X, \psi} + F_{[i_\psi, i_\theta + \frac{1}{2}, i_\varphi + \frac{1}{2}]}^{X, \psi} \right. \\ & \left. + F_{[i_\psi - 1, i_\theta - \frac{1}{2}, i_\varphi - \frac{1}{2}]}^{X, \psi} + F_{[i_\psi - 1, i_\theta - \frac{1}{2}, i_\varphi + \frac{1}{2}]}^{X, \psi} + F_{[i_\psi - 1, i_\theta + \frac{1}{2}, i_\varphi - \frac{1}{2}]}^{X, \psi} + F_{[i_\psi - 1, i_\theta + \frac{1}{2}, i_\varphi + \frac{1}{2}]}^{X, \psi} \right) \end{aligned}$$

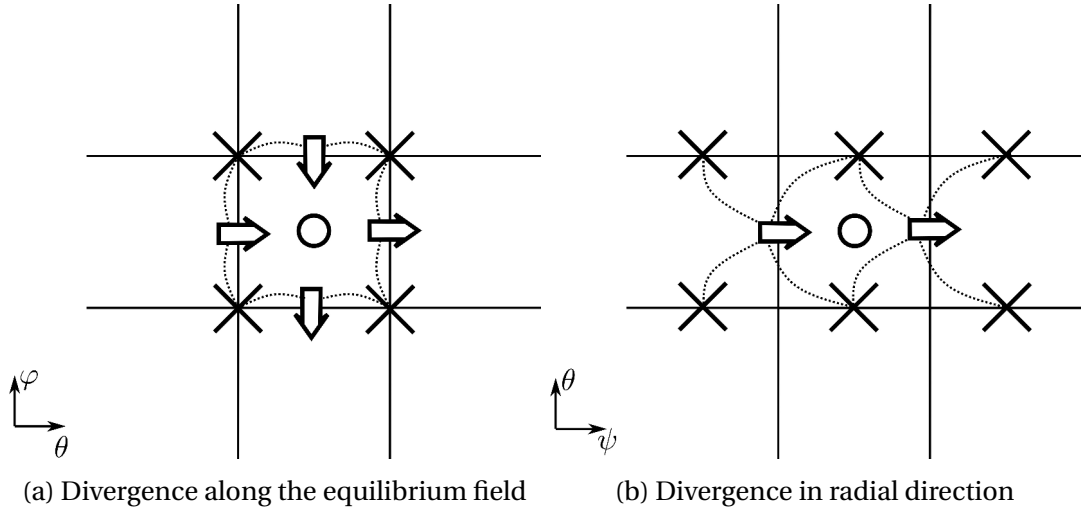


Figure 6.5.: Neighbors involved to calculated the parallel divergence. The arrows indicate the in- and outgoing fluxes that need to be calculated, and the dashed lines connect the arrows to the staggered points they require.

6.2.3.3. Perpendicular Laplacian

Ampère's law requires the perpendicular Laplacian on the staggered grid to link j_{\parallel} and A_{\parallel} , two staggered fields.

$$[\nabla \cdot \nabla_{\perp} X^{stg}]_{[i_{\psi}, i_{\theta}, i_{\varphi}]}^{stg} \quad (6.18)$$

Let us consider a staggered cell over the regular mesh, depicted in red in Fig. 6.6a. Since the Laplacian operator can be treated as a divergence of a gradient, the task . Each flux $F^{Y,i}$ is defined as the perpendicular gradient at the corresponding cell face, approximated with finite differences. The metric and diffusion coefficients $JD(g^{ij} - b^i b^j)$ are also required at the faces and we obtain them by taking their average on the closest collocated points. In poloidal and toroidal directions two collocated points shown in green in Figure 6.6c and Figure 6.6d are sufficient but in radial direction we need to consider eight points around the face to calculate the correct coefficients.

6. Numerical Implementation – 6.2. The staggered mesh

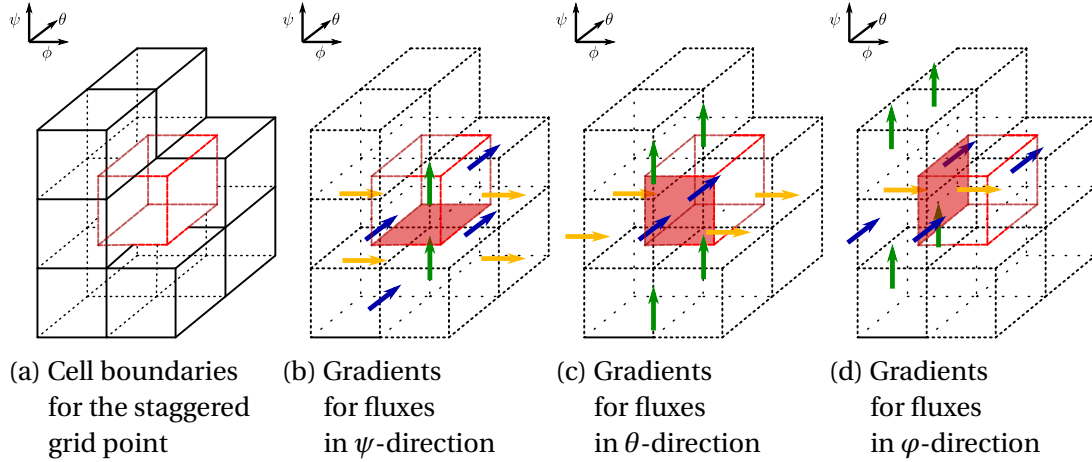


Figure 6.6.: Depiction of the relevant cell faces to calculate fluxes of a staggered field at coordinate index $[i_\psi, i_\theta - \frac{1}{2}, i_\phi - \frac{1}{2}]$

6.2.4. Discretization around the X-point

The staggered grid has direct implications on the estimation of fluxes around mesh singularities: while for regular fields, every cell around the X-point has well-defined neighbors (see Fig. 6.7a), radial fluxes in and out of staggered cells directly cross the X-point (see Fig. 6.7b). They affect the perpendicular Laplacian operator on A_{\parallel} in Ampere's law (Eq. ??), advection on j_{\parallel} in Eq. ??, and the anomalous perpendicular diffusion \mathcal{D}_{\perp} . To cope with the ill-defined cell faces, fluxes across the X-point are forced to 0 by Neumann-like boundary conditions. Neighbors of the involved cells must be defined separately from the regular cells with the same index.

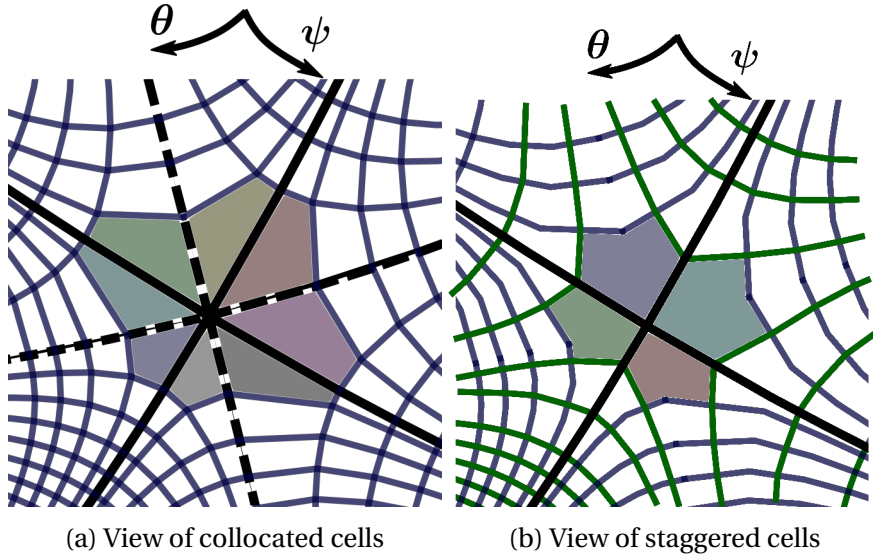


Figure 6.7.: Sketches of the mesh around the X-point. For collocated cells (a), 8 cells touch the X-point at a corner. For staggered cells (b), the X-point is located at the radial face of 4 cells, effectively modifying the shape of the cells to pentagons. Fluxes across the involved faces are hence ill-defined.

6.3. Implicit-explicit solving procedure

The model uses an explicit time discretization for the advection terms and an implicit one for the diffusive terms. In turbulence simulations, we limit ourselves to timescales slower than the cyclotronic frequency ω_C . This applies to all advection phenomena, as well as to friction, pressure, and energy source terms, which can then comfortably be solved explicitly in time.

However, ionization/recombination processes, resistive and viscous effects from the Spitzer-Härm model, and electron inertia involve much faster dynamics that would massively constrain the allowed timestep size. Therefore, these terms are solved implicitly. To reduce numerical complexity, they can be decoupled and solved sequentially for the density, the parallel velocity, the temperature, and finally the potentials.

6.3.1. Time discretization schemes

6.3.1.1. Explicit Runge-Kutta solver

6.3.1.2. Implicit-explicit VSIMEX solver

The time discretization is based on a variable stepsize implicit-explicit scheme (VSIMEX) [82], associating explicit time discretization for the advection terms and an implicit one for the diffusive terms. In turbulence simulations, we limit ourselves to timescales

slower than the cyclotronic frequency ω_C . This applies to all advection phenomena, as well as to friction, pressure, and energy source terms, which can then comfortably be solved explicitly in time.

This multi-step method is implemented for orders 1 to 3, and the timestep is updated such that fluxes and velocities in the simulation domain match a targeted CFL value.

6.3.2. Initialization at Restart

6.3.2.1. Electron Inertia

Use the steady-state Ohm's law from the existing profile in Φ .

6.3.2.2. Parallel Magnetic Vector Potential

Solve for the steady-state Ampère's law with the now available profile in j_{\parallel} . Creation of a new solver class for this purpose.

6.3.3.

6.3.3.1. Finite volumes with flutter

The spatial discretization is based on a second-order conservative finite-volume scheme associated with a 3rd-order WENO reconstruction and Donat, Marquina fluxes for a modified Riemann solver for the advection terms to handle both shocks and complicated smooth solution structures [5, 76].

Each of the In this structure, flutter is treated equivalent to drift velocities.

6.3.3.2. Parallel diffusion operator with flutter

In the magnetostatic setting, the parallel diffusion operator on v_i and T_α can be solved independently on each flux surface in a 2D system on the $\theta - \varphi$ plane. The scheme developed by Günter et al. [32] has proven well-suited to solve the 2D parallel Laplacian equations with minimized numerical spread for highly anisotropic problems. For an operator of the type $\nabla \cdot (\kappa \nabla_{\parallel} \circ \mathbf{b})$, parallel gradients are first calculated in cell corners with finite differences and then used in the fluxes across each cell face to get the divergence. The corners where gradients are calculated are shown in Figure 6.8a. This scheme is particularly effective if the poloidal and toroidal components b^θ and b^φ of the contravariant magnetic unit vector in the curvilinear metric have similar magnitudes. This is usually enforced through careful mesh generation.

However, with flutter (Sec. ??), magnetic flux surfaces are no longer aligned to the $\theta - \varphi$ plane because of the new radial component b^ψ . As a consequence, all indepen-

dent 2D problems across flux surfaces are now coupled into a single 3D problem. For the parallel diffusion solver, a first approach would be to extend the above scheme by calculating gradients in the 3D corners of our cells. However, the new component b^ψ is a pure fluctuation, which is therefore expected to be much smaller than b^θ or b^φ and can even vanish locally. This results in significant spurious numerical diffusion in the radial direction of equilibrium gradients. To prevent this diffusion, and still properly capture radial flutter gradients, only crossed derivatives $b^\theta b^\psi$ and $b^\varphi b^\psi$ as well as the principal radial diffusion $b^\psi b^\psi$ use gradients evaluated at 3D corners, while the equilibrium diffusion remains aligned to the $\theta - \varphi$ plane. Examples of the gradients used in this new scheme are shown in Figs. 6.8b and 6.8c. The new discretization stencil then corresponds exactly to the equilibrium 2D stencil in the limit $b^\psi = 0$.

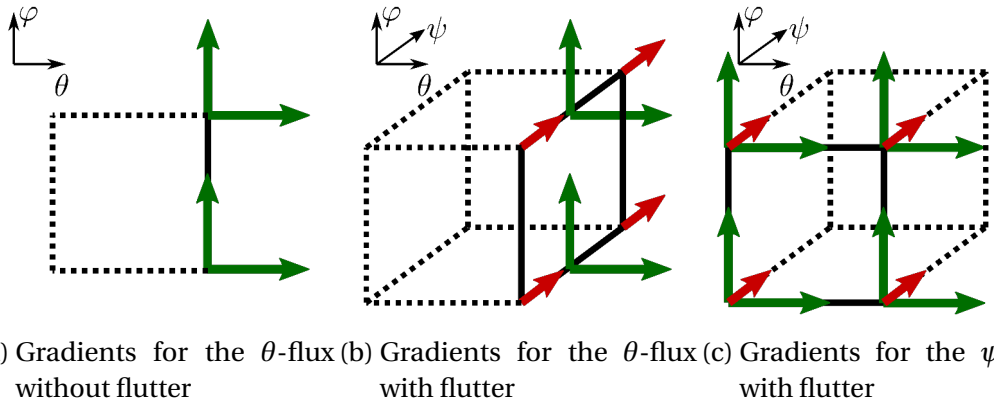


Figure 6.8.: Sketches showing the calculation of gradients for the parallel diffusion scheme. It shows the position where the different gradients are calculated that are relevant for a flux across the cell face with a solid line. Green and red arrows symbolize gradients in the equilibrium and in the radial direction, respectively.

6.4. Electromagnetic vorticity system

The newly introduced fields j_{\parallel} and A_{\parallel} are solved implicitly along with the electric potential Φ . As we face a coupled system that connects all points in the domain, direct solvers such as PASTIX are not suitable, especially for fine 3D meshes. We instead prefer to use iterative solvers available in the PETSc or HYPRE libraries. For the original vorticity system, the Stabilized version of the Biconjugate Gradient method (BiCGStab) along with the Geometric Algebraic Multigrid (GAMG) preconditioner proved to be very efficient and it is desirable to use them on the new systems. This section describes some special numerical features in the construction of the system to facilitate the convergence of the above iterative scheme. [subsubsection 6.4.1.1](#) introduces specific row and column scaling to equilibrate the blocks in the new system

and [subsubsection 6.4.1.2](#) describes how to handle staggered fields to be compatible with the iterative scheme.

6.4.1. Matrix formulation of the electromagnetic system

With the values for n_e and T_e known at time-step $n + 1$, the vorticity equation (Eq. ??) corresponds to a 3D costly system involving Φ , j_{\parallel} , and A_{\parallel} . To solve it efficiently, the j_{\parallel} advection and perpendicular diffusion are treated explicitly, allowing the integration of Ohm's law into the vorticity equation and Ampère's law. Then, at time-step $n + 1$, the following dimensionless system coupling the two potentials Φ and A_{\parallel} must be solved:

$$\begin{pmatrix} \nabla \cdot [D_{\perp} \nabla_{\perp} \circ] + \nabla \cdot [D_{\parallel} \nabla_{\parallel} \circ \mathbf{b}] & \frac{\beta_0}{\delta_t} \nabla \cdot [D_{\parallel} \circ \mathbf{b}] \\ -D_{\parallel} \nabla_{\parallel} \circ & \frac{\beta_0}{\delta_t} D_{\parallel} \circ -\nabla \cdot [\nabla_{\perp} \circ] \end{pmatrix} \begin{pmatrix} \Phi^{n+1} \\ A_{\parallel}^{n+1} \end{pmatrix} = \begin{pmatrix} \nabla \cdot [D_t j_{\parallel}^n \mathbf{b}] + \text{RHS}^{\Phi} \\ D_t j_{\parallel}^n + \text{RHS}^{A_{\parallel}} \end{pmatrix} \quad (6.19)$$

with $D_{\perp} = \frac{m_i n_i}{B^2 \delta_t}$, $D_{\parallel} = \frac{1}{\eta_{\parallel} + \mu}$, $D_t = \frac{\mu}{\eta_{\parallel} + \mu}$, and $\mu = m_e / (n_e \delta_t)$ accounting for electron inertia effects. The parameter δ_t derives from the integration scheme and is equal to the time-step in the case of a first-order implicit Euler scheme.

Since $\eta_{\parallel} \propto T_e^{-1.5}$, the parallel resistivity η_{\parallel} is often a small parameter that leads to strong anisotropy between the perpendicular and parallel Laplacian operators. However, the electron inertia term, being implemented in the current solver, acts as an upper limit for the parallel diffusion coefficient, which is expected to improve the matrix conditioning as η_{\parallel} approaches zero. This is in contrast to the original electrostatic model from [5].

6.4.1.1. Equilibration of the Matrix Blocks

The matrices in the electromagnetic model ?? can be decomposed in 2x2 or 3x3 block matrices that apply on the respective fields Φ , A_{\parallel} and/or j_{\parallel} . Apart of the use of dedimensionalized quantities, no effort was made so far to ensure that the blocks are roughly of the same order of the magnitude, which is important for the condition number of the matrix, nor that the matrix is diagonally dominant, which is generally a desirable feature for fast convergence of iterative schemes.

In the following bits, we introduce some column c_X and row r_X scaling factors that are specific to the blocks X of the matrix such that the above conditions are fulfilled as well as possible. To ensure a correct solution, the row scaling factor r_X must be applied to the corresponding entry in the RHS vector and as a matter of fact, in the original

vorticity matrix, we already have $r_\Phi = J$ the metrical Jacobian from subsection 6.1.3 to remove the effect of different mesh sizes in the domain on the discrete Laplacian operators. The column scaling factors c_X must be taken care of when retrieving the fields from the numerical solution and it is strongly recommended to apply them to the initial guess for the iterative scheme.

Some existing algorithms optimize the scaling task such as — cite —. However, they all require an expensive matrix analysis phase that must be repeated regularly since the matrix changes with the progress of the simulation. Therefore, we use the knowledge about the construction of the matrix blocks to define sufficiently good scaling factors. An educated row and column scaling can considerably increase the condition number of a matrix[80].

Due to the large size of the system, it must be resolved using iterative solvers. Note that the two diagonal blocks already have a convenient shape, and the anti-diagonal blocks contain parallel divergence and gradient operators, whose discrete stencils are very similar. Therefore, by scaling both the second column and row with $\sqrt{\delta_t/\beta_0}$, the resulting matrix becomes almost symmetric, which is convenient for most iterative solvers.

6.4.1.2. Staggered Fields in the Matrix

The GAMG multigrid solves the system on different coarser levels by restricting the matrix and the RHS vector and then interpolates the solution back to the finer levels. In the new system, two consecutive entries belong to different fields, which makes the whole restriction-interpolation task obsolete from the very first level since neither the solution nor the matrix entries are similar between neighbours. In general, PETSc takes care of multiple fields in a coupled system if one defines a block size (in our case either 2 or 3) that indicates GAMG how to match corresponding entries.vim However, as seen in ??, the fields A_{\parallel} and j_{\parallel} are defined on a staggered grid in poloidal and toroidal directions as opposed to the collocated field for Φ . For the system it means that at each wall in negative directions (at the left target and for non-axisymmetric geometries), a line and column for Φ exists but not for the two other fields. This in turn is problematic for GAMG as the blocks are globally defined and two different fields would again end up together and the total system size might even not be a multiple of the blocksize (2 resp. 3), which at all prevents the initialization of the preconditioner.

6.4.2. Treatment of flutter

6.4.2.1. Parallel diffusion on Φ

For the parallel diffusion on the electric potential $\nabla \cdot [D_{\parallel} \nabla_{\parallel} \Phi \mathbf{b}]$ with flutter, we do not use the stencil introduced in Sec. 6.3.3.2. To avoid numerical difficulties and the appearance of unphysical modes, the discretization of this term needs to be consistent with the parallel gradient and divergence operators in the same system. Since

the grid for A_{\parallel} and j_{\parallel} is only staggered in the θ and φ directions, we do not know them in the radial corners from Figs. 6.8b and 6.8c. Instead, the discrete diffusion operator is defined as the combination of the operators for the gradient and the divergence. It involves two neighbors on both radial sides, so the resulting stencil is less compact but consistent with the remaining system. Note that in cases without flutter ($b^{\psi} = 0$), the diffusion operator exactly corresponds to Günter's scheme [32] because the staggered fields are known at the position of the green gradients in Fig. 6.8.

6.4.3. Evaluation of the condition number

The electromagnetic vorticity system needs to be solved implicitly, and the condition number of the matrix is an important property that essentially defines the speed of convergence of iterative solvers. Extensive research in the past decade[[strakos1991linear](#), [19](#), [30](#), [57](#)], particularly on GMRES and conjugate gradient methods as they are used in SOLEDGE3X, has shown that a high condition number results in an increased number of iterations to reach convergence. The condition number of a matrix \mathbf{M} is defined as the ratio between its largest and smallest eigenvalues:

$$\kappa(\mathbf{M}) = \frac{|\lambda_{\max}(\mathbf{M})|}{|\lambda_{\min}(\mathbf{M})|} \quad (6.20)$$

It is therefore of particular interest to investigate how the electromagnetic extension of the system affects the conditioning of the vorticity system. While there are efficient algorithms to estimate the largest eigenvalue of a matrix, the smallest is much more expensive to compute. For the large 3D vorticity system, directly calculating the condition number is not feasible. Instead, we approach this question analytically.

Consider a 2D orthonormal system, with perpendicular gradients exclusively in the x direction and parallel gradients in the y direction, with $N_x \times N_y$ discretization points. All fields are assumed to take some constant reference value, the timestep size is fixed to δ_t , and time advancement is performed using the first-order implicit Euler method. Without a curvilinear grid, the gradient and divergence stencils are identical, and with the row/column scaling from Sec. 6.4.1.1, the vorticity system can then be expressed as:

$$\mathbf{M} = \begin{pmatrix} \alpha \mathbf{L}_{\perp} + \sigma \mathbf{L}_{\parallel} & \gamma \mathbf{G}_{\parallel} \\ -\gamma \mathbf{G}_{\parallel}^T & \sigma \mathbf{I} - \gamma^2 \mathbf{L}_{\perp} \end{pmatrix} \quad (6.21)$$

where $\alpha = \frac{m_i n_i}{B^2 \delta_t}$, $\sigma = \frac{1}{\eta_{\parallel} + \frac{m_e}{n_e \delta_t}}$, and $\gamma = \sqrt{\frac{\delta_t}{\beta_0}}$. The stencil matrices \mathbf{L}_{\perp} and \mathbf{L}_{\parallel} describe the Laplacians between the x and y neighbors, respectively, while \mathbf{G}_{\parallel} represents the gradient over y . Their matrices take the following forms:

$$\begin{aligned}
 \mathbf{L}_\perp &= \begin{pmatrix} -2 & 1 & 0 & \cdots & 0 \\ 1 & -2 & 1 & \cdots & 0 \\ 0 & 1 & -2 & \cdots & 0 \\ \vdots & \vdots & \vdots & \ddots & \vdots \\ 0 & 0 & 0 & \cdots & -2 \end{pmatrix}_{N_x \times N_x} & \mathbf{L}_\parallel &= \begin{pmatrix} -2 & 1 & 0 & \cdots & 1 \\ 1 & -2 & 1 & \cdots & 0 \\ 0 & 1 & -2 & \cdots & 0 \\ \vdots & \vdots & \vdots & \ddots & \vdots \\ 1 & 0 & 0 & \cdots & -2 \end{pmatrix}_{N_y \times N_y} \\
 \mathbf{G}_\parallel &= \begin{pmatrix} -1 & 1 & 0 & \cdots & 0 \\ 0 & -1 & 1 & \cdots & 0 \\ \vdots & \vdots & \vdots & \ddots & \vdots \\ 1 & 0 & 0 & \cdots & -1 \end{pmatrix}_{N_y \times N_y}
 \end{aligned} \tag{6.22}$$

In order to make the system invertible and avoid an infinite condition number, we assume Dirichlet-0 boundary conditions in the perpendicular direction and periodic boundary conditions in the parallel direction. This can be viewed as a region of closed flux surfaces connected to a region with a very crude sheath-dominated plasma. We can compute the eigenvalues of the two Laplacians and the gradient coupling matrix exactly.

$$\lambda_{k_x}(\mathbf{L}_\perp) = 4 \sin^2\left(\frac{(k_x + 1)\pi}{2N_x}\right) \quad \lambda_{k_y}(\mathbf{L}_\parallel) = 4 \sin^2\left(\frac{k_y\pi}{N_y}\right) \quad \lambda_{k_y}(\mathbf{G}_\parallel) = i \sin\left(\frac{k_y\pi}{N_y}\right) \tag{6.23}$$

where $k_x \in [0, N_x - 1]$ and $k_y \in [0, N_y - 1]$ are indices for all eigenvalues. We observe that both parallel systems have a zero eigenvalue that corresponds to a constant mode, due to the periodic boundary conditions along the closed flux surfaces, indicating that the solution can be determined up to a constant. The perpendicular operators, with fixed boundaries, make the system invertible with a unique solution.

Let us now evaluate the extremal eigenvalues of the diagonal blocks of \mathbf{M} . For the upper-left block, which contains the sum of Laplacians, the eigenvalues correspond to the combinations of (k_x, k_y) such that $|\lambda_{k_x}| + |\lambda_{k_y}|$ is minimized or maximized:

$$\lambda_{min}(\alpha\mathbf{L}_\perp + \sigma\mathbf{L}_\parallel) = \alpha \cdot \frac{\pi^2}{N_x^2} \quad \lambda_{max}(\alpha\mathbf{L}_\perp + \sigma\mathbf{L}_\parallel) = 4(\alpha + \sigma) \tag{6.24}$$

For the lower-right block matrix, the identity matrix will shift the eigenvalues of the perpendicular Laplacian by σ :

$$\lambda_{min}(\sigma\mathbf{I} - \gamma^2\mathbf{L}_\perp) = \sigma - 4\gamma^2 \quad \lambda_{max}(\sigma\mathbf{I} - \gamma^2\mathbf{L}_\perp) = \sigma - \gamma^2 \frac{\pi^2}{N_x^2} \tag{6.25}$$

For sufficiently large systems, the largest eigenvalue will be on the order of σ . If $\sigma \gg \gamma^2$, all eigenvalues will be close to σ , resulting in an excellent matrix condition.

6. Numerical Implementation – 6.4. Electromagnetic vorticity system

However, if $\sigma < 4\gamma^2$, some eigenvalues may become negative, causing the system to lose its positive-definiteness. This can lead to strong instabilities, and standard iterative solvers (e.g., GMRES or BiCGStab) may fail or produce unreliable results, as these methods are generally designed for positive-definite matrices. To ensure that the problem remains well-posed, we must enforce the constraint:

$$\frac{1}{4}\beta_0 > \delta_t \eta_{\parallel} + \frac{m_e}{n_e} \quad (6.26)$$

This condition states that β_0 cannot be too small for the system to remain solvable. Assuming this lower condition on β_0 holds with a sufficient margin, the minimum and maximum eigenvalues in Eq. 6.25 are simply $\lambda_{min} = \lambda_{max} = \sigma$.

We now have all extremal eigenvalues along the block diagonal. For the combined matrix \mathbf{M} , the gradient coupling plays a crucial role. If the coupling is small, the eigenvalues of \mathbf{M} are given by the union of the eigenvalues of the diagonal blocks. The condition number of \mathbf{M} is then the ratio of the overall maximum and minimum eigenvalues of the block matrices. Since γ is certainly smaller than σ , we should investigate the impact of the coupling in more detail. The matrix \mathbf{M} can be transformed into a block diagonal form by applying the Schur complement \mathbf{S} on the lower-left block.

$$\mathbf{M} = \begin{pmatrix} \mathbf{A} & \mathbf{B} \\ -\mathbf{B}^T & \mathbf{C} \end{pmatrix} = \begin{pmatrix} \mathbf{I} & 0 \\ -\mathbf{B}^T \mathbf{A}^{-1} & \mathbf{I} \end{pmatrix} \begin{pmatrix} \mathbf{A} & 0 \\ 0 & \mathbf{S} \end{pmatrix} \begin{pmatrix} \mathbf{I} & \mathbf{A}^{-1} \mathbf{B} \\ 0 & \mathbf{I} \end{pmatrix} \quad \text{with: } \mathbf{S} = \mathbf{D} + \mathbf{B}^T \mathbf{A}^{-1} \mathbf{B} \quad (6.27)$$

The block diagonal matrix is multiplied by both a lower and an upper diagonal matrix. Since they are invertible and all diagonal elements are equal to 1, the block diagonal matrix is quasi-similar to \mathbf{M} [27], thereby preserving its eigenvalues. Calculating the eigenvalues of the block diagonal matrix gives us then a good approximation for the actual eigenvalues of \mathbf{M} . We now need to estimate the eigenvalues of the Schur complement. Given that \mathbf{A} is Laplacian-based, the eigenvalues of \mathbf{A}^{-1} are the reciprocals of the eigenvalues of \mathbf{A} , as shown in Eq. 6.24. The matrix is sandwiched between the gradient operator and its transpose, and together they behave like a parallel Laplacian with the scaling factor γ^2 . We can first estimate:

$$\lambda_{min}(\mathbf{B}^T \mathbf{A}^{-1} \mathbf{B}) = \frac{\gamma^2 \lambda_{min}(L_{\parallel})}{\lambda_{max}(\alpha \mathbf{L}_{\perp} + \sigma \mathbf{L}_{\parallel})} = 0 \quad (6.28)$$

$$\lambda_{max}(\mathbf{B}^T \mathbf{A}^{-1} \mathbf{B}) = \frac{\gamma^2 \lambda_{max}(L_{\parallel})}{\lambda_{min}(\alpha \mathbf{L}_{\perp} + \sigma \mathbf{L}_{\parallel})} = \frac{4\gamma^2 N_x^2}{\alpha \pi^2} \quad (6.29)$$

By combining this result with the eigenvalues of $\sigma \mathbf{I} - \gamma^2 \mathbf{L}_{\perp}$ from Eq. 6.25, we can estimate the extremal eigenvalues of the Schur complement:

$$\lambda_{min}(\mathbf{S}) = \sigma \quad \lambda_{max}(\mathbf{S}) = \sigma + \frac{4\gamma^2 N_x^2}{\alpha\pi^2} \quad (6.30)$$

Everything is now in place to address the eigenvalues of \mathbf{M} with the two block diagonals \mathbf{A} and \mathbf{S} . Recall the assumption $\sigma \gg \gamma^2$ from Eq. 6.26, thus the double-Laplacian system in Eq. 6.24 defines the minimum eigenvalue of \mathbf{M} . Considering that $\alpha \sim 1/\delta_t$ in the dimensionless equations and $\gamma^2 \sim \delta_t/\beta_0$ is large, we can reasonably expect $\gamma^2 \gg \alpha$. The maximum eigenvalue of \mathbf{M} arises from the Schur complement in Eq. 6.30. Therefore, the condition number of \mathbf{M} can be estimated as:

$$\kappa(\mathbf{M}) \approx \frac{\sigma N_x^2}{\alpha\pi^2} + \frac{4\gamma^2 N_x^4}{\alpha^2\pi^4} \quad (6.31)$$

or in terms of dimensionless reference values:

$$\boxed{\kappa(\mathbf{M}) \approx \frac{B^2 \delta_t N_\perp^2}{m_i n_i \pi^2} \cdot \frac{1}{\eta_\parallel + \frac{m_e}{n_e \delta_t}} + \frac{4 \delta_t^3 B^4 N_\perp^4}{\beta_0 m_i^2 n_i^2 \pi^4}} \quad (6.32)$$

In the case of the system with electron inertia, but without electromagnetic induction, the analysis becomes much simpler as only the double Laplacian block matrix constitutes the system. Its condition number is given by the eigenvalues in Eq. 6.24:

$$\kappa(\mathbf{A}) = \frac{4\sigma N_x^2}{\alpha\pi^2} + \frac{4N_x^2}{\pi^2} \quad (6.33)$$

and is primarily determined by the first term. It can be written as:

$$\boxed{\kappa(\mathbf{A}) \approx \frac{B^2 \delta_t N_\perp^2}{m_i n_i \pi^2} \cdot \frac{1}{\eta_\parallel + \frac{m_e}{n_e \delta_t}}} \quad (6.34)$$

From these expressions for the condition number, we observe a degradation as the electric resistivity approaches zero, aligning with the difficulties faced by the original electrostatic implementation in higher-power scenarios. The finite electron mass acts as a lower bound for η_\parallel , which is expected to significantly aid iterative solvers in such scenarios. Magnetic induction introduces the second term in Eq. 6.32, and will always deteriorate the matrix conditioning. However, it is inversely proportional to β_0 , such that the deterioration is limited as the pressure ratio increases. Numerically, electromagnetic effects should only be considered in simulation scenarios where β_0 is sufficiently large. This point is further emphasized by the condition in Eq. 6.26, which imposes a lower limit on β_0 to ensure a positive-definite matrix—an essential property for most iterative solvers. In Fig. 6.9, we illustrate how the condition number changes with η_\parallel , δ_t , and N_\perp for both electrostatic and electromagnetic systems, with and without electron inertia.

6. Numerical Implementation – 6.4. Electromagnetic vorticity system

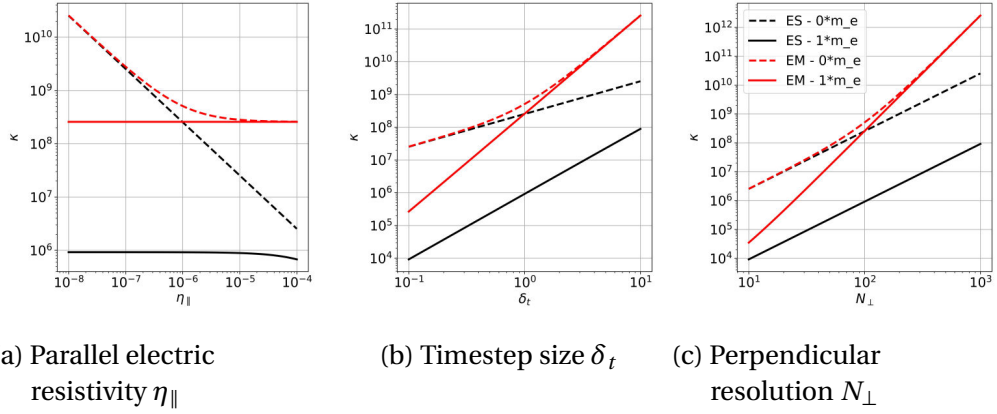


Figure 6.9.: Impact of different parameters on the condition number. Plasma parameters are taken as constant: $B = 1$, $m_i = 2$, $n_e = n_i = 2$, $m_e = 5.5 \cdot 10^{-4}$, $\beta_0 = 10^{-3}$, $\eta_{\parallel} = 10^{-6}$, $\delta_t = 1$ and $N_{\perp} = 100$. The parameters β_0 and n_e are deliberately chosen large to ensure the validity of the positive-definiteness condition 6.26. Black curves correspond to the electrostatic system, and red curves to the electromagnetic matrices, with full lines indicating electron inertia and dashed lines representing $m_e = 0$.

Overall, electromagnetic models exhibit a higher condition number. In particular, at larger timestep sizes or higher perpendicular resolutions, κ increases significantly due to the third and fourth exponents in the second term of Eq. 6.32. However, electron inertia positively affects the condition number. This is especially evident as η_{\parallel} approaches zero in Fig. 6.9a, where neglecting the electron mass results in a sharp increase in κ , while electron inertia allows for a stable, low κ . Similarly, for low timestep sizes and resolutions, m_e improves the system, such that for lower ranges, the electromagnetic system with inertia performs better than the electrostatic system without inertia.

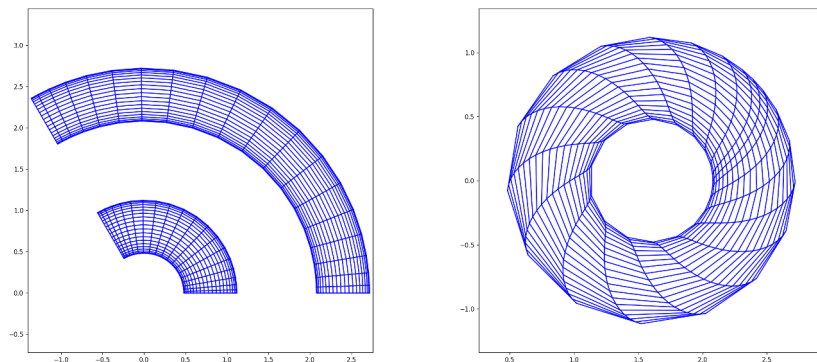
7. Verification and Validation

7.1. Verification by the Method of manufactured solutions

To ensure the correctness of the newly implemented system with the magnetic vector potential A_{\parallel} , a test model has been set up with the method of manufactured solutions (MMS) [65]. This allows to directly compare the numerical and analytic solutions and therefore validate the implementation and verify the order of convergence of the numerical operators.

7.1.1. Test system

The MMS test model is a fraction of a torus with a circular cross-section with an inner radius of 0.48m, an outer radius of 2.72m and a simulated plasma edge width of 0.64m. An example of the 3D mesh geometry is shown in Figure 7.1. To test the information exchange between zones in the model topology from ??, each coordinate direction is split in two zones totaling to 8 zones.



(a) Top view of the $\psi - \varphi$ plane
the two bands correspond to the poloidal angles 0 and π

(b) View of a cross-section of the torus
in the $\psi - \theta$ plane
The cross-section is at $\varphi = 0$

Figure 7.1.: Distorted MMS mesh geometry with $N = 20$ cells per dimension on a 3rd of a torus

7. Verification and Validation – 7.1. Verification by the Method of manufactured solutions

In the MMS geometry, ψ denotes the radius of the tube and R the radius of the entire torus. If $aR_0 = 1.6$ is the distance of the tube center to the torus center, we have:

$$R = aR_0 + \psi \cdot \cos(\theta)$$

Together with the poloidal coordinate $\theta \in [0, 2\pi]$ and the toroidal coordinate $\varphi \in [0, 2\pi/N_{div}]$ where $1/N_{div}$ is the considered fraction of the torus, each point in the domain is uniquely described by the curvilinear coordinates $[\psi, \theta, \varphi]$. We can define some $\vec{P} = [X, Y, Z]^T$ in a cartesian basis of the 3D domain:

$$X = R \cos(\varphi) \quad Y = \psi \cdot \sin(\theta) \quad Z = R \sin(\varphi)$$

In this setting, the basis vectors of the curvilinear coordinates from [subsection 6.1.3](#) can be calculated analytically. The covariant basis vectors are:

$$\vec{e}_\psi = \frac{\partial \vec{P}}{\partial \psi} = \begin{bmatrix} \cos(\theta) \cos(\varphi) \\ \sin(\theta) \\ \cos(\theta) \sin(\varphi) \end{bmatrix} \quad \vec{e}_\theta = \frac{\partial \vec{P}}{\partial \theta} = \begin{bmatrix} -\psi \sin(\theta) \cos(\varphi) \\ \psi \cos(\theta) \\ -\psi \sin(\theta) \sin(\varphi) \end{bmatrix} \quad \vec{e}_\varphi = \frac{\partial \vec{P}}{\partial \varphi} = \begin{bmatrix} -Z \\ 0 \\ X \end{bmatrix}$$

We can further calculate the metric coefficients:

$$g_{ij} = \vec{e}_i \cdot \vec{e}_j = \begin{bmatrix} 1 & 0 & 0 \\ 0 & \psi^2 & 0 \\ 0 & 0 & R^2 \end{bmatrix} \quad \text{and} \quad J = \sqrt{\det[g_{ij}]} = \psi R$$

As generally required by S3X, the magnetic field is axisymmetric and thus does not depend on the toroidal coordinate φ . By construction, it only has a poloidal and a toroidal component but no radial component, which are given in [Equation 7.1](#).

$$\begin{cases} B_\theta = \frac{1}{aR} \Psi_0 & \text{poloidal magnetic field} \\ B_\varphi = \frac{R_0}{R} B_0 & \text{toroidal magnetic field} \end{cases} \quad (7.1)$$

The magnetic field parameters are chosen such that the ratio of toroidal over poloidal magnetic field strength is $aR_0 B_0 / \Psi_0 = 12$. Tests have been performed on various mesh geometries in the scope of S3X from a perfectly regular grid with equally spaced cells in all coordinate directions to the distorted mesh depicted above. As the program can be either executed in a 2D or 3D mode with adapted stencils and geometry calculations, MMS tests have been developed for both scenarios.

7.1.2. Analytic solution

We are interested in the vorticity system on the electric potential Φ and the parallel magnetic vector potential A_{\parallel} . We postulate that their analytic form is:

$$\Phi = \Phi_0 \left(1 + 0.1 \cos(\theta) \cos\left(\frac{\varphi}{N_{div}}\right) \sin\left(2\pi \frac{\psi - \psi_{min}}{\psi_{max} - \psi_{min}}\right) \right) \quad (7.2)$$

$$A_{\parallel} = A_{\parallel,0} \left(1 + 0.1 \cos(\theta) \cos\left(\frac{\varphi}{N_{div}}\right) \sin\left(2\pi \frac{\psi - \psi_{min}}{\psi_{max} - \psi_{min}}\right) \right) \quad (7.3)$$

A similar expression is chosen for the densities $n_{i/e}$ and temperatures $T_{i/e}$ that also contribute to the vorticity equation. The entire form of the test equation is:

$$\begin{cases} \partial_t \vec{\nabla} \cdot \left(\frac{m_i n_i}{B^2} \vec{\nabla}_{\perp} \Phi \right) + \vec{\nabla} \cdot \sigma_{\parallel} \left(\nabla_{\parallel} \Phi \vec{b} + \partial_t A_{\parallel} \right) &= \partial_t \Omega_{\pi} + \vec{\nabla} \cdot \sigma_{\parallel} \left(+ \frac{T_e}{e} \nabla_{\parallel} \log(n_e) \vec{b} + \frac{1.71}{e} \nabla_{\parallel} T_e \vec{b} \right) - S_{\Phi}^{MMS} \\ \vec{\nabla} \cdot \left(\vec{\nabla}_{\perp} A_{\parallel} \vec{b} \right) - \mu_0 \sigma_{\parallel} \left(\nabla_{\parallel} \Phi + \partial_t A_{\parallel} \right) &= -\mu_0 \sigma_{\parallel} \left(\frac{T_e}{e} \nabla_{\parallel} \log(n_e) + \frac{1.71}{e} \nabla_{\parallel} T_e \right) - S_{A_{\parallel}}^{MMS} \\ \Omega_{\pi} = \vec{\nabla} \cdot \left(\frac{m_i}{Z_i B^2} \vec{\nabla}_{\perp} [nT] \right) & \end{cases} \quad (7.4)$$

The main difference to the original system of equations in ?? are the MMS source terms S_{Φ}^{MMS} and $S_{A_{\parallel}}^{MMS}$. They contain the analytic evaluation of all other time-independant terms in the respective line of the equation. The derivatives on curvilinear coordinates can be calculated analytically with the metric theory discussed in [subsection 6.1.3](#). Boundary conditions are enforced by a penalty method on the boundary cell layer where the two quantities are set to their analytic expression. The MMS system is initialized with the analytic expressions for Φ and A_{\parallel} in [Equation 7.3](#) and uniquely the vorticity equation is solved for one timestep. We are in a steady state, so the numerical solution after the first timestep should be equal to the initial state.

One drawback of a steady state system is that time derivatives are always assumed to vanish and terms such as Ω_{π} , the perpendicular Laplacian of Φ or the divergence of A_{\parallel} are not confronted to their analytic form. To catch these terms, we add the vorticity Ω to the MMS system and include it in the subsequent analysis. It is initialized with its analytic form:

$$\Omega = \Omega_{\pi} + \vec{\nabla} \cdot \left(\frac{m_i n_i}{B^2} \vec{\nabla}_{\perp} \Phi \right) + \vec{\nabla} \cdot \sigma_{\parallel} A_{\parallel}$$

and then calculated numerically after the first timestep. This allows to compare a numerical and an analytic form of the vorticity and hence all terms in [Equation 7.4](#).

7.1.3. Order of convergence

-
-
-

Describe

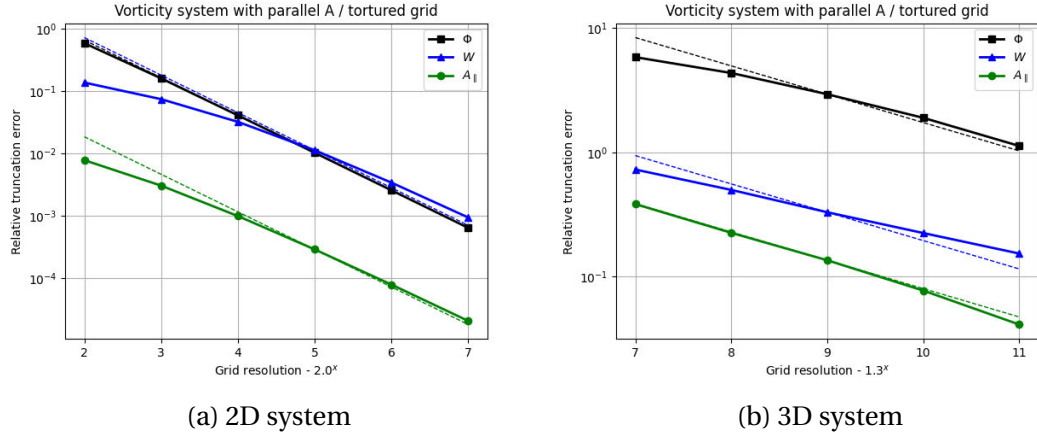


Figure 7.2.: Relative error between the initial plasma and the solution after one timestep. The x -axis indicates the number of points per zone in each direction, the total number of points is thus $N_{tot}^{3D} = 8 \cdot X^3$ (resp. $N_{tot}^{2D} = 4 \cdot X^2$). The dashed lines indicate the slope of the ideal 2nd order convergence

this beautiful graph

Thanks.

7.2. Linear Analysis

....

7.2.1. Pure advection

A first step to verify the correct physical behaviour of the simulation would be to investigate the plasma advection equations.

For this objective we set up a simplistic plasma model on a rectangular 2D SLAB topology. Periodic boundary conditions in all directions allow to properly observe wave propagation without any inference at the domain boundaries. In an isothermal hydrogen plasma without source terms and drifts, the governing equations then simplify to:

$$\partial_t n_i + \vec{\nabla} \cdot (n_i \vec{u}_i) = 0 \quad (7.5)$$

$$n_e = n_i \quad (7.6)$$

$$\partial_t (m_i n_i u_{\parallel}) + \vec{\nabla} \cdot (m_i n_i u_{\parallel} \vec{u}_i) = -2 T_e \vec{\nabla}_{\parallel} n_e \quad (7.7)$$

In this simple plasma, only the density and the velocity evolve over time and depend on each other. The electric potential Φ can also be computed and observed, but it does not interfere with the system because the parallel electric field in the momentum balance [Equation 7.7](#) is calculated from the electron pressure gradient $E_{\parallel} = (\vec{\nabla}_{\parallel} p_e + R_e)/n_e$.

To perform the linear analysis of the system, we assume that field variables such as the velocity or density respect some Fourier solution as sum of several wave modes with respective amplitudes $\tilde{X}_{\omega, k_{\perp}, k_{\parallel}}$:

$$X = \bar{X} + \hat{X} = X_0 + \sum \tilde{X}_{\omega, k_{\perp}, k_{\parallel}} e^{i(-\omega t + k_{\perp} \psi + k_{\parallel} \theta)} \quad (7.8)$$

Electron and ion density are identical because of the quasi-neutrality assumption in [Equation 7.6](#). Since we do not consider any drifts the radial component u_{ψ} of the velocity vector vanishes. Further, the mean density is $\bar{n} = n_0$ while the mean velocity \bar{u}_{θ} is zero. Because we are only interested in a first order approximation of the solution, we neglect all higher-order mixed fluctuating terms. Thus, [Equation 7.5](#) and [Equation 7.7](#) transform to:

$$\begin{aligned} -i\omega \hat{n} + i\bar{n} k_{\parallel} \hat{u}_{\theta} + i\bar{u}_{\theta} k_{\parallel} \hat{n} &= 0 & \Leftrightarrow \hat{u}_{\theta} &= \frac{\omega}{n_0 k_{\parallel}} \hat{n} \\ -i\omega m_i (\bar{n} \hat{u}_{\theta} + \bar{u}_{\theta} \hat{n}) + i m_i k_{\parallel} (2\bar{n} \bar{u}_{\theta} \hat{u}_{\theta} + \bar{u}_{\theta}^2 \hat{n}) &= -2i T k_{\parallel} \hat{n} & \Leftrightarrow \hat{u}_{\theta} &= \frac{2T k_{\parallel}}{m_i n_0 \omega} \hat{n} \end{aligned}$$

Both are combined to obtain a dispersion relation for the frequency ω :

$$\frac{\omega}{n_0 k_{\parallel}} = \frac{2T k_{\parallel}}{m_i n_0 \omega} \quad \Leftrightarrow \quad \omega = \pm \sqrt{\frac{2T}{m}} k_{\parallel} \quad (7.9)$$

It is apparent that both solutions for ω are real therefore non-decaying waves travelling with the speed of sound $c_s = \sqrt{2T/m}$ appear. The perpendicular wave mode does not contribute to the equation so a 1D system along the poloidal axis is sufficient to simulate the behaviour. Both the electron and the ion density are initialized with one sinusoidal perturbation and [Figure 7.3a](#) shows their evolution. The electron velocity in [Figure 7.3b](#) responds to this initial excitation with a shifted standing wave with same frequency.

7. Verification and Validation – 7.2. Linear Analysis

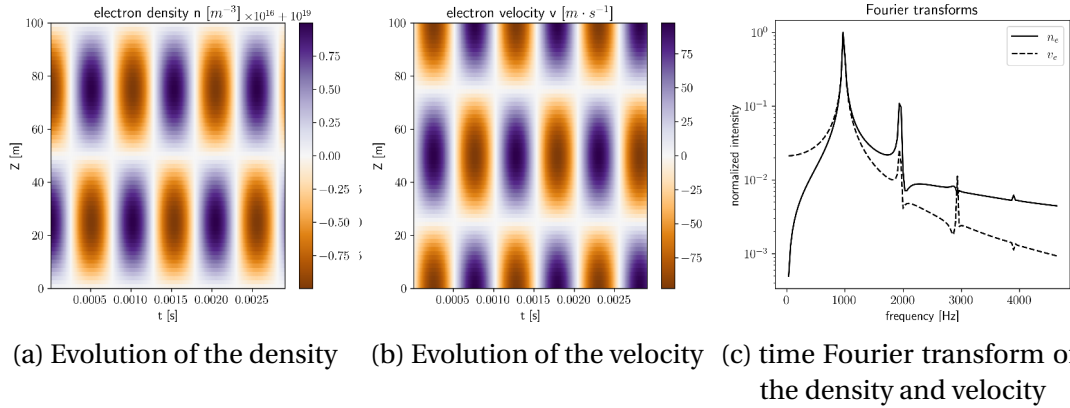


Figure 7.3.: Evolution of the 1D SLAB system with 64 cells in poloidal direction over 10000 timesteps with the RK4 scheme. For a better readability only parts of the graphs are represented

The system is initialized with one wavemode along the "poloidal" length of $L = 100\text{m}$ so the wavenumber here is $k_{\parallel} = 2\pi/L \approx 0.0628$. The plasma temperature is kept constant at $T = 100\text{eV}$ and the mass of a deuterium atom equals to $m_i \approx 3.34 \cdot 10^{-27}\text{kg}$, so we can expect a system frequency of $\omega \approx 978\text{Hz}$ from the dispersion relation in [Equation 7.9](#). This corresponds precisely to the main frequency peak in [Figure 7.3c](#) and thus acoustic waves appear in the system as expected. The smaller peaks at higher frequency modes are however not physical and are likely due to numerical noise as their appearance highly depends on the spatial and temporal resolution and their intensity increases for longer simulations.

7.2.2. Electrostatic case

Before plunging into the vorticity equation with A_{\parallel} it may be interesting to discuss whether the correct behaviour is actually observed in the original electrostatic implementation. For that we reduce the system to the bare minimum set of equations that involve the electric potential Φ . Neglecting all kind of transport equations and source phenomena remains the following simple equation on Φ :

$$\partial_t \nabla \cdot \left[\frac{m_i n_i}{B^2} \nabla_{\perp} \Phi \right] = -\nabla \cdot \sigma_{\parallel} \nabla_{\parallel} \Phi \quad (7.10)$$

whose simple dispersion relation reads, assuming that $k_{\perp} \neq 0$:

$$\omega = -\frac{B^2 \sigma_{\parallel}}{m_i n_i} \frac{k_{\parallel}^2}{k_{\perp}^2} i \quad \Rightarrow \quad \lambda = \frac{B^2 \sigma_{\parallel}}{m_i n_i} \frac{k_{\parallel}^2}{k_{\perp}^2} \quad (7.11)$$

As ω is a pure negative complex number, we do not expect any oscillations but an exponential decay of the solution. All points in the domain decay with

$$\Phi(t) = \Phi_0 e^{-\lambda t} + C \quad (7.12)$$

where the decay rate λ is the negative imaginary part of ω and Φ_0 relates to the initial distribution of the electric potential.

The time integration of this system can only be performed by solving the implicit system because there is no direct expression for the time derivative of Φ . Further, the electric potential Φ appears only in perpendicular and parallel Laplacian operators. Together with the periodic boundary conditions in all directions, one degree of freedom remains and the solution of Φ can only be calculated up to a constant C . To make the system invertible, it is thus necessary to add some term to the system. One simple approach is to fix (or ground) Φ to a set value Φ^G at one point $[i_\psi^G, i_\theta^G]$ in the domain. This defines the free parameter C and $\Phi(t)$ at all points converges to Φ^G .

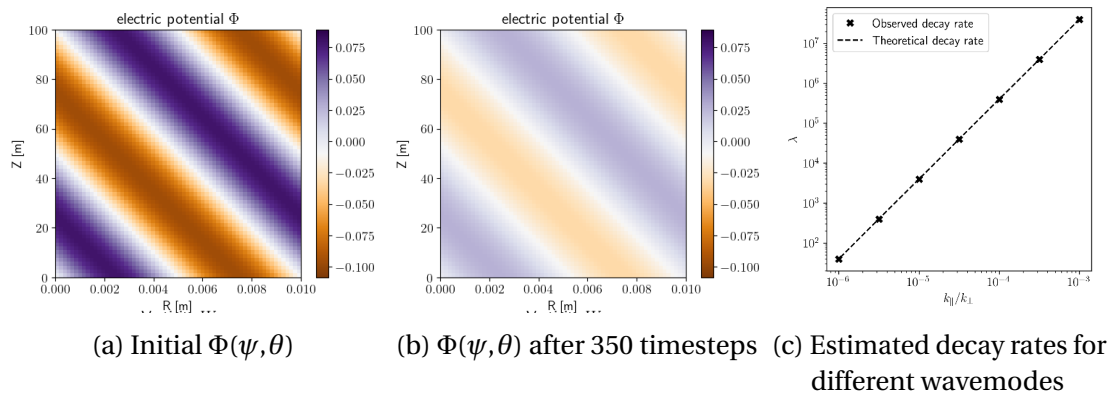


Figure 7.4.: Evolution of the 2D electrostatic SLAB system with 64 cells in radial and poloidal direction over 10000 timesteps with the implicit Euler scheme. The system is grounded at the center of the domain to $\Phi^G = 0V$.

The uniform decay can be clearly seen between Figure 7.4a and Figure 7.4b. It remains to investigate whether the observed attenuation matches the expected decay rate λ . A Fourier transformation as to determine oscillatory modes for the standing acoustic waves in the previous section is not of great help here, instead we use a non-linear least squares to fit the time evolution of $\Phi(t)$ at an arbitrary point in the domain except the grounded point. We fit the parameters Φ_0 , λ and C from Equation 7.12 to the simulation data and compare the hence estimated λ to the theoretical decay rate for the given initial wave. Figure 7.4c shows that there is a strong agreement between the theoretical and fitted decay rates for a large array of domain configurations. The wavenumbers k_{\parallel} and k_{\perp} were modified by changing the poloidal respectively the radial size of the domain with always the first wave mode spanning the entire domain. We can safely claim that the original electrostatic implementation produces the expected physical behaviour.

7.2.3. Electromagnetic case

While acoustic waves are characteristic for a physical medium, Alfvén waves dominate oscillations of ions within a magnetic field. The motion occurs in direction of the

magnetic field lines where the ion mass accounts for the inertia and the magnetic field tension for the restoring wave force. The Alfvén wave group velocity for a species i is given by:

$$v_A = \frac{B}{\sqrt{m_i n_i \mu_0}} \quad (7.13)$$

With the new parallel magnetic vector potential A_{\parallel} into the vorticity ?? Alfvén waves should appear in the simulation and the aim of this section is to prove their existence. We follow the same approach as in the previous section for the electrostatic case and reduce the system to the strict necessary minimum and keep following equations:

$$\partial_t \nabla \cdot \left[\frac{m_i n_i}{B^2} \nabla_{\perp} \Phi \right] = \nabla \cdot \sigma_{\parallel} (-\nabla_{\parallel} \Phi - \partial_t A_{\parallel}) \quad (7.14)$$

$$\Delta_{\perp} A_{\parallel} = -\mu_0 \sigma_{\parallel} (-\nabla_{\parallel} \Phi - \partial_t A_{\parallel}) \quad (7.15)$$

We ignore any kind of advection phenomena thus all densities $n_{i/e}$ and temperatures $T_{i/e}$ keep their initial uniform distributions their gradients vanish. If we perform the linear analysis of the remaining system we get following relation for [Equation 7.14](#):

$$\begin{aligned} i \frac{m_i n_i}{B^2} k_{\perp}^2 \omega \hat{\Phi} &= \sigma_{\parallel} k_{\parallel}^2 \hat{\Phi} - \sigma_{\parallel} k_{\parallel} \omega \hat{A}_{\parallel} \\ \Leftrightarrow \qquad \qquad \qquad \hat{A}_{\parallel} &= \left(\frac{k_{\parallel}}{\omega} - i \frac{m_i n_i k_{\perp}^2}{\sigma_{\parallel} B^2 k_{\parallel}} \right) \hat{\Phi} \end{aligned}$$

and for [Equation 7.15](#):

$$\begin{aligned} -k_{\perp}^2 \hat{A}_{\parallel} &= i \mu_0 \sigma_{\parallel} k_{\parallel} \hat{\Phi} - i \mu_0 \sigma_{\parallel} \omega \hat{A}_{\parallel} \\ \Leftrightarrow \qquad \qquad \qquad \hat{A}_{\parallel} &= \frac{\mu_0 \sigma_{\parallel} k_{\parallel}}{\mu_0 \sigma_{\parallel} \omega + i k_{\perp}^2} \hat{\Phi} \end{aligned}$$

If we combine both expressions we can relate the frequency to the parallel and perpendicular wave modes:

$$\begin{aligned} \frac{k_{\parallel}}{\omega} - i \frac{m_i n_i k_{\perp}^2}{\sigma_{\parallel} B^2 k_{\parallel}} &= \frac{\mu_0 \sigma_{\parallel} k_{\parallel}}{\mu_0 \sigma_{\parallel} \omega + i k_{\perp}^2} \\ \Leftrightarrow \qquad \qquad \qquad i \frac{m_i n_i k_{\perp}^2 \omega}{\sigma_{\parallel} B^2 k_{\parallel}^2} &= 1 - \frac{\mu_0 \sigma_{\parallel} \omega}{\mu_0 \sigma_{\parallel} \omega + i k_{\perp}^2} \\ \Leftrightarrow \qquad \qquad \qquad \omega^2 + i \frac{k_{\perp}^2 \omega}{\mu_0 \sigma_{\parallel}} &= \frac{B^2}{m_i n_i \mu_0} k_{\parallel}^2 \end{aligned}$$

We find the square of the Alfvén group velocity [7.13](#) as a factor before the parallel wave number. There is an additional imaginary term in the dispersion relation which depends on the perpendicular wave number and adds some damping to the system. Let us call $\gamma = 1/(\mu_0 \sigma_{\parallel})$ the associated damping coefficient. The dispersion relation

can then be rewritten to:

$$\omega^2 + i\gamma k_{\perp}^2 \omega - v_A^2 k_{\parallel}^2 = 0 \quad (7.16)$$

If we transform the system back to the time domain, we expect a damped solution for the potentials Φ and A_{\parallel} of the form [12]:

$$X = X_0 + \hat{X} e^{-\lambda t} e^{i(-\omega_0 t + k_{\perp} \psi + k_{\parallel} \theta)} \quad (7.17)$$

where the decay rate λ contains the imaginary part and the oscillation frequency ω_0 the real part of ω .

In the case that $\gamma k_{\perp}^2 > 2v_A k_{\parallel}$, the frequency ω is purely imaginary and the system decays to the mean value X_0 with the rate:

$$\lambda = \frac{\gamma}{2} k_{\perp}^2 \pm \sqrt{\frac{\gamma^2}{4} k_{\perp}^4 - v_A^2 k_{\parallel}^2} \quad (7.18)$$

If on the other hand $\gamma k_{\perp}^2 < 2v_A k_{\parallel}$, the frequency ω has both a real and an imaginary part. The decay rate is then:

$$\lambda = \frac{\gamma}{2} k_{\perp}^2 \quad (7.19)$$

and the system frequency:

$$\omega_0 = \pm \sqrt{v_A^2 k_{\parallel}^2 - \frac{\gamma^2}{4} k_{\perp}^4} \quad (7.20)$$

In the case that the damping term is much smaller than the oscillatory term (if for instance the parallel wave mode dominates over the perpendicular one), ω is a real number and the system frequency only depends on the Alfvén group velocity and we should be able to observe pure Alfvén waves.

$$\omega_0 = v_A k_{\parallel}$$

In [Equation 7.18](#) and [Equation 7.20](#) we see that there are two possible solution for the decay rate respectively the oscillation frequency. This does not conflict with our assumed wave solution which has been defined in [Equation 7.8](#) as the sum of several Fourier modes and each solution here contributes to one mode.

As in the electrostatic case from the previous section, the just described system is not invertible and Φ is defined up to a constant. Grounding the potential in one single point is however not a suitable solution here because it deteriorates the condition number of the vorticity matrix past solvability. Instead two other approaches will be followed to check if simulations can reproduce the expected physical behaviour.

7.2.3.1. Grounded line

One approach is to set the potential not in one but in several points to a fixed value. The potential in the remaining domain then distributes according to this value and the whole system becomes solvable. Numerically, this is achieved by replacing the row of the matrix corresponding to the grounded point by a single 1 on the diagonal and the matching term in the RHS vector by the desired value for Φ . This operation is equal to enforcing Dirichlet boundary conditions in radial direction if Φ is grounded at all points with index i_ψ^G .

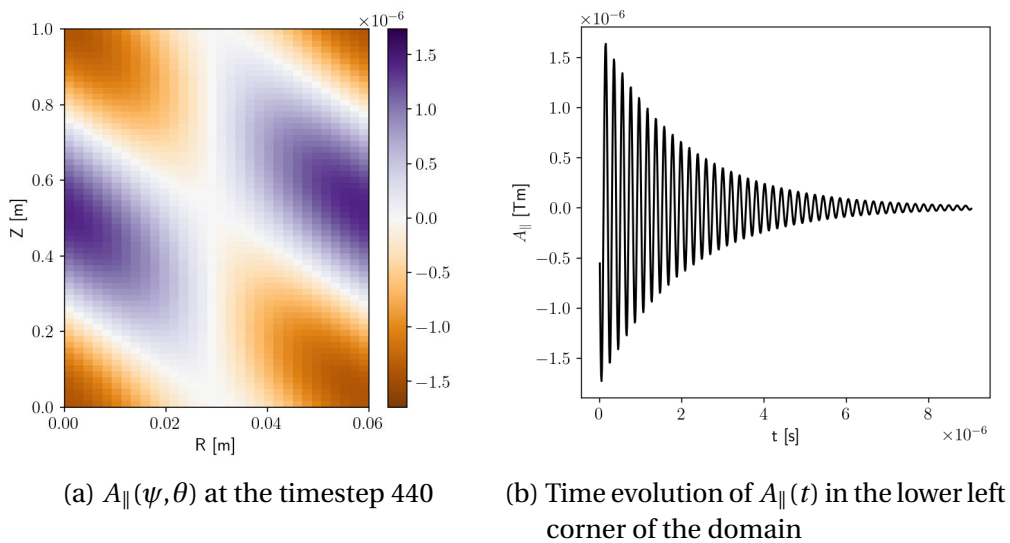


Figure 7.5.: Snapshot of an electromagnetic SLAB simulation on a domain with $N_\psi = 32$ and $N_\theta = 64$ grid points. All point at the radial center with i_ψ^G are grounded.

In the simulations with a grounded line, the initial wave solution has been applied to the vorticity field Ω to prevent steep gradients and instabilities if it was done on Φ directly. Very soon, the two potentials Φ and A_{\parallel} respond to this initial excitation and a wave profile appears as depicted in Figure 7.5a. The line of grounded points in the middle of the domain however breaks the wave which then smoothly lines up with the equilibrium point $\Phi_0 = 0V$ and $A_{\parallel,0} = 0Tm$ around the grounded line. At this point it may be emphasized that only the electric potential Φ is grounded, but as both potential fields are strongly coupled the grounded line affects A_{\parallel} equally. We thus have a wave that is guided between two poloidal grounded lines (remember that the domain is periodic in radial direction) so by construction the system cannot account for radial dynamics. If we consider a point that is furthest away from the grounded line (e.g. any point on the domain boundary in the example above) we might still be able to observe some expected physical behaviour. At first glance, if we track A_{\parallel} in one point over time as in Figure 7.5b, a decaying oscillation appears which is in line with the here dominant underdamped regime.

First we investigate the underdamped scenario by opposing simulation results to the expected damping rates λ and frequencies ω_0 . As for the previous electromagnetic we fit the four free parameters in [Equation 7.17](#) to simulation data with a nonlinear least squares method. With 1000 sample points we get a high fitting fidelity with a relative standard deviation of the order of 10^{-9} and the difference if the fit is performed on Φ or A_{\parallel} has about the same magnitude.

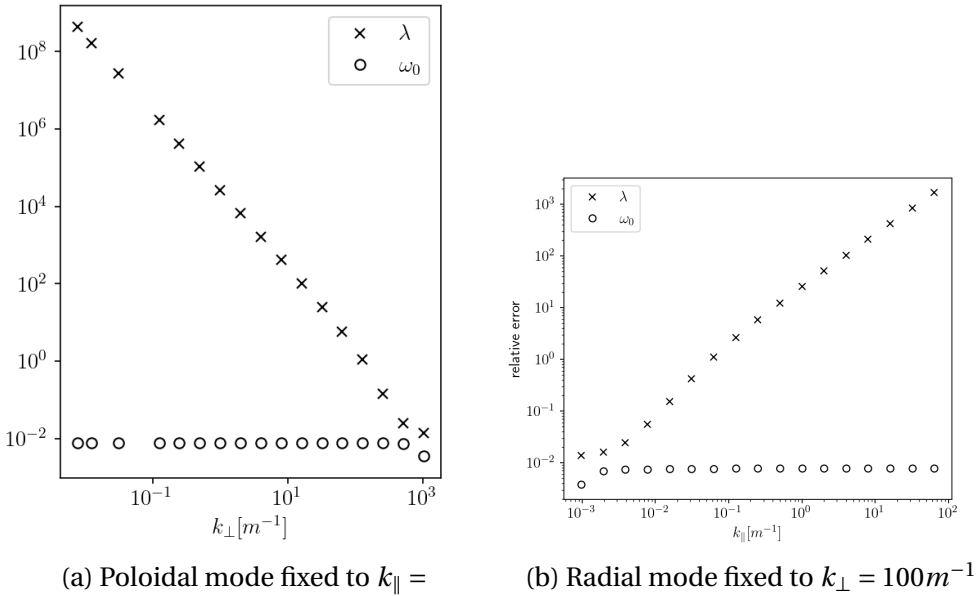


Figure 7.6.: Relative error for the fits of the frequency ω_0 and the decay rate λ on the evolution of A_{\parallel} with respect to the expected values in a grounded electromagnetic SLAB simulation on a domain with $N_{\psi} = 32$ and $N_{\theta} = 64$ grid points.

7.2.4. Linear transition from Alfvén to thermal electron waves

In Sec. 4.4, we introduced drift-Alfvén waves. With the electromagnetic extensions, drift-waves are coupled to higher-frequency modes that transition from the Alfvén to the thermal electron speed and travel along magnetic field lines. These modes are associated with negative growth rate and usually dampen out quite fast. They can however be used to validate the electromagnetic implementation. The thought behind it is that if we reduce the system to suppress drift-waves, and run simulations with a sufficiently temporal resolution, the transition should appear in the SOLEDGE3X simulations.

The following simplified model (Eq. 7.21) is considered on the electron density n_e , parallel current j_{\parallel} , and the potentials Φ and A_{\parallel} :

$$\left\{ \begin{array}{l} \partial_t n_e = \frac{1}{e} \nabla \cdot (j_{\parallel} \mathbf{b}) \\ j_{\parallel} + \frac{\sigma_{\parallel} m_e}{n_e e^2} \partial_t j_{\parallel} = \sigma_{\parallel} \left(-\nabla_{\parallel} \Phi - \partial_t A_{\parallel} + \frac{T_e}{e} \nabla_{\parallel} \log(n_e) \right) \\ \nabla \cdot \left[\frac{m_i n_i}{B^2} \partial_t \nabla_{\perp} \Phi \right] = \nabla \cdot (j_{\parallel} \mathbf{b}) \\ \Delta_{\perp} A_{\parallel} = -\mu_0 j_{\parallel} \end{array} \right. \quad (7.21)$$

The computational domain is a 3D slab domain with periodic boundary conditions in all directions. The magnetic field is assumed to be constant in the $\theta - \varphi$ plane. The wavenumbers k_{ψ} , k_{θ} , and k_{φ} are defined by the respective dimensions of the slab. Parallel and perpendicular wavenumbers express as:

$$k_{\parallel} = b_{\theta} k_{\theta} + b_{\varphi} k_{\varphi} \quad k_{\perp} = \sqrt{k_{\psi}^2 + k_{\theta}^2 + k_{\varphi}^2 - k_{\parallel}^2} \quad (7.22)$$

The Alfvén wave speed is given by $v_A = \frac{B_0}{\sqrt{m_u n_e \mu_0}}$ and the electron thermal speed by $v_{th,e} = \sqrt{\frac{e T_e}{m_e}}$. In the zero-resistivity limit, the dispersion relation states that we deal with a complex wave frequency, whose real component is:

$$\omega_0^2 = \frac{v_A^2}{1 + \frac{m_e}{e^2 \mu_0 n_e} k_{\perp}^2} k_{\parallel}^2 + \frac{1}{\frac{n_e \mu_0}{T_0 k_{\perp}^2} + \frac{1}{v_{th,e}^2}} k_{\parallel}^2 \quad (7.23)$$

From Eq. 7.23, we expect a wave in the parallel direction traveling at the Alfvén velocity for small k_{\perp} and at the thermal electron velocity at high k_{\perp} . In the slab domain, k_{\perp} is changed by changing the radial dimension of the domain. The results of our numerical simulations perfectly match the predictions by Dudson [21] and the numerical results obtained by Stegmeir *et al.* [74] and show the expected transition when k_{\perp} is varied, Fig. 7.7.

!!!! ALERNATIVE TEXT !!!!!!! Density perturbations provoke an electromagnetic response. To this effect, we consider a standard four-field model that couples the electron density n_e with the parallel current density j_{\parallel} and both potentials Φ and A_{\parallel} . The governing equations now are:

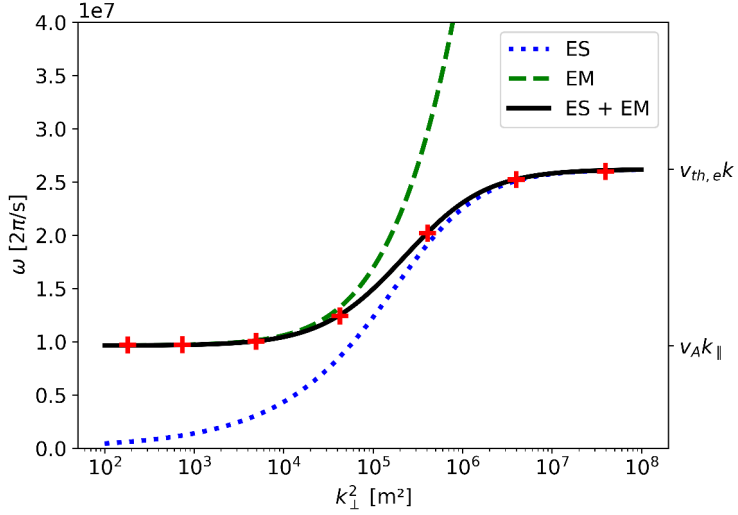


Figure 7.7.: Fitted wave frequencies as a function of the perpendicular wave numbers. The lines indicate the theoretical wave frequencies in the electrostatic case with finite electron mass (ES), the electromagnetic case with $m_e = 0$ (EM), and the complete electromagnetic case with electron inertia (ES + EM).

$$\nabla \cdot \left[\frac{m_i n_i}{B^2} \partial_t \nabla_{\perp}^2 \Phi \right] = \nabla \cdot (j_{\parallel} \mathbf{b}) \quad (7.24)$$

$$\nabla_{\perp}^2 A_{\parallel} = -\mu_0 j_{\parallel} \quad (7.25)$$

$$\eta_{\parallel} j_{\parallel} + \frac{m_e}{n_e e^2} \partial_t j_{\parallel} = (-\nabla_{\parallel} \Phi - \partial_t A_{\parallel} + T_e \nabla_{\parallel} \log(n_e)) \quad (7.26)$$

$$\partial_t n_e = \frac{1}{e} \nabla \cdot (j_{\parallel} \mathbf{b}) \quad (7.27)$$

Its complex dispersion relation has a real and an imaginary part indicating the appearance of a decaying wave.

$$\omega_A^2 = \left(\frac{v_A^2}{1 + \frac{m_e}{e^2 \mu_0 n_e} k_{\perp}^2} + \frac{1}{\frac{n_e \mu_0}{T_0} + \frac{1}{v_{th,e}^2}} \right) k_{\parallel}^2 - \frac{\eta_{\parallel}^2 k_{\perp}^4}{4 \left(\mu_0 + \frac{m_e}{e^2 n_i} k_{\perp}^2 \right)^2} \quad (7.28)$$

The dispersion relation describes "shear Alfvén waves", according to which perturbations travel along magnetic field lines. In cases with high parallel conductivity, the first term dominates the dispersion relation. We then observe that the relation describes a wave in parallel direction whose velocity is bound by the Alfvén wave speed $v_A = \frac{B}{\sqrt{m_i n_i \mu_0}}$ for small k_{\perp} and by the thermal electron wave speed $v_{th,e} = \sqrt{\frac{T_e}{m_e}}$ for large k_{\perp} . This is in line with the findings by Dudson et al [21] and reflects the need for electron inertia to avoid unphysically large speeds in the upper k_{\perp} limit.

Part III.

Impact of Electromagnetic Effects on Plasma Simulations

8. Electromagnetic simulations on analytic geometries

8.1. Slab configurations

8.1.1. Analysis of a plasma blob

The linear analysis from the previous section has only , as characteristic shear Alfvén and thermal electron times are much shorter than the ion cyclotronic time, which underlies the resolution of typical turbulent SOLEDGE3X simulations. Drift Alfvén waves in turn correspond to the impact of inductive electromagnetic effect on the formation of drift waves, where the term $\partial_t A_\parallel$ in Ohm's law (Eq. ??) modifies the non-adiabatic response of the potential Φ to parallel fluctuations of the electron pressure p_e . To study the these effects on a plasma blob in a slab domain.

We place ourselves in a plasma environment similar to the separatrix region in the diverted TCV simulations from the next Sec. ???. The magnetic field is aligned to the toroidal coordinate with $B_{eq,t} = 1.3\text{T}$ with a curvature of 1.1m from the tokamak center, similar to the position of the separatrix at the outer mid-plane in TCV. Limiters are placed at both toroidal ends such that that connection length $L_\varphi = 65\text{m}$. A cartesian grid with coordinates r and z discretizes each poloidal plane, allowing radial fluxes out and with periodic boundary conditions in the vertical z -direction. The electron temperature is kept constant at $T_e = 60\text{eV}$, ions are cold and the background density is set to $n_0 = 10^{19}\text{part/m}^3$. To simplify the study and prevent numerical difficulties at the sheath, we apply Neumann-0 boundary $\partial_\parallel n^{BC} = 0$ on the density and the potential Φ is fixed to $\Phi^{BC} = \Lambda T_e^{BC}$. This is a major simplification to the typical SOLEDGE3X sheath conditions described in Sec. ???. The axisymmetric blob initially takes a Gaussian profile

$$n = n_0 \left(1 + \alpha e^{-[(r-r_b)^2 + (z-z_b)^2]/\delta_b}\right) \quad (8.1)$$

with a blob overdensity $\alpha = 2$ and radius $\delta_b = 1\text{cm}$. The blob evolves with curvature and electric drifts, neglecting anomalous perpendicular diffusion and viscous effects. Further, electron inertia effect are neglected with $m_e = 0$. We compare the reference electrostatic case with magnetic induction in the parallel electric field and the full electromagnetic setting including flutter. The simulation results are collected in Fig. 8.1.

8. Electromagnetic simulations on analytic geometries – 8.1. Slab configurations

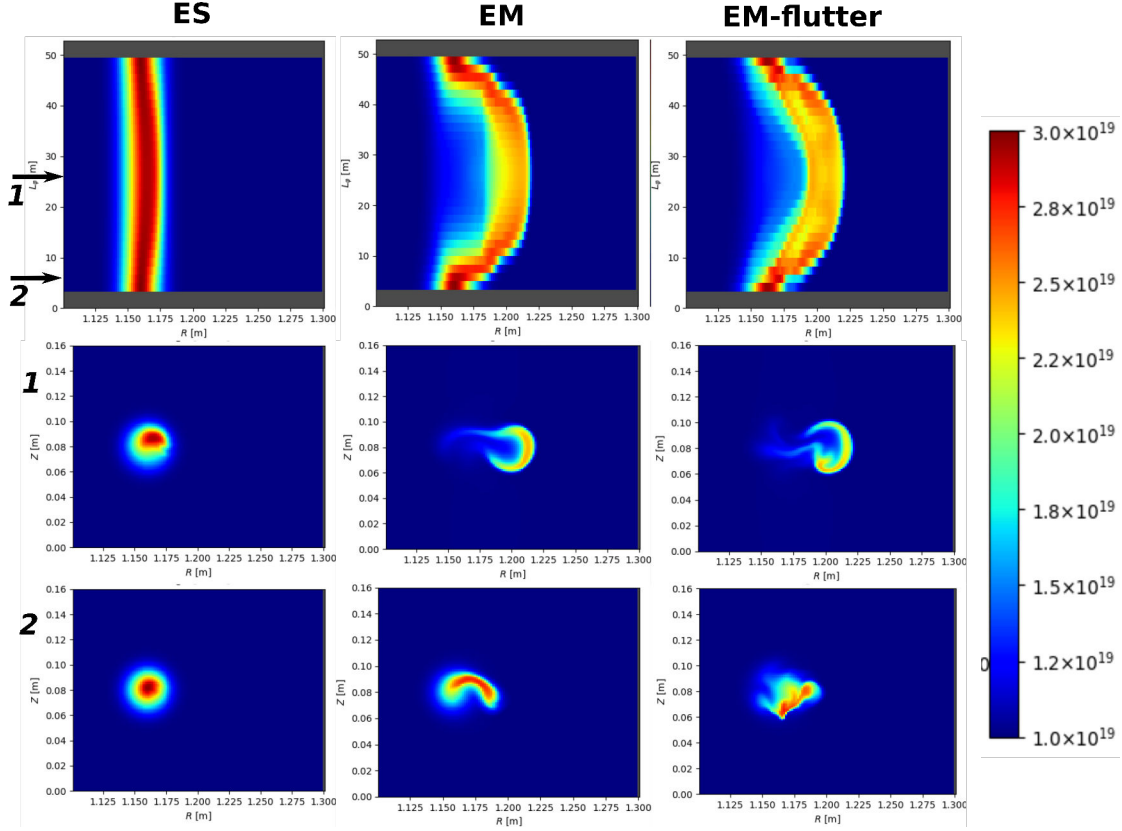


Figure 8.1.: Density profiles [part/m^3] after $9.6\mu\text{s}$ simulated plasma time for the electrostatic (ES), magnetic inductive (EM) and full electromagnetic scenarios (EM-flutter). The first row shows a view of the $R - \varphi$ plane with the maximum density taken along the Z coordinate. The second and third rows show the density on poloidal planes ($R - Z$) at the center of the field lines (1) and in proximity to the sheath (2).

In the center of the domain, drift waves determine the potential Φ but it is dominated by the sheath in proximity to the limiters. Hence a parallel gradient appears on Φ , which in turn induces a parallel current responsive to inductive electromagnetic effects. As a result, the blob filaments bends along the toroidal direction, with higher advection velocities in the center of the domain than at the sheath. The bending is much more pronounced for the two electromagnetic scenarios, in line with the findings of previous blob studies[48, 49, 75]. On closed field lines, the blob would conserve its axisymmetry and both j_{\parallel} and A_{\parallel} would remain 0 throughout the simulation.

8.1.2. Generation of drift waves

In the previous section, we examined how a single plasma blob propagates across open field lines. However, this does not account for how the blob appears in the first place. In this second part of the slab study, we investigate the onset of drift waves.

8. Electromagnetic simulations on analytic geometries – 8.1. Slab configurations

We consider the same setting as before but with a background density of $n_0 = 2 \cdot 10^{19}$ part/m³ and isothermal electrons and ions at $T_e = T_i = 50$ eV. Instead of an initial overdensity, we apply a constant particle source of $5 \cdot 10^{22}$ part/s on the core side, at all $R < 1.12$ m. The emergence of drift-wave instabilities for the three scenarios is shown in Fig. 8.2.

Initially, the particle source causes the density to build up on the core side of the slab. The radial gradient becomes stronger and soon collapses into drift waves. These waves are particularly pronounced in the electrostatic and electromagnetic inductive models. The term $\partial_t A_{\parallel}$ in Ohm's law intensifies the turbulent interchange, with plasma filaments reaching much further outward. On the other hand, the electromagnetic model with flutter has a stabilizing effect, producing only a thin turbulent layer at the exit of the source and maintaining a strong gradient at the transition from high-to low-density regions. As more particles are introduced at the source, the pressure differential causes this transition line to bend at scales of the simulation box, while the local gradient remains very steep.

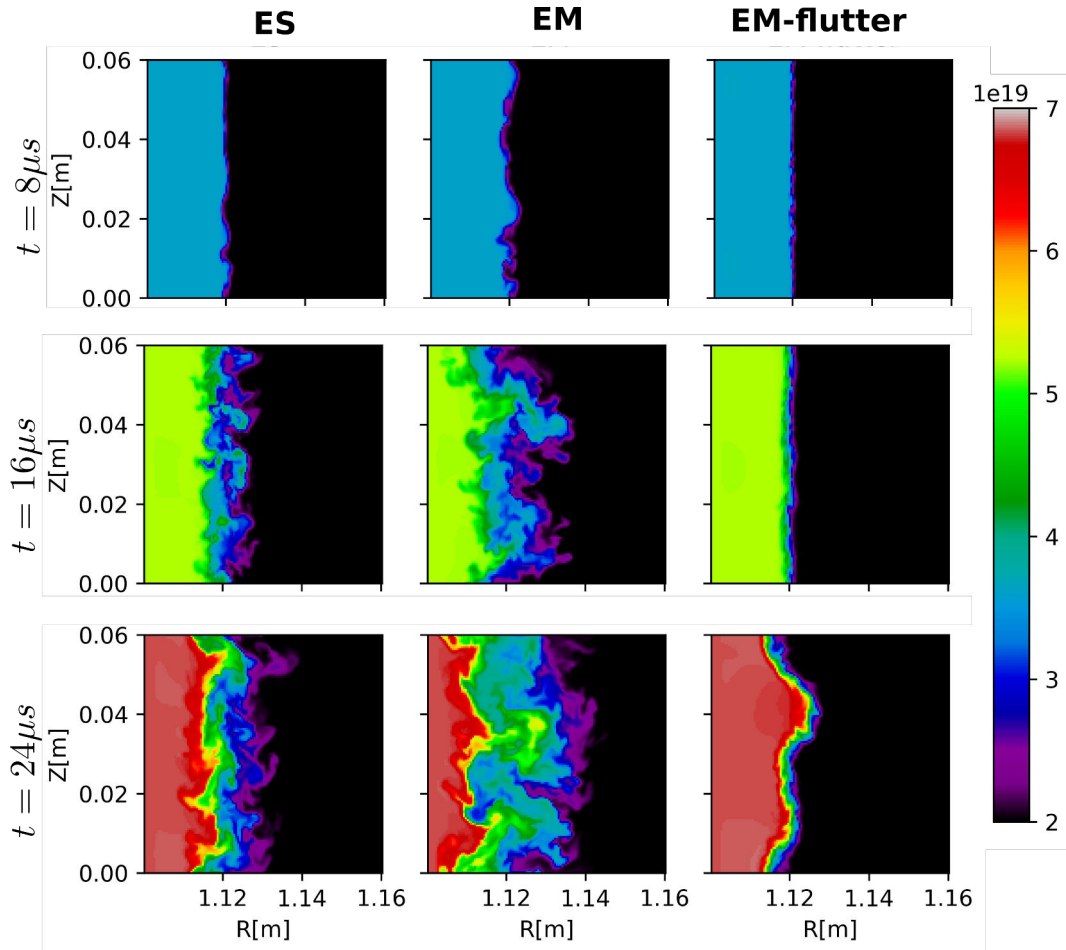


Figure 8.2.: Density profiles [part/m³] at the toroidal center of the slab, at about 32m from both limiters. The snapshots compare the electrostatic (ES), magnetic inductive (EM) and full electromagnetic scenarios (EM-flutter) scenarios after 8, 16 and 24 μs simulated plasma time.

8.2. Circular geometry

8.2.1. Simulation set-up

Flat limiter on the low-field side

8. Electromagnetic simulations on analytic geometries – 8.2. Circular geometry

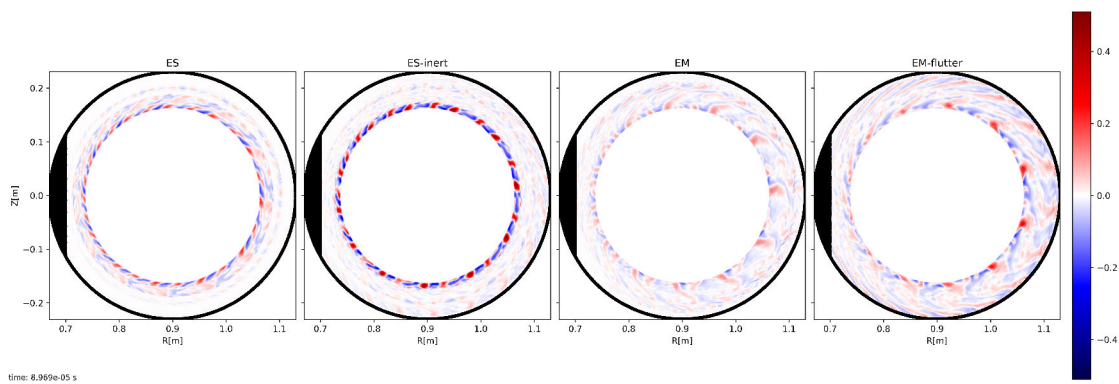


Figure 8.3.: Snapshots of the electron temperature T_e fluctuations

8.2.2. Growth rates

8.2.2.1. Electron inertia

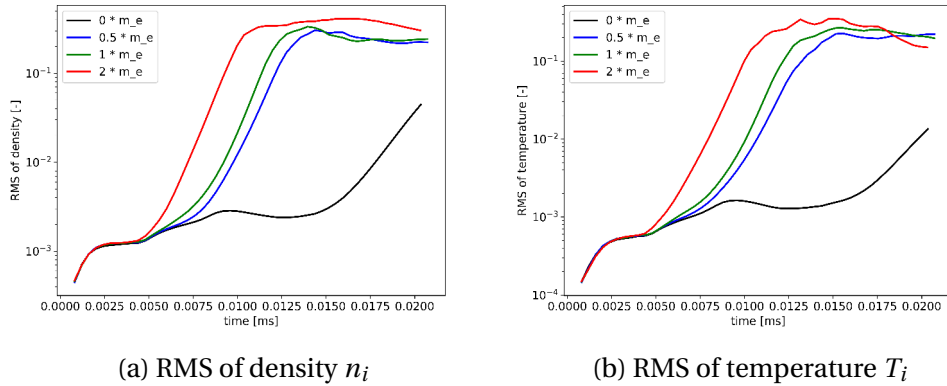


Figure 8.4.: Evolution of the perturbation intensity for different values of m_e . The electron mass is artificially increased and the 0 factor corresponds effectively to the electrostatic reference

8.2.2.2. Magnetic induction

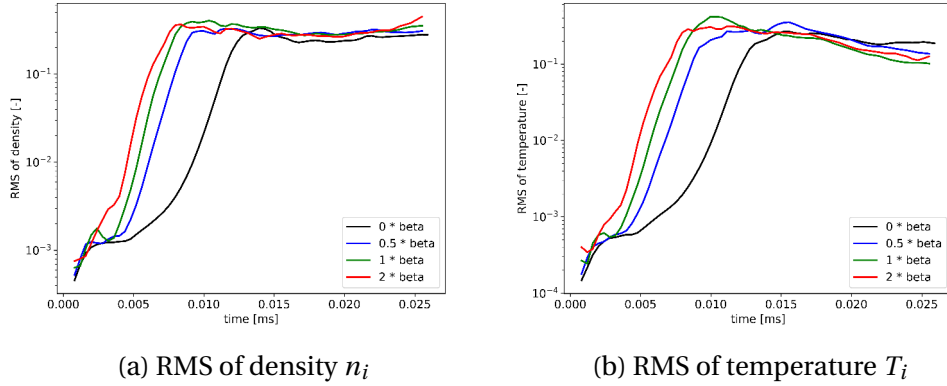


Figure 8.5.: Evolution of the the perturbation intensity for different values of β . The is artificially increased and the 0 factor corresponds effectively to the electrostatic with electron inerita. The electron mass for all scenarios is physical (factor 1 in Fig. 8.4).

8.2.3. Stabilization by flutter

9. Electromagnetic simulations on a realistic diverted geometry

To demonstrate the abilities of SOLEDGE3X to perform electromagnetic turbulence simulations of a realistic tokamak geometry, the configuration of the test cases has been inspired by the TCV-X21 benchmark [56]. This latter addresses L-mode discharges in TCV with a single lower X-point.

9.1. Electrostatic versus electromagnetic scenarios

The semi-implicit time discretization implemented in this model allows comparisons to be made between the electrostatic and electromagnetic models using the same code. Four cases have therefore been considered here: electrostatic (ES), electrostatic with electron inertia (ES-inert), electromagnetic (EM), and electromagnetic with flutter (EM-flutter).

9.1.1. Simulation set-up

The plasma is pure deuterium, and only a quarter-torus with a relatively low resolution of approximately 1.9 million cells has been considered to speed up computations (see the mesh in a poloidal plane in Fig. 6.1a). A constant heat source of 25 kW is applied to both electrons and ions, equating to a full-torus equivalent total Ohmic heating of 200 kW. The external toroidal magnetic field is $B_t = 0.95$ T, and the density at the separatrix is targeted to $7 \cdot 10^{18}$ part/m³.

Since the aim of these preliminary computations was to focus on electromagnetic effects, neutrals have been omitted to speed up the convergence of the solutions. Simulations with a more complete physical model will be performed in a further work, including in particular the latest fluid neutral model [58] developed for regimes dominated by charge exchanges [40].

In all cases, the initial condition is the corresponding 2D transport solution obtained by increased perpendicular diffusion coefficients.

In Fig. 9.1, typical poloidal cuts of important plasma fields are shown. The local value of β varies between 10^{-3} at the hot core boundary, 10^{-4} around the separatrix

9. Electromagnetic simulations on a realistic diverted geometry – 9.1. Electrostatic versus electromagnetic scenarios

and divertor region, and 10^{-5} or lower in the far SOL. Consequently, the flutter perturbation \tilde{B} of the magnetic field remains small compared to the equilibrium field, barely exceeding 0.1% of B_t on the hot core side of the domain. The advection velocity associated with the flutter is also minimal, contributing to less than 0.1% of the cross-field transport, dominated by the electric "ExB" drift.

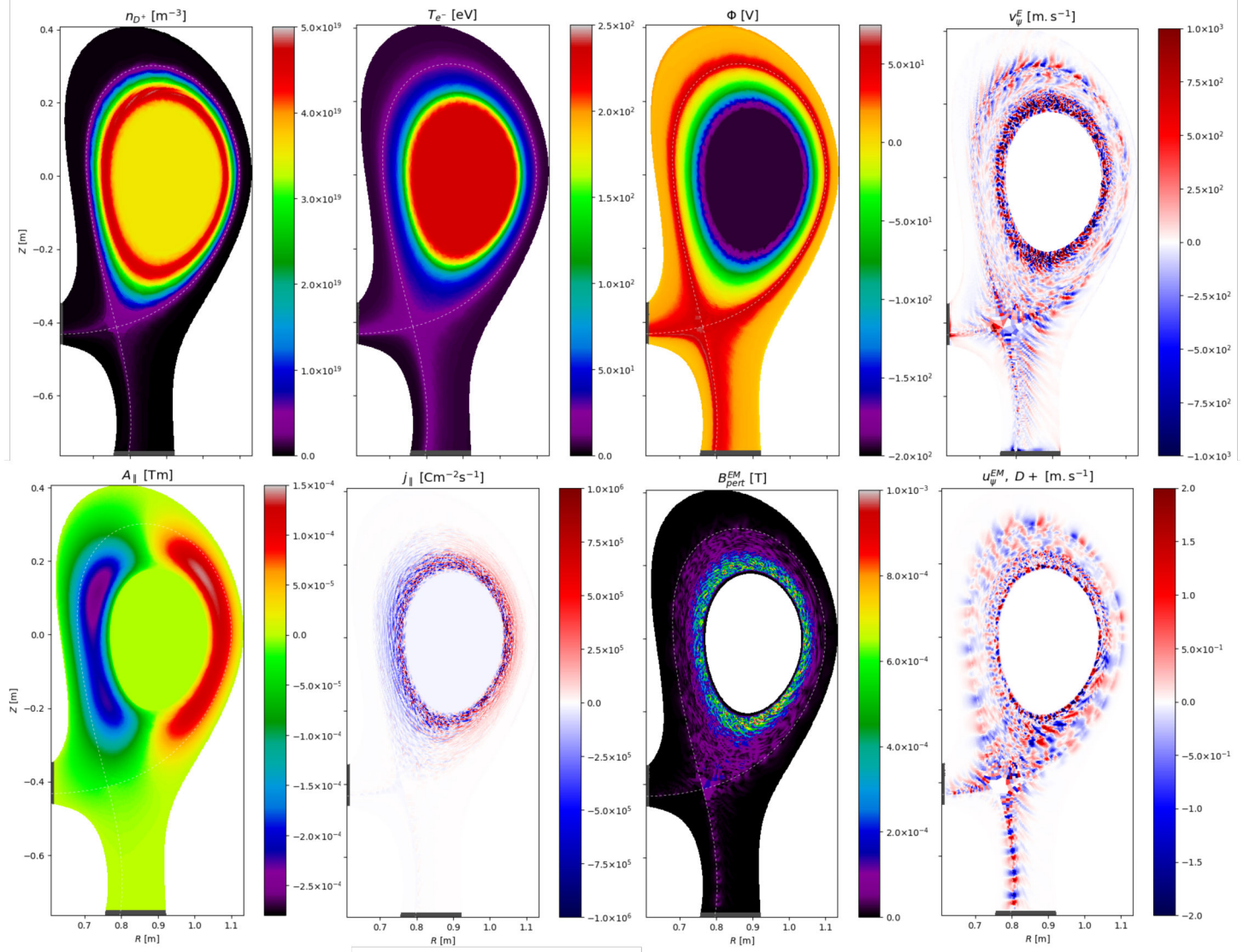


Figure 9.1.: Simulation snapshots of the full electromagnetic scenario with flutter. The first poloidal plane is shown after 6 ms simulated plasma time on the TCV case. From left to right, the first row shows the ion density n_i , the electron temperature T_e , the electric potential Φ , and the radial "ExB" drift velocity v_E^ψ . The second row shows the parallel magnetic potential A_\parallel , the parallel current density j_\parallel , the amplitude of the flutter field $\|\tilde{\mathbf{B}}\|$, and the radial flutter advection velocity $v_{\tilde{B}\psi}$.

9.1.2. Comparison between the scenarios

We now compare the impact of the different levels of new physics on the TCV scenario. Since turbulent structures are essentially driven by the electric "ExB" drift, we consider the associated total kinetic energy $E_{ExB} = \frac{1}{2} m_i \int_V n_i \|v_E\|^2 dV$ to estimate the turbulence level. As shown in Fig. 9.2a, a finite electron mass does not change the energy level with respect to the reference electrostatic scenario. Next, adding magnetic induction with A_\parallel further amplifies the turbulent interchange. This enhancement arises from the increased coupling between the magnetic and electric fields, leading to more instabilities and modified turbulent dynamics. Consequently, turbulent filaments give way to smaller, rounder blobs. Finally, the inclusion of flutter has a stabilizing effect on the turbulence, where fluctuations fall again to the level in the electrostatic case. Nonlinear effects in the parallel current equation, namely from the parallel pressure gradient $\nabla_\parallel p_e$, substantially impact the profiles of j_\parallel and hence the response of the potential Φ . The direct consequence is a modification of the radial electric field and a modified evolution of "ExB" drifts. This does not contradict our previous observation that magnetic advection is negligible with respect to the electric drift.

With a different turbulence level, the heat exhaust is also affected, as shown in Fig. 9.2b. Without radiative effects, the quasi-totality of the heat leaves the tokamak at two divertor targets. The supplementary radial turbulent transport in the magnetic inductive scenario allows more hot particles to cross the separatrix from the core, which will then eventually reach the divertor. Overall, the heat flux is multiplied by a factor of 10. Electron inertia alone leads to an increase by a factor of 2, despite very similar turbulence levels. This phenomenon needs further investigation. Flutter does not reduce further the heat exhaust as one might expect because it is already very low in the electrostatic case.

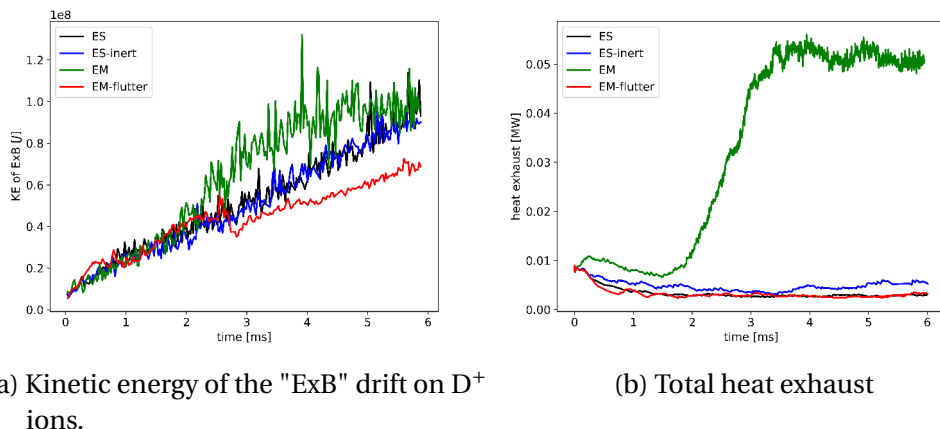


Figure 9.2.: Evolution of the kinetic energy and heat exhaust over time iterations on the turbulent TCV scenario. It indicates the turbulence level and its consequence on the total heat transport.

The change in turbulence intensity naturally impacts the mean profiles in Fig. 9.3. The most noticeable change affects the electromagnetic inductive scenario, where density and temperature gradients are considerably reduced by the additional radial turbulent transport. Again, the finite electron mass has no significant impact, and the reduced turbulence levels by flutter lead to steeper gradients. At this point, we stress the similarity to the simplified drift wave simulations on slab in Sec. 8.1.2, where the gradients from the dense core follow the same pattern.

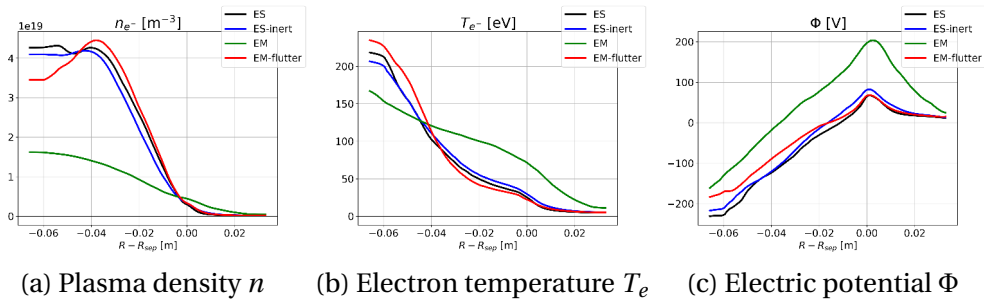


Figure 9.3.: Radial profiles at the outer mid-plane after 6 ms simulated plasma time.

These profiles were obtained by averaging simulation data across all 32 toroidal planes and over the last 20 available plasma saves.

9.1.3. Numerical performances

In our previous work [5, 76] about the electrostatic model, it was pointed out that solving the implicit 3D vorticity operator is the most expensive and tricky operation in the algorithm. Adding new variables inevitably modifies the code's performance. With the rather coarse mesh used in the present work, simulations have been run on 16 nodes with 48 CPUs each on the MARCONI supercomputer operated by CINECA [42]. Implicit systems, such as the 3D vorticity operator, have been inverted using the stabilized biconjugate gradient method (BCGS) [81] with the generalized algebraic multigrid preconditioner (GAMG) by PETSc [1].

The overall performance of the code largely depends on how quickly a certain plasma timespan can be calculated. Table 9.1 presents the average simulation time for one timestep, broken down by the cost of each implicit solver. For the vorticity system, we also provide the number of iterations the BCGS needed to match the imposed tolerance (10^{-8}), as it relates to the condition number of the matrix. This system has always accounted for a considerable share of the total execution time and was heavily modified with the new electromagnetic model. Finally, the timestep size is provided, as a higher timestep size can compensate a costlier problem because the desired simulation time is reached in fewer iterations. As described earlier in Sec. ??, SOLEDGE3X uses a variable timestep scheme to maximize the CFL condition with the calculated fluxes.

	Total execution time per timestep [ms]	Execution time for the viscosity [ms]	Execution time for the heat diffusion [ms]	Execution time for the vorticity [ms]	N° of vorticity solver iterations	Timestep size [ns]
ES	664	61	76	339	80	15.6
ES-inert	523	61	77	193	32	16.4
EM	895	63	82	552	60	15.9
EM-flutter	2019	225	390	1147	55	16.6

Table 9.1.: Numerical metrics on the four TCV scenarios for one timestep. All quantities are averaged over the last 20000 timesteps of the simulation. The execution time refers to the wall-clock time and must be multiplied by the number of used processors (768) to get the actual used CPU time.

The introduction of a finite electron mass to the vorticity system significantly reduces the number of solver iterations and allows to reach a solution much faster. This improvement occurs because electron inertia effects dominate Ohm's law, thereby reducing the anisotropy between the perpendicular and parallel Laplacians on Φ in the electrostatic scenario. This reduction in anisotropy is due to the parallel diffusion coefficient being the conductivity σ_{\parallel} in the electrostatic case, but a finite electron mass m_e imposes an upper limit on it. Adding A_{\parallel} doubles the size of the matrix and introduces a more complex structure, challenging the solvers and requiring more iterations. Despite the higher complexity, a finite electron mass allows the solver to converge in fewer iterations than in the reference electrostatic case. However, the effective solve time is still worse due to the doubling in system size. Finally, including flutter slightly improves the matrix condition compared to the scenario with only magnetic induction, but the execution time is significantly increased. At first glance, one would expect the solve time to correlate with the number of BCGS iterations as both electromagnetic scenarios solve a coupled 3D system on Φ and A_{\parallel} . Since flutter introduces the radial direction to parallel gradients, and the coupling terms between the two unknowns are exactly a parallel gradient and a divergence (see Eq. ??), the matrix exhibits a decreased sparsity ratio. This circumstance is further aggravated by the fact that A_{\parallel} is not staggered in the radial direction, so the radial discrete gradient/divergence operator has a larger stencil width than its poloidal and toroidal counterparts.

The viscosity and heat diffusion solvers are not directly affected by the electromagnetic model, and their solve times are similar for the first three scenarios. Electromagnetic flutter, however, with its radial gradient (again), heavily modifies the parallel diffusion operators and requires solving one global 3D system instead of separate 2D systems on each flux surface (see Sec. 6.3.3.2). This is immediately reflected in the

code performance, as both solvers take up to 5 times longer to solve.

In total, electron inertia decreases the computing time with an excellent improvement of the vorticity matrix condition. The magnetic inductive model means slightly higher computational costs, because the implicit vorticity problem doubles in size. Including electromagnetic flutter in the system almost quadruples the execution time compared to the original implementation because the radial parallel gradient complicates both the implicit vorticity and the parallel diffusion problem. The timestep size does not vary considerably between the scenarios and hence has only a limited impact on the overall performance.

9.1.4. Comparison to the TCV-X21 reference simulations

?????

9.2. Electromagnetic power scan

Full model, with electron inertia, magnetic induction and flutter.

Increase input power of the Ohmic heating in the TCV scenarios. Density is controlled by Horsten neutral model.

9.2.1. Qualitative evolution of the simulation

First phase the plasma heats up. As it reaches a quasi-steady state (surge in output heat fluxes to compensate the core source), Increase in turbulent transport across separatrix. But importantly: strong increase of the radial flutter flux.

9.2.2. Mid-plane profiles

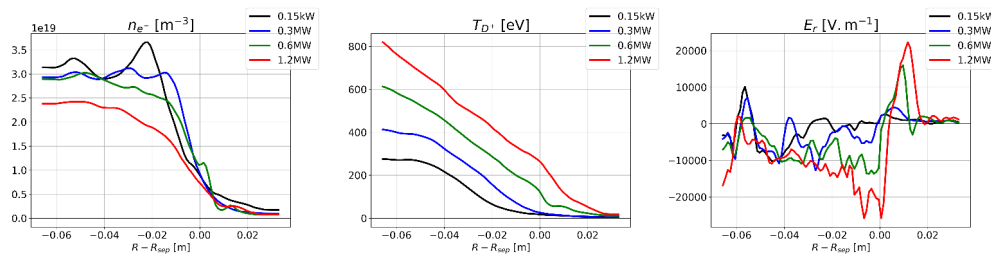


Figure 9.4.: Radial profiles at the outer mid-plane after 4ms.

Formation of a pedestal ?

9.2.3. Flutter in the high-power cases

Poincaré plots:

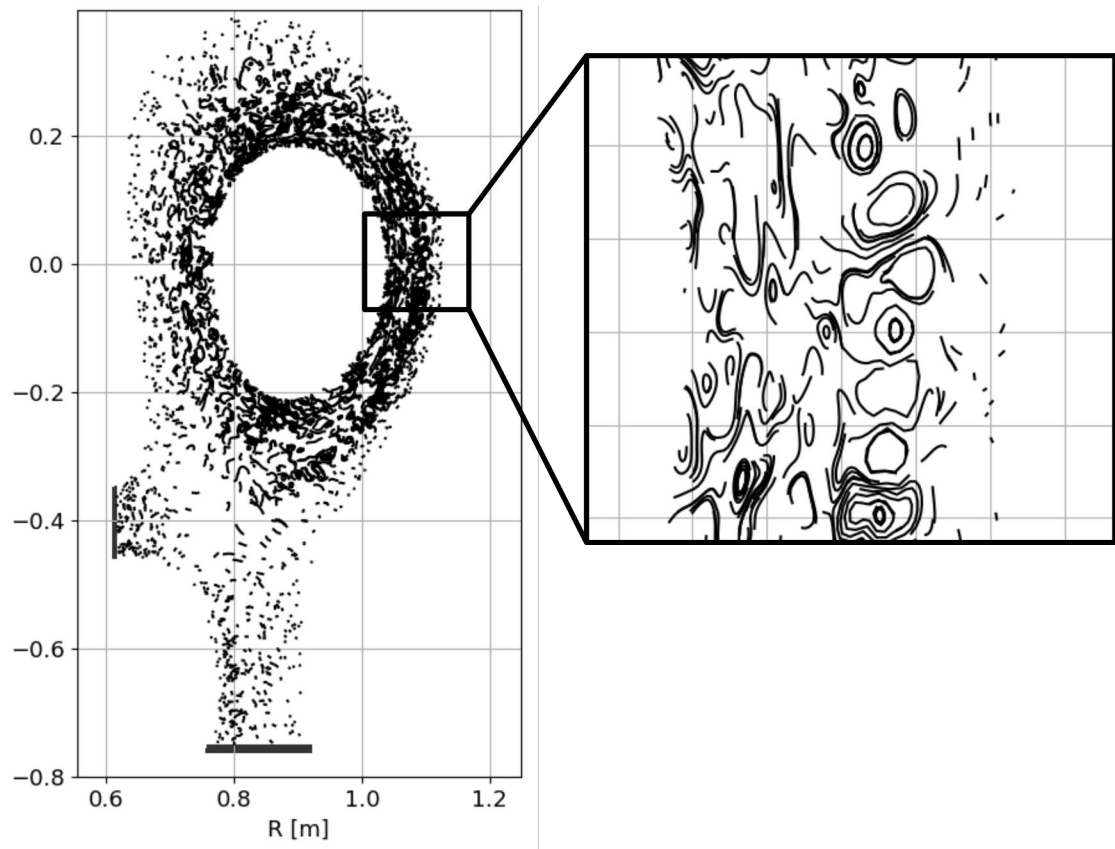


Figure 9.5.: Poincaré plot of the fluctuating magnetic field in the TCV high-power case.

What about the average taken out to avoid twice the Grad-Shafranov shift ?

10. Simulations of Magnetic ripple

Developments performed in the scope of this thesis can be useful for applications other than electromagnetic effects on plasmas. In transport mode with large perpendicular diffusion coefficients, a regime where drifts and turbulent scales are not solved, modulations of the magnetic field can have an external source. Because of the toroidal locality of toroidal field coils, the equilibrium magnetic field itself is not axisymmetric, a phenomenon usually referred to as "magnetic ripple". This chapter describes how the implementation of fluctuating magnetic fields in the framework of flutter can be used to simulate perturbations of the equilibrium magnetic field.

10.1. Motivation for simulating magnetic ripple

Power exhaust is a major concern in magnetic fusion research. Accurately predicting the heat load on the divertor plates is essential for the design and operation of current and future tokamaks. Estimates for the International Thermonuclear Experimental Reactor (ITER), the most powerful device currently under construction, indicate maximum local heat loads close to material limits[31]. For this reason it is important to study transport of heat and particle fluxes in present experiments, coupling the experimental analysis with a modelling effort with dedicated numerical tools.

Experiments conducted on the tungsten environment steady-state tokamak (WEST) at CEA in Cadarache, France[4], have demonstrated that the heat deposition on the divertor targets is not uniform in the toroidal direction. A "snake skin" pattern (see Figure 10.1), with alternating local maxima, appears on the inner and outer divertor targets. Reconstructions from infrared camera images exhibit a considerable difference between peaks and lows along a target line. These variations correlate with the disposition of the toroidal magnetic field coils, which locally modify the field lines and amplitude. This effect is known as magnetic ripple[77], and it is particularly pronounced on WEST, where the 18 coils cause strong variations in the amplitude of the magnetic field \mathbf{B} . For example, fast ions trapped in the toroidal magnetic field ripple have been found to be responsible for significant power losses[55]. Moreover, it is important to determine the impact of this toroidal modulation on impurity transport, in particular on tungstene contamination of the core[16].

SOLEDGE3X is a powerful fluid code for scrape-off-layer (SOL) and edge plasma analysis. The simulation domain extends from the far core across the separatrix up to the first wall in complex geometries. Its full model is capable of simulating resistive

10. Simulations of Magnetic ripple – 10.2. Generation of a non-axisymmetric magnetic configuration

drift-wave turbulence[6] with advanced fluid closures[9] and interactions with recycling neutrals[58]. A "transport" mode, where cross-field transport is approximated with effective diffusion coefficients, allows simulations to run until convergence on large machines like ITER[64] or JT-60SA[15]. Applications of this code include studies on impurity transport[11], heat exhaust[63], and detachment regimes in the divertor[84].

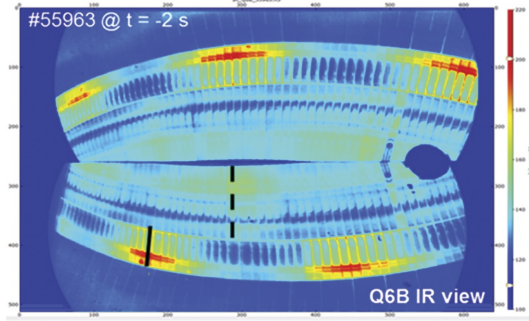


Figure 10.1.: Infrared camera view of the divertor target, taken from [4]. Red zones correspond to hot regions with high heat deposition. One can see the "snake skin" pattern, where the maximal intensity alternates between the inner and outer strike points.

In its current form, SOLEDGE3X can address 2D and 3D axisymmetric configurations as well as 3D non axisymmetric wall geometries[17], but still requires a 3D axisymmetric magnetic field. Therefore, toroidal variations of the magnetic field due to ripple could not be taken into account. Moreover, matching simulation results to experimental data is made difficult by the toroidal locality of Langmuir probes and their consequent susceptibility to ripple effects. Recent developments in the turbulence model have introduced electromagnetic effects[23], where magnetic field lines are perturbed by fluctuations of the magnetic vector potential. In this paper, we demonstrate that the new implementations can be used not only for plasma-induced perturbations but also for external perturbations of the axisymmetric magnetic field. This paves the way for ripple simulations in SOLEDGE3X and will be applied to a WEST scenario in this paper.

10.2. Generation of a non-axisymmetric magnetic configuration

The SOLEDGE3X framework is capable of addressing magnetic configurations with singularities at one or more X-points. Constructed by a combination of a toroidal field, \mathbf{B}_t , and a poloidal field, \mathbf{B}_{pol} , the expression for the magnetic field is:

$$\mathbf{B}_{axi} = \mathbf{B}_t + \mathbf{B}_{pol} = F \nabla \varphi + \nabla \Psi \times \nabla \varphi \quad (10.1)$$

10. Simulations of Magnetic ripple – 10.2. Generation of a non-axisymmetric magnetic configuration

where φ represents the toroidal angle. The toroidal field \mathbf{B}_t is derived from a toroidal flux F and \mathbf{B}_{pol} from a poloidal flux function Ψ . For high numerical accuracy, the meshing in SOLEGE3X is aligned to magnetic flux surfaces, treating singularities with a multi-domain decomposition shown in Figure 10.2

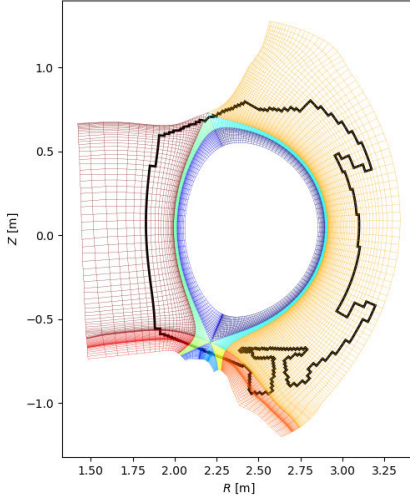


Figure 10.2.: Exemplary SOLEDGE3X mesh for a WEST single-null geometry

On top of this axisymmetric basis, we calculate the ripple perturbation of the magnetic field induced by the toroidal distribution of the toroidal field coils. For that, we simplify each coil to a single, circular wire. We first discretize each of the N_c coils into N_{seg} segments. For every cell in the SOLEDGE3X grid, we then calculate the magnetic field associated with the coils using the Biot-Savart law:

$$\mathbf{B}_{ripple} = \frac{\mu_0}{4\pi} I_c \sum_{i=1}^{N_c} \sum_{j=1}^{N_{seg}} \frac{\mathbf{d}_{i,j} \times (\mathbf{s}_{i,j+1} - \mathbf{s}_{i,j})}{\|\mathbf{d}_{i,j}\|^3} \quad (10.2)$$

where the coil current I_c corresponds to the nominal coil current times the number of wire turns in a coil, $\mathbf{s}_{i,j}$ represents the start and end locations of each coil segment, and $\mathbf{d}_{i,j}$ is the vector from each mesh point to the segment center. To avoid accounting for the axisymmetric component of the magnetic field twice, we define the perturbation field as the toroidal fluctuations of the ripple field:

$$\mathbf{B}_{pert} = \mathbf{B}_{ripple} - \langle \mathbf{B}_{ripple} \rangle_\varphi \quad (10.3)$$

Together with the axisymmetric part from Equation ??, the equilibrium magnetic field as applied to the simulation is given by:

$$\mathbf{B} = \mathbf{B}_{axi} + \mathbf{B}_{pert} \quad (10.4)$$

10. Simulations of Magnetic ripple – 10.2. Generation of a non-axisymmetric magnetic configuration

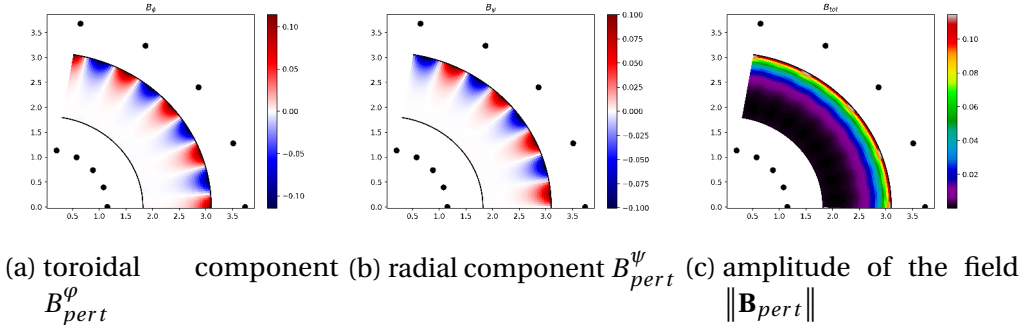


Figure 10.3.: Top views of the perturbed field \mathbf{B}_{pert} on the WEST tokamak at the mid plane. The black dots indicate the position of the toroidal field coils. The amplitude of the perturbed field remains much smaller than the axisymmetric component, whose amplitude ranges around 1T.

This strategy is now applied to compute the magnetic field ripple for the WEST tokamak, with the coil parameters described in Table 10.1. The ripple has a twofold impact on the magnetic equilibrium. A toroidal perturbation field, as shown in Figure 10.3a, modifies \mathbf{B}_t with local maxima located at the coils' positions and minima midway between two coils. The perturbation vanishes at $\pi/2$ and $3\pi/2$ of a ripple period. Conversely, the radial perturbation in Figure 10.3b vanishes at the coils and midway, and modifies the poloidal field \mathbf{B}_{pol} .

Number of coils	N_c	18
Major coil radius	R_c	2.443 m
Minor coil radius	a_c	1.292 m
Nominal coil current	I_c	1.2 kA
Number of wire turns	N_{turns}	2028

Table 10.1.: Technical parameters of the toroidal field coils used to generate the ripple field for the WEST tokamak

Even if the amplitude of the ripple field is small compared to the axisymmetric one, it strongly impacts the poloidal field \mathbf{B}_{pol} from one poloidal plane to another. As \mathbf{B}_{pol} approaches zero at X-points, the radial perturbation \mathbf{B}_{pert}^ψ induced by the coils dominates over the axisymmetric component. In Figure 10.4, we observe that the X-point based on B_{pol} shifts by about 4.1 cm towards the high-field side at the maximal radial perturbation and by 2.7 cm inwards at the minimum.

10. Simulations of Magnetic ripple – 10.2. Generation of a non-axisymmetric magnetic configuration

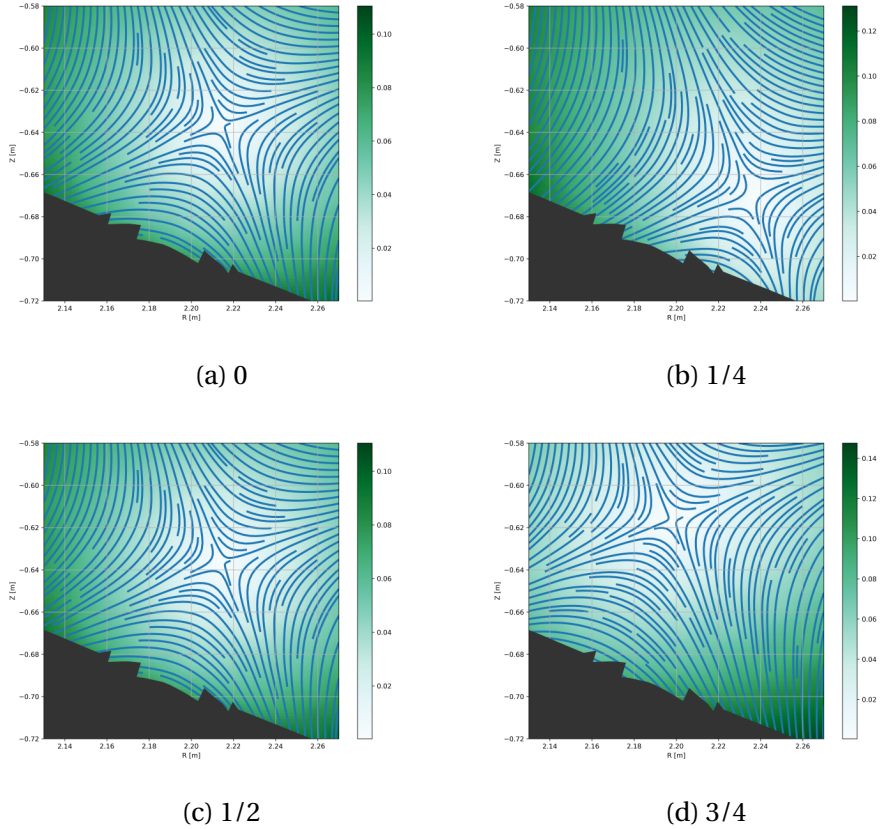


Figure 10.4.: Map of the poloidal field B_{pol} [T] at several poloidal planes within a ripple period around the lower X-point and the divertor targets. Streamlines are superposed to the fields to better visualize the position of the X-point and the separatrix at the divertor. The phase shifts 0 and 1/2 with respect to the coil positions are identical to the axisymmetric configuration as B_{pert}^ψ vanishes while the planes at 1/4 and 3/4 correspond to the respective maximum and minimum of B_{pert}^ψ

However, this does not mean that the last closed flux surface (LCFS) experiences such a strong modulation. Indeed, the toroidal field \mathbf{B}_t imposes a strong self-similarity between poloidal planes. Tracing particles in the magnetic field, we observe in Figure 10.5 that particles seeded at the same position in different poloidal planes are only modulated by a few millimeters, and key features of the configuration, such as strike points or the X-point, remain almost unaffected.

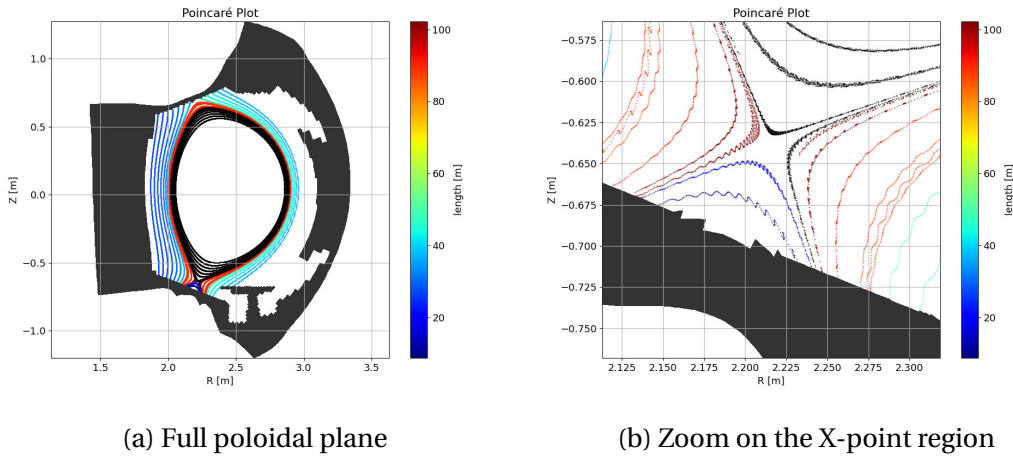


Figure 10.5.: Poincaré plot at coil-aligned poloidal planes. Seed points are uniformly distributed on the mid-plane along the radial and toroidal directions. Because of the periodicity of the perturbated field, each point corresponds to a field line crossing any of the N_c planes aligned with a coil. The total length of a field line from wall to wall translates in its color, black standing for an infinite closed field line.

10.3. Application to a WEST scenario

To demonstrate the newly implemented feature, we perform a SOLEDGE3X simulation on a WEST scenario with ripple. We consider a simple deuterium plasma with recycling fluid neutrals (recycling coefficient 98%). The core density fixed to 2×10^{19} particles/m³, and 1 MW Ohmic heating is equally applied to electrons and ions. Cross-field transport is emulated by a constant diffusion of 0.3 m²/s.

To reduce numerical costs, we only simulate one ripple period, or 1/18th of the full torus, and periodically expand the simulated plasma in the toroidal direction. The simulation contains 250,000 cells spread over 16 poloidal planes and was run on 384 processors of the MARCONI computing center[42] for 20 ms simulated plasma time. The plasma has not yet reached a converged state, but is sufficiently stable to observe ripple-induced phenomena.

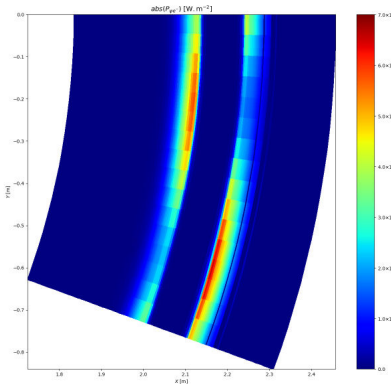


Figure 10.6.: Calculated electron wall heat flux in the divertor region from the SOLEDGE3X simulation. View on the target from the top for one ripple period.

In Figure 10.6, the heat fluxes originating at the core source reach the divertor target with maximal heat loads that alternate between the inner and the outer strike point with the toroidal coordinate. It has a strong resemblance with the "snake skin" pattern in Figure 10.1 observed on infrared imagery during the tokamak operation.

10.4. Conclusion

The incorporation of magnetic ripple perturbations into the SOLEDGE3X framework significantly enhances its capability to simulate complex magnetic configurations in tokamaks. Using the Biot-Savart law to calculate the ripple effects, this study exhibits the impact of the toroidal magnetic ripple on the magnetic equilibrium configuration in the WEST tokamak. These perturbations both affect the poloidal and the radial component of the axisymmetric magnetic equilibrium, with an important modulation of the poloidal field.

The perturbed magnetic field has been integrated into all parallel advection and gradient terms of the SOLEDGE3X transport model. The radial component of the poloidal perturbation field required major refactoring of the transport model because the mesh remains aligned to axisymmetric flux surfaces. Parallel fluxes now occur in all three directions in the curvilinear coordinates. Consequently, implicit solvers for the heat and viscosity problems are now applied to full-domain 3D systems instead of independent 2D systems on each flux surface, resulting in additional computational costs.

Simulations on a realistic WEST geometry demonstrate the new capability to perform simulations in a non-axisymmetric magnetic configuration. Key features of magnetic ripple, such as the modulation of heat loads on the divertor strike points along the toroidal coordinate, are successfully recovered.

10. Simulations of Magnetic ripple – 10.4. Conclusion

With this new implementation, it will be possible to explore new physics, such as ripple effects on tungsten core contamination or improved predictions of power exhaust in tokamaks. Additionally, this enhancement allows for better comparisons between simulation and experimental data due to the toroidal locality of several plasma diagnostics.

Conclusion

Lorem ipsum dolor sit amet, consectetuer adipiscing elit. Ut purus elit, vestibulum ut, placerat ac, adipiscing vitae, felis. Curabitur dictum gravida mauris. Nam arcu libero, nonummy eget, consectetuer id, vulputate a, magna. Donec vehicula augue eu neque. Pellentesque habitant morbi tristique senectus et netus et malesuada fames ac turpis egestas. Mauris ut leo. Cras viverra metus rhoncus sem. Nulla et lectus vestibulum urna fringilla ultrices. Phasellus eu tellus sit amet tortor gravida placerat. Integer sapien est, iaculis in, pretium quis, viverra ac, nunc. Praesent eget sem vel leo ultrices bibendum. Aenean faucibus. Morbi dolor nulla, malesuada eu, pulvinar at, mollis ac, nulla. Curabitur auctor semper nulla. Donec varius orci eget risus. Duis nibh mi, congue eu, accumsan eleifend, sagittis quis, diam. Duis eget orci sit amet orci dignissim rutrum.

Nam dui ligula, fringilla a, euismod sodales, sollicitudin vel, wisi. Morbi auctor lorem non justo. Nam lacus libero, pretium at, lobortis vitae, ultricies et, tellus. Donec aliquet, tortor sed accumsan bibendum, erat ligula aliquet magna, vitae ornare odio metus a mi. Morbi ac orci et nisl hendrerit mollis. Suspendisse ut massa. Cras nec ante. Pellentesque a nulla. Cum sociis natoque penatibus et magnis dis parturient montes, nascetur ridiculus mus. Aliquam tincidunt urna. Nulla ullamcorper vestibulum turpis. Pellentesque cursus luctus mauris.

Bibliography

- [1] Satish Balay, Shirirang Abhyankar, Mark F. Adams, et al. *PETSc Web page*. <https://petsc.org/>. 2023. URL: <https://petsc.org/> (cit. on p. 114).
- [2] Charles K Birdsall. “Particle-in-cell charged-particle simulations, plus Monte Carlo collisions with neutral atoms, PIC-MCC”. In: *IEEE Transactions on plasma science* 19.2 (1991), pp. 65–85 (cit. on p. 34).
- [3] S. I. Braginskii. “Transport processes in a plasma”. In: *Reviews of plasma physics* 1 (1965), p. 205 (cit. on p. 62).
- [4] J. Bucalossi, J. Achard, O. Agullo, et al. “Operating a full tungsten actively cooled tokamak: overview of WEST first phase of operation”. In: *Nuclear Fusion* 62.4 (Feb. 2022), p. 042007. DOI: [10.1088/1741-4326/ac2525](https://doi.org/10.1088/1741-4326/ac2525). URL: <https://dx.doi.org/10.1088/1741-4326/ac2525> (cit. on pp. 118, 119).
- [5] H Bufferand, J Bucalossi, G Ciraolo, et al. “Progress in edge plasma turbulence modelling—hierarchy of models from 2D transport application to 3D fluid simulations in realistic tokamak geometry”. In: *Nuclear Fusion* 61.11 (2021), p. 116052 (cit. on pp. 82, 84, 114).
- [6] H. Bufferand, C. Baudoin, J. Bucalossi, et al. “Implementation of drift velocities and currents in SOLEDGE2D–EIRENE”. In: *Nuclear Materials and Energy* 12 (2017). Proceedings of the 22nd International Conference on Plasma Surface Interactions 2016, 22nd PSI, pp. 852–857. ISSN: 2352-1791. DOI: [10.1016/j.nme.2016.11.031](https://doi.org/10.1016/j.nme.2016.11.031). URL: <https://www.sciencedirect.com/science/article/pii/S2352179116301946> (cit. on p. 119).
- [7] H. Bufferand, J. Bucalossi, G. Ciraolo, et al. “Progress in edge plasma turbulence modelling—hierarchy of models from 2D transport application to 3D fluid simulations in realistic tokamak geometry”. In: *Nuclear Fusion* 61.11 (2021), p. 116052 (cit. on p. 58).
- [8] H. Bufferand, G. Ciraolo, Y. Marandet, et al. “Numerical modeling for divertor design of the WEST device with a focus on plasma wall interactions”. In: *Nucl. Fus.* 55(5) (2015), p. 053025 (cit. on p. 58).
- [9] Hugo Bufferand, J Balbin, S Baschetti, et al. “Implementation of multi-component Zhdanov closure in SOLEDGE3X”. In: *Plasma Physics and Controlled Fusion* 64.5 (2022), p. 055001 (cit. on p. 119).

Bibliography

- [10] J. D. Callen. "Drift-Wave Turbulence Effects on Magnetic Structure and Plasma Transport in Tokamaks". In: *Phys. Rev. Lett.* 39 (24 Dec. 1977), pp. 1540–1543. DOI: [10.1103/PhysRevLett.39.1540](https://doi.org/10.1103/PhysRevLett.39.1540). URL: <https://link.aps.org/doi/10.1103/PhysRevLett.39.1540> (cit. on p. 49).
- [11] G Ciraolo, S Di Genova, H Yang, et al. "Interpretative modeling of impurity transport and tungsten sources in WEST boundary plasma". In: *Nuclear Fusion* 61.12 (2021), p. 126015 (cit. on pp. 58, 119).
- [12] L. Cohen. "Wave propagation with dispersion and damping". In: *Proceedings of SPIE - The International Society for Optical Engineering* 5559 (Oct. 2004). DOI: [10.1117/12.564247](https://doi.org/10.1117/12.564247) (cit. on p. 99).
- [13] James William S Cook, RO Dendy, and Sandra C Chapman. "Particle-in-cell simulations of the magnetoacoustic cyclotron instability of fusion-born alpha-particles in tokamak plasmas". In: *Plasma Physics and Controlled Fusion* 55.6 (2013), p. 065003 (cit. on p. 34).
- [14] W. D. D'haeseleer, W. N. G. Hitchon, J. D. Shohet Callen, et al. *Flux Coordinates and Magnetic Field Structure*. Springer Series in Computational Physics, 1991. ISBN: 978-3-642-75595-8 (cit. on p. 72).
- [15] Ludovica De Gianni, Guido Ciraolo, Gerardo Giruzzi, et al. "Core and edge modeling of JT-60SA H-mode highly radiative scenarios using SOLEDGE3X-EIRENE and METIS codes". In: *Frontiers in Physics* 12 (2024), p. 1422286 (cit. on p. 119).
- [16] S Di Genova, A Gallo, N Fedorczak, et al. "Modelling of tungsten contamination and screening in WEST plasma discharges". In: *Nuclear Fusion* 61.10 (2021), p. 106019 (cit. on p. 118).
- [17] Stefano Di Genova. "Heavy ions migration in tokamak boundary plasmas : development of a numerical model to interpret WEST experiments". PhD thesis. Aix-Marseille University, 2023 (cit. on p. 119).
- [18] G. Dif-Pradalier, V. Grandgirard, Y. Sarazin, et al. "Interplay between Gyrokinetic Turbulence, Flows, and Collisions: Perspectives on Transport and Poloidal Rotation". In: *Phys. Rev. Lett.* 103 (6 Aug. 2009), p. 065002. DOI: [10.1103/PhysRevLett.103.065002](https://doi.org/10.1103/PhysRevLett.103.065002). URL: <https://link.aps.org/doi/10.1103/PhysRevLett.103.065002> (cit. on p. 40).
- [19] Jitka Drkošova, Anne Greenbaum, Miroslav Rozložník, et al. "Numerical stability of GMRES". In: *BIT Numerical Mathematics* 35.3 (1995), pp. 309–330 (cit. on p. 86).
- [20] B. D. Dudson, A. Allen, G. Breyiannis, et al. "BOUT : Recent and current developments". In: *Journal of Plasma Physics* 81.1 (2015), p. 365810104. DOI: [10.1017/S0022377814000816](https://doi.org/10.1017/S0022377814000816) (cit. on p. 49).

Bibliography

- [21] B. D. Dudson, S. L. Newton, J. T. Omotani, et al. “On Ohm’s law in reduced plasma fluid models”. In: *Plasma Physics and Controlled Fusion* 63.12 (Oct. 2021). ISSN: 0741-3335. DOI: [10.1088/1361-6587/ac2af9](https://doi.org/10.1088/1361-6587/ac2af9). URL: <https://www.osti.gov/biblio/1840134> (cit. on pp. 50, 102, 103).
- [22] B.D. Dudson, M.V. Umansky, X.Q. Xu, et al. “BOUT++: A framework for parallel plasma fluid simulations”. In: *Computer Physics Communications* 180.9 (2009), pp. 1467–1480. ISSN: 0010-4655. DOI: <https://doi.org/10.1016/j.cpc.2009.03.008>. URL: <https://www.sciencedirect.com/science/article/pii/S0010465509001040> (cit. on pp. 40, 49).
- [23] Raffael Düll, Hugo Bufferand, Eric Serre, et al. “Introducing electromagnetic effects in Soledge3X”. In: *Contributions to Plasma Physics* (2024), e202300147 (cit. on p. 119).
- [24] Thomas Eich, AW Leonard, RA Pitts, et al. “Scaling of the tokamak near the scrape-off layer H-mode power width and implications for ITER”. In: *Nuclear fusion* 53.9 (2013), p. 093031 (cit. on p. 32).
- [25] Richard Fitzpatrick. “A simple model of the resistive wall mode in tokamaks”. In: *Physics of Plasmas* 9.8 (2002), pp. 3459–3469 (cit. on p. 22).
- [26] HP Furth, PH Rutherford, and H Selberg. “Tearing mode in the cylindrical tokamak”. In: *The Physics of Fluids* 16.7 (1973), pp. 1054–1063 (cit. on p. 22).
- [27] Jean Gallier et al. “The Schur complement and symmetric positive semidefinite (and definite) matrices”. In: *Penn Engineering* (2010), pp. 1–12 (cit. on p. 88).
- [28] M. Giacomin, P. Ricci, A. Corrado, et al. “The GBS code for the self-consistent simulation of plasma turbulence and kinetic neutral dynamics in the tokamak boundary”. In: *Journal of Computational Physics* 463 (2022), p. 111294. ISSN: 0021-9991. DOI: [10.1016/j.jcp.2022.111294](https://doi.org/10.1016/j.jcp.2022.111294). URL: <https://www.sciencedirect.com/science/article/pii/S0021999122003564> (cit. on pp. 40, 49, 67).
- [29] H. Grad and H. Rubin. *Hydromagnetic Equilibria and Force-Free Fields*. INIS-XU-021. United Nations (UN), 1958, pp. 190–197. URL: http://inis.iaea.org/search/search.aspx?orig_q=RN:39082408 (cit. on p. 23).
- [30] Anne Greenbaum, Miroslav Rozložník, and Zdenek Strakoš. “Numerical behaviour of the modified Gram-Schmidt GMRES implementation”. In: *BIT Numerical Mathematics* 37.3 (1997), pp. 706–719 (cit. on p. 86).
- [31] James P Gunn, S Carpentier-Chouchana, F Escourbiac, et al. “Surface heat loads on the ITER divertor vertical targets”. In: *Nuclear Fusion* 57.4 (2017), p. 046025 (cit. on pp. 32, 118).
- [32] S. Günter, Q. Yu, J. Krüger, et al. “Modelling of heat transport in magnetised plasmas using non-aligned coordinates”. In: *Journal of Computational Physics* 209.1 (2005), pp. 354–370. ISSN: 0021-9991. DOI: <https://doi.org/10.1016/j.jcp.2005.03.021>. URL: <https://www.sciencedirect.com/science/article/pii/S0021999105001373> (cit. on pp. 77, 82, 86).

Bibliography

- [33] Robert Hager, S. Ku, A. Y. Sharma, et al. “Electromagnetic total-f algorithm for gyrokinetic particle-in-cell simulations of boundary plasma in XGC”. In: *Phys. Plasmas* 29.11 (2022), p. 112308. DOI: [10.1063/5.0097855](https://doi.org/10.1063/5.0097855). URL: <https://doi.org/10.1063/5.0097855> (cit. on p. 68).
- [34] Akira Hasegawa and Masahiro Wakatani. “Plasma edge turbulence”. In: *Physical Review Letters* 50.9 (1983), p. 682 (cit. on p. 46).
- [35] Koji Hasegawa and Takao Shimada. “Staggered Grid with Collocated Grid Points of Velocities for Modeling Propagation of Elastic Waves in Anisotropic Solids by Finite-Difference Time Domain Method”. In: *Japanese Journal of Applied Physics* 51.7S (2012), 07GB04 (cit. on p. 77).
- [36] RJ Hastie, Jesus J Ramos, and Francesco Porcelli. “Drift ballooning instabilities in tokamak edge plasmas”. In: *Physics of Plasmas* 10.11 (2003), pp. 4405–4412 (cit. on p. 48).
- [37] RD Hazeltine, M Kotschenreuther, and PJ Morrison. “A four-field model for tokamak plasma dynamics”. In: *Physics of Fluids* 28.8 (1985), p. 2466 (cit. on p. 45).
- [38] Per Helander and Dieter J Sigmar. *Collisional transport in magnetized plasmas*. Vol. 4. Cambridge university press, 2005 (cit. on p. 62).
- [39] P Hennequin, R Sabot, C Honoré, et al. “Scaling laws of density fluctuations at high-k on Tore Supra”. In: *Plasma Physics and Controlled Fusion* 46.12B (Nov. 2004), B121. DOI: [10.1088/0741-3335/46/12B/011](https://doi.org/10.1088/0741-3335/46/12B/011). URL: <https://doi.org/10.1088/0741-3335/46/12B/011> (cit. on p. 40).
- [40] N. Horsten, G. Samaey, and M. Baelmans. “Development and assessment of 2D fluid neutral models that include atomic databases and a microscopic reflection model”. In: *Nuclear Fusion* 57.11 (Aug. 2017), p. 116043. DOI: [10.1088/1741-4326/aa8009](https://doi.org/10.1088/1741-4326/aa8009). URL: <https://doi.org/10.1088/1741-4326/aa8009> (cit. on p. 111).
- [41] IH Hutchinson, J Freidberg, et al. “Introduction to plasma physics”. In: *Electronic book available from: http://silas.psfc.mit.edu/introplasma/index.html* (2001) (cit. on p. 28).
- [42] F Iannone, G. Bracco, C. Cavazzoni, et al. “MARCONI-FUSION: The new high-performance computing facility for European nuclear fusion modelling”. In: *Fusion Engineering and Design* 129 (2018), pp. 354–358. ISSN: 0920-3796. DOI: [10.1016/j.fusengdes.2017.11.004](https://doi.org/10.1016/j.fusengdes.2017.11.004). URL: <https://www.sciencedirect.com/science/article/pii/S0920379617309018> (cit. on pp. 114, 123).
- [43] I. Keramidas Charidakos, J. R. Myra, S. Parker, et al. “Analysis of equilibrium and turbulent fluxes across the separatrix in a gyrokinetic simulation”. In: *Physics of Plasmas* 25.7 (July 2018), p. 072306. ISSN: 1070-664X. DOI: [10.1063/1.5037723](https://doi.org/10.1063/1.5037723). eprint: <https://pubs.aip.org/aip/pop/article-pdf/doi/10.1063/1.5037723/14763677/072306_1\online.pdf>. URL: <https://doi.org/10.1063/1.5037723> (cit. on p. 40).

Bibliography

- [44] Rinat Khaziev and Davide Curreli. “hPIC: A scalable electrostatic particle-in-cell for plasma–material interactions”. In: *Computer Physics Communications* 229 (2018), pp. 87–98 (cit. on p. 34).
- [45] M Kruskal and JL Tuck. “The instability of a pinched fluid with a longitudinal magnetic field”. In: *Proceedings of the Royal Society of London. Series A. Mathematical and Physical Sciences* 245.1241 (1958), pp. 222–237 (cit. on p. 22).
- [46] J D Lawson. “Some Criteria for a Power Producing Thermonuclear Reactor”. In: *Proceedings of the Physical Society. Section B* 70.1 (Jan. 1957), p. 6. DOI: [10.1088/0370-1301/70/1/303](https://doi.org/10.1088/0370-1301/70/1/303). URL: <https://dx.doi.org/10.1088/0370-1301/70/1/303> (cit. on p. 16).
- [47] Jarrod Leddy, Ben Dudson, Michele Romanelli, et al. “On the validity of drift-reduced fluid models for tokamak plasma simulation”. In: *Plasma Physics and Controlled Fusion* 57.12 (2015), p. 125016 (cit. on p. 48).
- [48] Wonjae Lee, J.R. Angus, Maxim V. Umansky, et al. “Electromagnetic effects on plasma blob-filament transport”. In: *Journal of Nuclear Materials* 463 (2015), pp. 765–768. ISSN: 0022-3115. DOI: [10.1016/j.jnucmat.2014.09.083](https://doi.org/10.1016/j.jnucmat.2014.09.083). URL: <https://www.sciencedirect.com/science/article/pii/S0022311514006837> (cit. on pp. 48, 106).
- [49] Wonjae Lee, Maxim V Umansky, JR Angus, et al. “Electromagnetic effects on dynamics of high-beta filamentary structures”. In: *Physics of Plasmas* 22.1 (2015) (cit. on p. 106).
- [50] A Lessig, C Caldin Queiros, E Franck, et al. “Fluid models for Tokamak Plasmas: Magneto-Hydrodynamic”. In: (2016) (cit. on p. 37).
- [51] A. Loarte, B. Lipschultz, A.S. Kukushkin, et al. “Chapter 4: Power and particle control”. In: *Nuclear Fusion* 47.6 (June 2007), S203. DOI: [10.1088/0029-5515/47/6/S04](https://doi.org/10.1088/0029-5515/47/6/S04). URL: <https://dx.doi.org/10.1088/0029-5515/47/6/S04> (cit. on p. 40).
- [52] HF Meier, JJN Alves, and M Mori. “Comparison between staggered and collocated grids in the finite-volume method performance for single and multi-phase flows”. In: *Computers & chemical engineering* 23.3 (1999), pp. 247–262 (cit. on p. 74).
- [53] AB Mikhailovskii and LI Rudakov. “The stability of a spatially inhomogeneous plasma in a magnetic field”. In: *Soviet Physics JETP* 44 (1963), pp. 912–918 (cit. on p. 50).
- [54] AB Mikhailovskii and VS Tsypin. “Transport equations and gradient instabilities in a high pressure collisional plasma”. In: *Plasma Physics* 13.9 (1971), p. 785 (cit. on p. 45).
- [55] D Moiraf, J Morales, L Colas, et al. “Optimization of the operational domain for ICRH scenarios in WEST from statistical analysis”. In: *Nuclear Fusion* 63.8 (2023), p. 086010 (cit. on p. 118).

Bibliography

- [56] D.S. Oliveira, T. Body, D. Galassi, et al. “Validation of edge turbulence codes against the TCV-X21 diverted L-mode reference case”. In: *Nuclear Fusion* 62.9 (July 2022), p. 096001. DOI: [10.1088/1741-4326/ac4cde](https://doi.org/10.1088/1741-4326/ac4cde). URL: <https://dx.doi.org/10.1088/1741-4326/ac4cde> (cit. on p. 111).
- [57] Anna Pyzara, Beata Bylina, and Jarosław Bylina. “The influence of a matrix condition number on iterative methods’ convergence”. In: *2011 Federated Conference on Computer Science and Information Systems (FedCSIS)*. IEEE. 2011, pp. 459–464 (cit. on p. 86).
- [58] V. Quadri, P. Tamain, Y. Marandet, et al. “Self-organization of plasma edge turbulence in interaction with recycling neutrals”. In: *Contributions to Plasma Physics* n/a.n/a (), e202300146. DOI: <https://doi.org/10.1002/ctpp.202300146>. eprint: <https://onlinelibrary.wiley.com/doi/pdf/10.1002/ctpp.202300146>. URL: <https://onlinelibrary.wiley.com/doi/abs/10.1002/ctpp.202300146> (cit. on pp. 111, 119).
- [59] Tariq Rafiq, Chris C Hegna, James D Callen, et al. “Unified theory of resistive and inertial ballooning modes in three-dimensional configurations”. In: *Physics of Plasmas* 16.10 (2009) (cit. on p. 50).
- [60] P Ricci, F D Halpern, S Jolliet, et al. “Simulation of plasma turbulence in scrape-off layer conditions: the GBS code, simulation results and code validation”. In: *Plasma Physics and Controlled Fusion* 54.12 (Nov. 2012), p. 124047. DOI: [10.1088/0741-3335/54/12/124047](https://doi.org/10.1088/0741-3335/54/12/124047). URL: <https://dx.doi.org/10.1088/0741-3335/54/12/124047> (cit. on p. 49).
- [61] K-U Riemann. “The Bohm criterion and sheath formation”. In: *Journal of Physics D: Applied Physics* 24.4 (1991), p. 493 (cit. on p. 31).
- [62] N Rivals, P Tamain, Y Marandet, et al. “SOLEDGE3X full vessel plasma simulations for computation of ITER first-wall fluxes”. In: *Contributions to Plasma Physics* 262.5–6 (2022), e202100182 (cit. on p. 58).
- [63] Nicolas Rivals, Patrick Tamain, Yannick Marandet, et al. “Impact of enhanced far-SOL transport on first wall fluxes in ITER from full vessel edge-plasma simulations”. In: *Nuclear Materials and Energy* 33 (2022), p. 101293 (cit. on p. 119).
- [64] Nicolas Rivals, Patrick Tamain, Yannick Marandet, et al. “SOLEDGE3X full vessel plasma simulations for computation of ITER first-wall fluxes”. In: *Contributions to Plasma Physics* 62.5-6 (2022), e202100182 (cit. on p. 119).
- [65] P.J. Roache. “Code Verification by the Method of Manufactured Solutions ”. In: *Journal of Fluids Engineering* 124.1 (Nov. 2001), pp. 4–10. ISSN: 0098-2202. DOI: [10.1115/1.1436090](https://doi.org/10.1115/1.1436090). URL: <https://doi.org/10.1115/1.1436090> (cit. on p. 91).
- [66] Felix Rubio, Mauricio Hanzich, Albert Farrés, et al. “Finite-difference staggered grids in GPUs for anisotropic elastic wave propagation simulation”. In: *Computers & geosciences* 70 (2014), pp. 181–189 (cit. on p. 77).

Bibliography

- [67] DD Ryutov, RH Cohen, TD Rognlien, et al. “The magnetic field structure of a snowflake divertor”. In: *Physics of Plasmas* 15.9 (2008) (cit. on p. 26).
- [68] Frédéric Schwander, Eric Serre, Hugo Bufferand, et al. “Global fluid simulations of edge plasma turbulence in tokamaks: a review”. In: *Computers & Fluids* 270 (2024), p. 106141. ISSN: 0045-7930. DOI: <https://doi.org/10.1016/j.compfluid.2023.106141>. URL: <https://www.sciencedirect.com/science/article/pii/S0045793023003663> (cit. on pp. 40, 67).
- [69] Bruce D. Scott. “Three-dimensional computation of drift Alfvén turbulence”. In: *Plasma Phys. Control. Fusion* 39 (1997), p. 1635 (cit. on pp. 49, 50).
- [70] VD Shafranov. “Stability of plasmas confined by magnetic fields”. In: *Soviet Journal of Atomic Energy* 5 (1956), p. 38 (cit. on p. 22).
- [71] VD Shafranov. “On equilibrium magnetohydrodynamic configurations”. In: *Zh. Eksp. Teor. Fiz.* 33.3 (1957), pp. 710–722 (cit. on p. 23).
- [72] A.N. Simakov and PJ. Catto. “Drift-ordered fluid equations for field-aligned modes in low- beta collisional plasma with equilibrium pressure pedestals”. In: *Phys. of Plasma* 10.1 (2003), pp. 4744–57 (cit. on pp. 42, 45).
- [73] P. C. Stangeby. *The Plasma Boundary of Magnetic Fusion Devices (1st ed.)* Boca Raton: CRC Press, 2000 (cit. on pp. 31, 70).
- [74] A. Stegmeir, A. Ross, T. Body, et al. “Global turbulence simulations of the tokamak edge region with GRILLIX”. In: *Phys. Plasmas* 26.5 (2019), p. 052517. DOI: [10.1063/1.5089864](https://doi.org/10.1063/1.5089864). URL: <https://doi.org/10.1063/1.5089864> (cit. on pp. 40, 49, 102).
- [75] A. A. Stepanenko. “Impact of electromagnetic effects on macroscopic dynamics of blobs in hot low- β edge plasma of fusion devices”. In: *Physics of Plasmas* 27.9 (Sept. 2020), p. 092301. DOI: [10.1063/5.0013435](https://doi.org/10.1063/5.0013435). URL: <https://doi.org/10.1063/5.0013435> (cit. on pp. 48, 106).
- [76] P. Tamain, H. Bufferand, G. Ciraolo, et al. “The TOKAM3X code for edge turbulence fluid simulations of tokamak plasmas in versatile magnetic geometries”. In: *Journal of Computational Physics* 321 (2016), pp. 606–623. ISSN: 0021-9991. DOI: [10.1016/j.jcp.2016.05.038](https://doi.org/10.1016/j.jcp.2016.05.038). URL: <https://www.sciencedirect.com/science/article/pii/S0021999116301838> (cit. on pp. 58, 71, 82, 114).
- [77] Keiji Tani, Masafumi Azumi, Hiroshi Kishimoto, et al. “Effect of toroidal field ripple on fast ion behavior in a tokamak”. In: *Journal of the Physical Society of Japan* 50.5 (1981), pp. 1726–1737 (cit. on p. 118).
- [78] Asdex Team et al. “The H-mode of ASDEX”. In: *Nuclear Fusion* 29.11 (1989), p. 1959 (cit. on p. 32).
- [79] David Tskhakaya, Konstantin Matyash, Ralf Schneider, et al. “The Particle-In-Cell Method”. In: *Contributions to Plasma Physics* 47.8-9 (2007), pp. 563–594 (cit. on p. 33).

Bibliography

- [80] Abraham Van der Sluis. “Condition numbers and equilibration of matrices”. In: *Numerische Mathematik* 14.1 (1969), pp. 14–23 (cit. on p. 85).
- [81] H. A. van der Vorst. “Bi-CGSTAB: A Fast and Smoothly Converging Variant of Bi-CG for the Solution of Nonsymmetric Linear Systems”. In: *SIAM J. Sci. Stat. Comput.* 13.2 (1992), pp. 631–644. DOI: [10.1137/0913035](https://doi.org/10.1137/0913035) (cit. on p. 114).
- [82] Dong Wang and Steven J Ruuth. “Variable step-size implicit-explicit linear multistep methods for time-dependent partial differential equations”. In: *Journal of Computational Mathematics* (2008), pp. 838–855 (cit. on p. 81).
- [83] JA Wesson. “Hydromagnetic stability of tokamaks”. In: *Nuclear Fusion* 18.1 (1978), p. 87 (cit. on p. 71).
- [84] Hao Yang. “Control of detachment in the divertor region of tokamaks: impact of wall geometry, particle, and energy sources”. PhD thesis. Aix-Marseille University, 2023 (cit. on p. 119).
- [85] Kane Yee. “Numerical solution of initial boundary value problems involving Maxwell’s equations in isotropic media”. In: *IEEE Transactions on antennas and propagation* 14.3 (1966), pp. 302–307 (cit. on p. 77).
- [86] A Zeiler, JF Drake, and B Rogers. “Nonlinear reduced Braginskii equations with ion thermal dynamics in toroidal plasma”. In: *Physics of Plasmas* 4.6 (1997), pp. 2134–2138 (cit. on p. 62).
- [87] Kaiyu Zhang, Wladimir Zhlobenko, Andreas Stegmeir, et al. “Magnetic flutter effect on validated edge turbulence simulations”. In: *Nuclear Fusion* 64.3 (2024), p. 036016 (cit. on pp. 49, 68).
- [88] Wladimir Zhlobenko, Kaiyu Zhang, Andreas Stegmeir, et al. “Tokamak edge-SOL turbulence in H-mode conditions simulated with a global, electromagnetic, transcollisional drift-fluid model”. In: *Nuclear Fusion* (2024). URL: <http://iopscience.iop.org/article/10.1088/1741-4326/ad7611> (cit. on p. 48).
- [89] Ben Zhu, Xue-Qiao Xu, and Xian-Zhu Tang. “Electromagnetic turbulence simulation of tokamak edge plasma dynamics and divertor heat load during thermal quench”. In: *Nuclear Fusion* 63.8 (July 11, 2023). Not subject to copyright in the USA. Contribution of U.S. Department of Energy, p. 086027. DOI: [10.1088/1741-4326/acdfc4](https://doi.org/10.1088/1741-4326/acdfc4) (cit. on p. 48).

Index

 Lorem ipsum, [4](#), [5](#)

 Nam dui ligula, [6](#)

APPENDICES

A. New software modules

In the course of the PhD, several software modules were created outside of SOLEDGE3X.

A.1. Grad-Shafranov solver

Python script

A.2. Poincaré plots

Python script

A.3. Generation of a modulated magnetic configuration

Python script cite ERGOS here.

A.4. Toroidal plots in pySOLEDGE3X

Python script

B. Curvilinear metric operators

B.1. Linear algebra

The metric coefficients together with the co-/contravariant vectors are useful tools to perform several operations on the curvilinear grid. First of all, the squared Jacobian of the transformation from the cartesian to the curvilinear coordinate systems is equal to the determinant of g_{ij} .

$$J = \frac{\partial(x, y, z)}{\partial(u^\psi, u^\theta, u^\varphi)} = \sqrt{\det[g_{ij}]} \quad (\text{B.1})$$

The dot product between two vectors \vec{v} and \vec{w} is calculated with the co-/contravariant vectors.

$$\vec{v} \cdot \vec{w} = g_{ij} v^i w^j = g^{ij} v_i w_j \quad (\text{B.2})$$

The co-/contravariant components of the cross product can also be calculated:

$$\begin{cases} (\vec{v} \times \vec{w})_k = J \epsilon_{ijk} v^i w^j \\ (\vec{v} \times \vec{w})^k = \frac{1}{J} \epsilon_{ijk} v_i w_j \end{cases} \quad (\text{B.3})$$

This operations involves the Levi-Civita symbol ϵ_{ijk} which takes the value +1 for all even permutations $\{\psi, \theta, \varphi\}, \{\theta, \varphi, \psi\}$ and $\{\varphi, \psi, \theta\}$, the value -1 for all odd permutations $\{\varphi, \theta, \psi\}, \{\theta, \psi, \varphi\}$ and $\{\psi, \varphi, \theta\}$, and is 0 for all other cases.

In various formulae such as ..., ... or ... of the SOLEDGE3X model, we need to split a vector into its parallel and perpendicular component with respect to the magnetic field \vec{B} .

$$\vec{v}_\parallel = \vec{v} \cdot \vec{b} \quad \vec{v}_\perp = -\vec{b} \times (\vec{b} \times \vec{v}) \quad (\text{B.4})$$

The vector \vec{b} contains the normalized magnetic field and hence represents a unit vector in parallel direction at each point. In the code only its co- and contravariants are calculated and stored for the entire mesh:

$$b_\psi = \vec{b} \cdot \vec{e}_\psi \quad b_\theta = \vec{b} \cdot \vec{e}_\theta \quad b_\varphi = \vec{b} \cdot \vec{e}_\varphi \quad (\text{B.5})$$

$$b^\psi = \vec{b} \cdot \vec{e}^\psi \quad b^\theta = \vec{b} \cdot \vec{e}^\theta \quad b^\varphi = \vec{b} \cdot \vec{e}^\varphi \quad (\text{B.6})$$

B.2. Centered operators

B.2.1. Differentiation

The gradient of a scalar field $S(u^\psi, u^\theta, u^\varphi)$ is calculated in terms of the reciprocal basis:

$$(\nabla S)_i = \frac{\partial S}{\partial u^i} \vec{e}^i \quad (\text{B.7})$$

In the transport equations, we need to calculate gradients in parallel direction of the field which allows us to express $\vec{\nabla}_\parallel$ in terms of the contravariant vector of the unit magnetic field from [Equation B.6](#).

$$\nabla_\parallel S = \frac{\partial S}{\partial u^i} \vec{b} \cdot \vec{e}^i = \frac{\partial S}{\partial u^\theta} b^\theta + \frac{\partial S}{\partial u^\varphi} b^\varphi \quad (\text{B.8})$$

The terms in ψ are omitted in the above formula since the equilibrium magnetic flux surfaces are located on the θ - φ coordinate surface and the vector \vec{b} has therefore a zero value in its radial component. Note that this gradient is a scalar as it always points in \vec{b} direction.

Similarly, a perpendicular gradient can be defined as:

$$\vec{\nabla}_\perp S = \vec{\nabla} S - (\nabla_\parallel S) \vec{b}$$

In terms of metric coefficients, it translates to:

$$\begin{aligned} (\vec{\nabla}_\perp S)^i &= g^{ij} (\nabla S)_j - (\nabla_\parallel S) b^i \\ &= g^{ij} \frac{\partial S}{\partial u^j} - \left(\frac{\partial S}{\partial u^\theta} b^\theta + \frac{\partial S}{\partial u^\varphi} b^\varphi \right) b^i \end{aligned} \quad (\text{B.9})$$

We have to keep in mind that the above expression leads to the contravariant components of the perpendicular gradient whereas the general expression for the gradient in [Equation B.7](#) gives its covariant components.

Next, the divergence of a vector \vec{v} is calculated by:

$$\vec{\nabla} \cdot \vec{v} = \frac{1}{J} \frac{\partial (JA^i)}{\partial u^i} \quad (\text{B.10})$$

and further the divergence of parallel vector fields $S_\parallel \vec{b}$ comes in handy:

$$\vec{\nabla} \cdot (S_\parallel \vec{b}) = \frac{1}{J} \left[\frac{\partial (JS_\parallel b^\theta)}{\partial u^\theta} + \frac{\partial (JS_\parallel b^\varphi)}{\partial u^\varphi} \right] \quad (\text{B.11})$$

The gradient and divergence operators can be combined to define a diffusion operator. The parallel Laplacian with some diffusion coefficients D reads in metric

terms:

$$\vec{\nabla} \cdot [D(\nabla_{\parallel} S) \vec{b}] = \frac{1}{J} \left[\frac{\partial \left(JD \left(\frac{\partial S}{\partial u^{\theta}} b^{\theta} + \frac{\partial S}{\partial u^{\varphi}} b^{\varphi} \right) b^{\theta} \right)}{\partial u^{\theta}} + \frac{\partial \left(JD \left(\frac{\partial S}{\partial u^{\theta}} b^{\theta} + \frac{\partial S}{\partial u^{\varphi}} b^{\varphi} \right) b^{\varphi} \right)}{\partial u^{\varphi}} \right] \quad (\text{B.12})$$

Similarly, a perpendicular diffusion operator can be defined:

$$\begin{aligned} \vec{\nabla} \cdot [D \vec{\nabla}_{\perp} S] &= \vec{\nabla} \cdot \left[D \left(\vec{\nabla} S - (\nabla_{\parallel} S) \vec{b} \right) \right] \\ &= \frac{1}{J} \frac{\partial}{\partial u^i} \left[JD \left(g^{ij} \frac{\partial S}{\partial u^j} - \left(\frac{\partial S}{\partial u^{\theta}} b^{\theta} + \frac{\partial S}{\partial u^{\varphi}} b^{\varphi} \right) b^i \right) \right] \\ &= \frac{1}{J} \left(\frac{\partial}{\partial u^{\psi}} \left[JD \left(g^{\psi\psi} \frac{\partial S}{\partial u^{\psi}} + g^{\psi\varphi} \frac{\partial S}{\partial u^{\theta}} + g^{\psi\theta} \frac{\partial S}{\partial u^{\varphi}} \right) \right] \right. \\ &\quad + \frac{\partial}{\partial u^{\theta}} \left[JD \left(g^{\theta\psi} \frac{\partial S}{\partial u^{\psi}} + \left(g^{\theta\theta} - b^{\theta} b^{\theta} \right) \frac{\partial S}{\partial u^{\theta}} + \left(g^{\theta\varphi} - b^{\varphi} b^{\theta} \right) \frac{\partial S}{\partial u^{\varphi}} \right) \right] \\ &\quad \left. + \frac{\partial}{\partial u^{\varphi}} \left[JD \left(g^{\varphi\psi} \frac{\partial S}{\partial u^{\psi}} + \left(g^{\varphi\varphi} - b^{\theta} b^{\varphi} \right) \frac{\partial S}{\partial u^{\theta}} + \left(g^{\varphi\theta} - b^{\varphi} b^{\varphi} \right) \frac{\partial S}{\partial u^{\varphi}} \right) \right] \right) \end{aligned} \quad (\text{B.13})$$

B.2.2. Scheme for centered 2D parallel diffusion

B.2.3. Scheme for 3D parallel diffusion

B.3. Staggered operators

B.3.1. Parallel gradient

In the electromagnetic vorticity equation, a discrete operator is needed to represent the gradient of $A_{\parallel} \mathbf{b}$ on the staggered grid.

$$[\nabla_{\parallel} X^{col}]_{[i_{\psi}, i_{\theta}, i_{\varphi}]}^{stg}$$

According to [Equation B.8](#), its numerical evaluation is quite straight-forward:

$$\begin{aligned} [\nabla_{\parallel} X^{col}]_{[i_{\psi}, i_{\theta}, i_{\varphi}]}^{stg} &= \frac{1}{2} \left(X_{[i_{\psi}, i_{\theta}, i_{\varphi}]} - X_{[i_{\psi}, i_{\theta}-1, i_{\varphi}]} \right) b^{\theta}_{[i_{\psi}, i_{\theta}-\frac{1}{2}, i_{\varphi}-\frac{1}{2}]} \\ &\quad + \frac{1}{2} \left(X_{[i_{\psi}, i_{\theta}, i_{\varphi}]} - X_{[i_{\psi}, i_{\theta}, i_{\varphi}-1]} \right) b^{\varphi}_{[i_{\psi}, i_{\theta}-\frac{1}{2}, i_{\varphi}-\frac{1}{2}]} \end{aligned} \quad (\text{B.14})$$

If any of the used X happens to lie inside the boundary, it is eliminated from the stencil.

The staggered divergence and parallel gradient stencils already existed in a hidden form in the original SOLEDGE3X implementation as part of the parallel Laplacian

operator on collocated fields, which first computes the parallel gradient leading to intermediate staggered results and then applies the divergence operator on these staggered intermediate results.

B.3.2. Perpendicular Laplacian

The perpendicular Laplacian can be succinctly written in term of the fluxes in and out of a staggered cell:

$$[\Delta_{\perp} X^{stg}]_{[i_{\psi}, i_{\theta}, i_{\varphi}]}^{stg} = \frac{1}{J_{[i_{\psi}, i_{\theta} - \frac{1}{2}, i_{\varphi} - \frac{1}{2}]}} \left(F_{[i_{\psi} + \frac{1}{2}, i_{\theta} - \frac{1}{2}, i_{\varphi} - \frac{1}{2}]}^{Y, \psi} - F_{[i_{\psi} - \frac{1}{2}, i_{\theta} - \frac{1}{2}, i_{\varphi} - \frac{1}{2}]}^{Y, \psi} \right. \\ \left. + F_{[i_{\psi}, i_{\theta}, i_{\varphi} - \frac{1}{2}]}^{Y, \theta} - F_{[i_{\psi}, i_{\theta} - 1, i_{\varphi} - \frac{1}{2}]}^{Y, \theta} + F_{[i_{\psi}, i_{\theta} - \frac{1}{2}, i_{\varphi}]}^{Y, \varphi} - F_{[i_{\psi}, i_{\theta} - \frac{1}{2}, i_{\varphi} - 1]}^{Y, \varphi} \right) \quad (\text{B.15})$$

If any of the staggered cell faces touches the domain boundary in any form, the corresponding flux is excluded from the divergence operator. It only remains to calculate the fluxes $F^{Y,i}$. The metric and diffusion coefficients at all faces have already been described and are represented by the term $\xi^{ij} = JD(g^{ij} - b^i b^j)$. We then can express the fluxes as:

$$F^{Y,i} = \xi^{ij} \frac{\partial X}{\partial u^j}$$

The remaining gradient must use X^{stg} at staggered points in the domain. If $[ijk]$ stands for any permutation of the staggered indices $[i_{\psi}, i_{\theta} - \frac{1}{2}, i_{\varphi} - \frac{1}{2}]$ we always have a flux of the kind:

$$F_{i - \frac{1}{2}, jk}^{Y, i} = \xi^{ii} \left(X_{ijk}^{stg} - X_{i-1,jk}^{stg} \right) \\ + \frac{1}{4} \xi^{ij} \left(X_{i,j+1,k}^{stg} - X_{i,j-1,k}^{stg} + X_{i-1,j+1,k}^{stg} - X_{i-1,j-1,k}^{stg} \right) \\ + \frac{1}{4} \xi^{ik} \left(X_{i,j,k+1}^{stg} - X_{i,j,k-1}^{stg} + X_{i-1,j,k+1}^{stg} - X_{i-1,j,k-1}^{stg} \right)$$

If any of the field points X lie in or on the domain boundary, it is not considered in the stencil and the factor $\frac{1}{4}$ is changed to $\frac{1}{3}$.